Experimental and Numerical Investigation of Developing Turbulent Flow over a Wavy Wall

by

Vinicius Martins Segunda

A Thesis submitted to the Faculty of Graduate Studies of
The University of Manitoba
in partial fulfilment of the requirements for the degree of

Master of Science

Department of Mechanical Engineering
University of Manitoba
Winnipeg, Manitoba, Canada

Abstract

Turbulent flow over a wavy wall in a horizontal channel is investigated by experimental and numerical methods. The thorough problem understanding can advance turbulent flow physics knowledge for separating and reattaching flows. Another important consideration is the performance evaluation of mathematical models used in computational fluid dynamics (CFD) codes to predict the flow characteristics. This study explores numerical models because they are critically important to the design and performance evaluation of engineering systems. The experimental data are obtained to provide repository data and more insights into the flow physics considering both the flow development and fully periodic regions.

A channel with a wavy bottom wall is considered for this study, and its main characteristic is a value of 10 for the ratio between the wave length and wave amplitude. A high-resolution particle image velocimetry (PIV) system is used to obtain detailed measurements of velocity at Reynolds number of 5040, 8400, 10700 and 13040 in both the developing and fully periodic regions. The numerical simulations are performed with a commercial CFD code using four eddy viscosity turbulence models (standard k–ϵ; Realizable k–ϵ; k–ω; and SST) and three Second-Moment Closure (SMC) turbulence models (LRR-IP, LPS and SMC-ω). This work assessed the predictive accuracy of a total of seven turbulence models.

The experimental study covered a lack of data for the flow development within the waves, prior the periodic condition region, and it supported the turbulence models evaluation. The experiments provided features of the flow such as the recirculation regions, Reynolds stresses, and turbulent kinetic energy production at different channel locations. A comprehensive comparison between models and experimental data revealed a significant dependency on the turbulence model formulation and on the wall treatment selection for the flow development and fully periodic regions predictions.

Acknowledgements

I would like to express my sincere gratitude to my academic advisors Dr. Mark F. Tachie and Dr. Scott J. Ormiston for their guidance, discussions, and constructive feedback throughout this research. Their mentorship was essential for the developing and accomplishment of this project. I am also very thankful for the opportunity of working with other colleagues involved in this research group. The financial support by University of Manitoba and the Natural Sciences and Engineering Council of Canada are greatly acknowledged.

I am sincerely grateful to my father and mother, Valdomiro and Débora, for all their support, love, understanding, and encouragement throughout my life and this accomplishment. I am also thankful to my brother, Gustavo. I sincere thank my true love, Daria, for her immeasurable love, encouragement, and support throughout this journey.

Contents

Abstract ii

Acknowledgements iii

List of Tables viii

List of Figures ix

Nomenclature xv

1 Introduction 1

1.1 Scope of the Research 2

1.2 Thesis Outline 3

2 Research Background 5

2.1 Theoretical Frameworks: Turbulent Flow 5

2.1.1 Summary 13

2.2 Literature Review: Turbulent Flow over a Wavy Bottom Wall Channel . . 13

2.2.1 Wavy Channel Definition 14

2.2.2 Experimental Studies 14

2.2.3 Numerical Studies 19

2.3 Objectives 23

3 Methodology 25

3.1 Experimental Procedure 25

3.1.1 Water channel facility and the PIV system 25
3.1.2 Test Conditions 27
3.1.3 System Components 27
3.1.4 Convergence and Spatial Resolution Tests 30
3.1.5 Measurement Uncertainty 31
3.2 Numerical Procedure 32
3.2.1 Solution domain 32
3.2.2 Boundary Conditions 32
3.2.3 Mathematical Model 34
3.2.4 Numerical solution method 36
3.2.5 Grid independence study 36

4 Experimental Results and Discussions - Wavy Wall 39

4.1 Recirculation Region Characterization 39
4.2 Mean Velocity 43
4.3 Reynolds stresses 49
4.3.1 Reynolds normal stresses 49
4.3.2 Reynolds Shear Stress and the Structural Parameter 53
4.3.3 Reynolds Number Effects in the Reynolds Stresses 57
4.4 Turbulent Kinetic Energy 58
4.4.1 Turbulent Kinetic Energy Production 58
4.5 Summary: Experimental Results 64

5 Numerical Results and Discussions - Wavy Wall **65**

5.1 Mean Velocity and Recirculation Region 65

5.2 Wall Shear Stress Distributions for the Fully Periodic Region 73

5.3 Mean Velocity for the Fully Periodic Region 76

5.4 Reynolds Stresses 79

5.4.1 Reynolds stresses one-dimensional profiles 85

5.5 Summary: Numerical Results 88

Conclusion **89**

References **92**

A Experimental Data Convergence Test **98**

A.1 Sample size 98

A.2 Interrogation Area (IA) 100

B Reynolds Averaged Navier Stokes (RANS) Models **103**

B.1 Two-Equation Eddy Viscosity Models 103

B.1.1 The k–ϵ model 104

B.1.2 The Realizable k–ϵ model 105

B.1.3 The k–ω model 106

B.1.4 The SST model 106

B.2 Second Moment Closure (SMC) models 108

B.2.1 The LRR-IP model 108

B.2.2 The LPS model 110

B.2.3 The SMC-ω model 113

B.3 Near Wall Region Modelling 114

B.3.1 Scalable Wall Functions (SWF) 114

B.3.2 Automatic Wall Treatment (AWT) 115

B.3.3 Enhanced Wall Treatment (EWT) 117

C Approaching Flow Characteristics **119**

C.1 Experimental Investigation 119

C.2 Numerical Modeling of the Inlet Region 127

C.2.1 Flow characteristics 127

D Additional Experimental Results **132**

D.1 Recirculation Region Characterization 132

D.2 Mean Velocity Gradients 135

List of Tables

2.1 Experimental studies summary: turbulent flow over a wavy channel. . . . 16

2.2 Numerical studies summary: turbulent flow over a wavy channel. 20

3.1 Turbulence Models (RANS models) Summary. 35

3.2 Typical wavy module grids 37

3.3 Grid independence study results 38

4.1 Recirculation locations (separation ($\tilde{x}_s$), reattachment ($\tilde{x}_r$), and center ($\tilde{x}_c$)) for Waves 1, 3, 6, 8, and 9 and $\mathrm{Re_b} = 10700$. 41

4.2 Recirculation locations (separation ($\tilde{x}_s$), reattachment ($\tilde{x}_r$), and center ($\tilde{x}_c$)) for Wave 9 and $\mathrm{Re_b} = 5040, 8400, 10700$, and 13040 42

4.3 Experimental studies summary: turbulent flow over a wavy channel. . . . 64

5.1 $\mathrm{RMS}_{\mathrm{RN},\langle U\rangle^*}$ [%] values comparing numerical to experimental data, at $\tilde{x} = 0.5$ 70

5.2 Summary of experimental and numerical results for the recirculation region locations: separation ($\tilde{x}_s$) and reattachment ($\tilde{x}_r$). 72

5.3 $\mathrm{RMS}_{\mathrm{RN},\langle U\rangle^*}$ [%] values comparing numerical to experimental data at Wave 9. 78

5.4 $\mathrm{RMS}_{\mathrm{RN},-\langle uv\rangle^*}$ [%] values comparing numerical to experimental data, for the entire profile and to a near-wall region. 88

5.5 Experimental studies summary: turbulent flow over a wavy channel. . . . 88

C.1 Summary of test conditions and boundary layer parameters for the experiments 122

List of Figures

2.1 Model Domain and Wavy Geometry 14

3.1 Experimental setup: (a) transverse system, (b) Nd:YAG double-pulsed laser, (c) CCD camera, (d) recirculation water channel, which contains both the wavy bottom wall test section (I) and the entrance sand paper sheets (II). 26

3.2 Schematic of the experimental test section. Dashed squares represent the x–y measurement planes and dimensions are in mm. 26

3.3 Mesh details for a typical wavy module using Grid 3. 33

4.1 Contour plots of dimensionless streamwise mean velocity, $\langle U \rangle^*$, at Wave 1 (a), Wave 3 (c), and Wave 9 (e), and dimensionless wall normal mean velocity, $\langle V \rangle^*$, at Wave 1 (b), Wave 3 (d), and Wave 9 (f) for $\mathrm{Re_b} = 10700$. 44

4.2 Profiles of dimensionless streamwise mean velocity, $\langle U \rangle^*$, at Wave 1, 3, 6, 8, and 9, at $\tilde{x} = 0.3$, 0.5, and 0.7, for $\mathrm{Re_b} = 10700$. 46

4.3 Profiles of dimensionless wall-normal mean velocity, $\langle V \rangle^*$, at Wave 1, 3, 6, 8, and 9, at $\tilde{x} = 0.3$, 0.5, and 0.7, for $\mathrm{Re_b} = 10700$. 47

4.4 Profiles of dimensionless streamwise mean velocity, $\langle U \rangle^*$, and wall-normal mean velocity, $\langle V \rangle^*$, at Wave 9 and $\tilde{x} = 0.5$, for $\mathrm{Re_b} = 5040, 8400, 10700, 12000$ [25], and 13040. 49

4.5 Contour plots of dimensionless Reynolds normal stresses in the streamwise direction, $\langle u^2 \rangle^*$, (a, c, e) and in the wall-normal direction, $\langle v^2 \rangle^*$, (b, d, f) at Wave 1, 3, and 9 at $\mathrm{Re_b} = 10700$. 50

4.6 Profiles of dimensionless Reynolds normal stresses in the streamwise direction, $\langle u^2 \rangle^*$, at Wave 1, 3, 6, 8, and 9 at $\tilde{x} = 0.3$, 0.5, and 0.7, for $\mathrm{Re_b} = 10700$. 52

4.7 Profiles of dimensionless Reynolds normal stresses in the wall-normal direction, $\langle v^2 \rangle^*$, at Wave 1, 3, 6, 8, and 9 at $\tilde{x} = 0.3$, 0.5, and 0.7, for $\mathrm{Re_b} = 10700$. 53

4.8 Contour plots of dimensionless Reynolds shear stress, $-\langle uv \rangle^*$, at Wave 1 (a), Wave 3 (c), Wave 9 (e), and structural parameter, $-\langle uv \rangle / 2k$, at Wave 1 (b), Wave 3 (d), and Wave 9 (f), for $\mathrm{Re_b} = 10700$. 54

4.9 Profiles of dimensionless Reynolds shear stress, $-\langle uv \rangle^*$, at Wave 1, 3, 6, 8, and 9 at $\tilde{x} = 0.3$, 0.5, and 0.7, for $\mathrm{Re_b} = 10700$. 55

4.10 Profiles of dimensionless Structural Parameter, $-\langle uv \rangle / 2k$ at Wave 1, 3, 6, 8, and 9 at $\tilde{x} = 0.3$, 0.5, and 0.7, for $\mathrm{Re_b} = 10700$. 56

4.11 Profiles of dimensionless Reynolds normal stresses in the streamwise direction, $\langle u^2 \rangle^*$, wall-normal direction, $\langle v^2 \rangle^*$, and Reynolds shear stress, $-\langle uv \rangle^*$, at Wave 9 and $\tilde{x} = 0.5$, for $\mathrm{Re_b} = 5040, 8400, 10700$, and 13040. 57

4.12 Total turbulent kinetic energy production, ${P_k}^*$, normal component P_n^*, and shear component, P_s^* contours at Wave 1 (a, c, e) and at Wave 9 (b, d, f), for $\mathrm{Re_b} \approx 10700$. 59

4.13 Contours of the individual terms in the total turbulent kinetic energy production in Equation 4.1 at Wave 9, for $\mathrm{Re_b} \approx 10700$. 61

4.14 Dimensionless individual terms of total production of turbulent kinetic energy, P_k, at Wave 9 and $\tilde{x} = 0.3$, 0.5, and 0.7, for $\mathrm{Re_b} \approx 10700$. 62

4.15 Dimensionless individual terms of total production of turbulent kinetic energy, P_k, at Wave 1 and $\tilde{x} = 0.3$, 0.5, and 0.7, for $\mathrm{Re_b} \approx 10700$. 63

5.1 Contour plots of dimensionless streamwise mean velocity, $\langle U \rangle^*$, at $\mathrm{Re_b} = 10700$ for the k–ϵ model (a) at Wave 1 and (b) at Wave 9, and for the SST model (c) at Wave 1 and (d) at Wave 9. 66

5.2 Contour plots of dimensionless streamwise mean velocity, $\langle U \rangle^*$, at $\mathrm{Re_b} = 10700$ for the LPS model (a) at Wave 1 and (b) at Wave 9, and for the LRR-IP model (c) at Wave 1 and (d) at Wave 9. 67

5.3 Eddy viscosity models: Dimensionless mean velocity, $\langle U \rangle^*$, distribution for Waves 1, 3, and 6 at $\tilde{x} = 0.5$ for $\mathrm{Re_b} = 10700$. 68

5.4 SMC models: Dimensionless mean velocity, $\langle U \rangle^*$, distribution for Waves 1, 3 and 6 at $\tilde{x} = 0.5$ for $\mathrm{Re_b} = 10700$. 69

5.5 Two-equation models: Dimensionless wall shear stress, τ_w^*, distribution for Wave 8 at $\mathrm{Re_b} = 10700$. 74

5.6 SMC models: Dimensionless wall shear stress, τ_w^*, distribution for Wave 8 at $\mathrm{Re_b} = 10700$. 74

5.7 Eddy viscosity models: Dimensionless streamwise mean velocity, $\langle U \rangle^*$, distribution for Wave 9, at $\tilde{x} = 0.3$, 0.5, and 0.7 for $\mathrm{Re_b} = 10700$. 76

5.8 SMC models: Dimensionless streamwise mean velocity, $\langle U \rangle^*$, distribution for Wave 9, at $\tilde{x} = 0.3$, 0.5, and 0.7 for $\mathrm{Re_b} = 10700$. 77

5.9 Contour plots of dimensionless streamwise Reynolds normal stresses, $\langle u^2 \rangle^*$, at $\mathrm{Re_b} = 10700$ for the LPS model (a) at Wave 1 and (b) at Wave 9, for the LRR-IP model (c) at Wave 1 and (d) at Wave 9, and for the SMC-ω model (e) at Wave 1 and (f) at Wave 9. 80

5.10 Contour plots of dimensionless wall normal Reynolds normal stresses, $\langle v^2 \rangle^*$, at $\mathrm{Re_b} = 10700$ for the LPS model (a) at Wave 1 and (b) at Wave 9, for the LRR-IP model (c) at Wave 1 and (d) at Wave 9, and for the SMC-ω model (e) at Wave 1 and (f) at Wave 9. 82

5.11 Contour plots of dimensionless Reynolds shear stress, $-\langle uv\rangle^*$, at $\mathrm{Re_b} = 10700$ for the LPS model (a) at Wave 1 and (b) at Wave 9, for the LRR-IP model (c) at Wave 1 and (d) at Wave 9, and for the SMC-ω model (e) at Wave 1 and (f) at Wave 9. 84

5.12 SMC models: Dimensionless streamwise Reynolds normal stresses, $\langle u^2\rangle^*$, distributions at $\mathrm{Re_b} = 10700$ for Wave 9 at $\tilde{x} = 0.3$, 0.5, and 0.7. 86

5.13 SMC models: Dimensionless wall normal Reynolds normal stresses, $\langle v^2\rangle^*$, distributions at $\mathrm{Re_b} = 10700$ for Wave 9 at $\tilde{x} = 0.3$, 0.5, and 0.7. 86

5.14 SMC models: Dimensionless Reynolds shear stress, $-\langle uv\rangle^*$, distributions at $\mathrm{Re_b} = 10700$ for Wave 9 at $\tilde{x} = 0.3$, 0.5, and 0.7. 87

A.1 Results for samples sizes of $N = 2000, 4000, 6000$, and 7500 for the profiles of dimensionless streamwise mean velocity, $\langle U\rangle^*$, and wall normal mean velocity, $\langle V\rangle^*$, at Wave 9 and $\tilde{x} = 0.5$, at $\mathrm{Re_b} = 10700$. 98

A.2 Results for samples sizes of $N = 2000, 4000, 6000$, and 7500 for profiles of dimensionless Reynolds normal stresses in the streamwise direction, $\langle u^2\rangle^*$, wall-normal direction, $\langle v^2\rangle^*$, and the Reynolds shear stress, $-\langle uv\rangle^*$, at Wave 9 and $\tilde{x} = 0.5$, at $\mathrm{Re_b} = 10700$. 99

A.3 Results for samples sizes of $N = 2000, 4000, 6000$, and 7500 for the profiles of dimensionless triple correlations in the streamwise, $\langle u^3\rangle^*$, and wall normal, $\langle v^3\rangle^*$ directions, at Wave 9 and $\tilde{x} = 0.5$, at $\mathrm{Re_b} = 10700$. 99

A.4 Results for IA sizes of $16\times16, 32\times16, 32\times32, 64\times32$, and 64×64 for the profiles of dimensionless streamwise mean velocity, $\langle U\rangle^*$, and wall normal mean velocity, $\langle V\rangle^*$, at Wave 9 and $\tilde{x} = 0.5$, at $\mathrm{Re_b} = 10700$. 101

A.5 Results for IA sizes of 16×16, 32×16, 32×32, 64×32, and 64×64 for profiles of dimensionless Reynolds normal stresses in the streamwise direction, $\langle u^2 \rangle^*$, wall-normal direction, $\langle v^2 \rangle^*$, and the Reynolds shear stress, $-\langle uv \rangle^*$, at Wave 9 and $\tilde{x} = 0.5$, at $\mathrm{Re_b} = 10700$. 102

A.6 Results for IA sizes of 16×16, 32×16, 32×32, 64×32, and 64×64 for the profiles of dimensionless triple correlations in the streamwise, $\langle u^3 \rangle^*$, and wall normal, $\langle v^3 \rangle^*$ directions, at Wave 9 and $\tilde{x} = 0.5$, at $\mathrm{Re_b} = 10700$. 102

C.1 Approaching turbulent flow over the upstream smooth wall channel for the PIV experimental data: (a) dimensionless mean velocity, $\langle U \rangle / U_{in}$; (b) dimensionless mean velocity, U^+, in log-scale, y^+. 123

C.2 Approaching turbulent flow over the upstream smooth wall channel for the PIV experimental data: (a) dimensionless velocity fluctuations in the streamwise direction, u^+; (b) and in the wall-normal direction, v^+; (c) dimensionless Reynolds shear stress, uv^+; (d) dimensionless turbulent kinetic energy, k^+. 124

C.3 Approaching turbulent flow over the upstream smooth wall channel for the two equations eddy viscosity models: (a) dimensionless mean velocity, $\langle U \rangle / U_{in}$; (b) dimensionless viscous mean velocity, u^+, with wall units axis in log-scale, y^+; (c) dimensionless viscous mean velocity, u^+, and wall units, both axes in log-scales; (d) dimensionless turbulent kinetic energy, k^+. . . 128

C.4 Approaching turbulent flow over the upstream smooth wall channel for the SMC models: (a) dimensionless mean velocity, $\langle U \rangle / U_{in}$; (b) dimensionless viscous mean velocity, u^+, with wall units axis in log-scale, y^+; (c) dimensionless viscous mean velocity, u^+, and wall units, both axes in log-scales; (d) dimensionless turbulent kinetic energy, k^+. 129

D.1 Contour plots of mean streamlines at (a) Wave 1, (b) Wave 3, (c) Wave 6 and (d) Wave 9, at $\mathrm{Re_b} \approx 10700$. 133

D.2 Contour plots of forward flow fraction at (a) Wave 1, (b) Wave 3, (c) Wave 6 and (d) Wave 9, at $\mathrm{Re_b} \approx 10700$. 134

D.3 Contour plots of dimensionless mean streamwise velocity, $\langle U \rangle^*$, at (a) Wave 1, (b) Wave 3, (c) Wave 6 and (d) Wave 9, at $\mathrm{Re_b} \approx 10700$. 135

D.4 Contour plots of streamwise and wall normal mean velocity gradients at Wave 9 in the x-direction: (a) $\partial\langle U \rangle/\partial x^\star$ and (c) $\partial\langle V \rangle/\partial x^\star$, and in the y-direction (b) $\partial\langle U \rangle/\partial y^\star$ and (d) $\partial\langle V \rangle/\partial y^\star$. 137

Nomenclature

C	number concentration, $[1/m^3]$
C_p	specific heat, $[\mathrm{J/kg \cdot K}]$
C_f	friction coefficient
C_p	pressure coefficient
D	diffusion coefficient, $[\mathrm{m^2/s}]$
h	half mean channel height, [m]
I	streamwise turbulence intensity
Nu	Nusselt number
P	pressure, $[\mathrm{N/m^2}]$
P^*	dimensionless pressure: $(P - P_{\mathrm{in}})/(0.5\rho_{\mathrm{in}}U_{\mathrm{in}}^2)$
$\mathrm{Re_{in}}$	Reynolds number based on the inlet velocity
$\mathrm{Re_b}$	Reynolds number based on the bulk velocity
T	temperature, [K]
T_b	bulk temperature, [K]
T_{w}^+	dimensionless temperature: T_w/T_τ
$\langle T \rangle^+$	dimensionless mean temperature: $\langle T \rangle / T_\tau$
k	turbulent kinetic energy, $[\mathrm{m^2/s^2}]$
T_u	turbulent intensity
u	velocity fluctuation in the x direction, [m/s]
u_τ	friction velocity, [m/s]
U	instantaneous velocity in the x direction, [m/s]
$\langle U \rangle$	mean velocity in the x direction, [m/s]
$\langle U \rangle^*$	dimensionless $\langle U \rangle$ velocity: $\langle U \rangle / U_b$
$\langle U \rangle^+$	dimensionless $\langle U \rangle$ velocity: $\langle U \rangle / u_\tau$
v	velocity fluctuation in the y direction, [m/s]
V	instantaneous velocity in the y direction, [m/s]
$\langle V \rangle$	mean velocity in the y direction, [m/s]

$\langle V \rangle^*$	dimensionless $\langle V \rangle$ velocity: $\langle V \rangle / U_b$
w	velocity fluctuation in the z direction, [m/s]
W	instantaneous velocity in the z direction, [m/s]
$\langle W \rangle$	mean velocity in the z direction, [m/s]
x	Cartesian coordinate direction, [m]
$\tilde{x}$	dimensionless length: x/λ
y	Cartesian coordinate direction, [m]
y^*	dimensionless length: $y/2h$
y^+	dimensionless wall coordinate: yu_τ/ν
z	cylindrical coordinate direction, [m]
τ_w^*	dimensionless wall shear stress : $\frac{\tau_w}{\frac{1}{2}\rho U_b^2}$
P_w^*	dimensionless wall pressure : $\frac{P_w - P_{w0}}{\frac{1}{2}\rho U_b}$

Greek Letters

λ	wave length, [m]
α	thermal diffusivity, [m^2/s]
ϵ	turbulence dissipation rate, [m^2/s^3]
τ	wall shear stress, [N/m^2]
μ	dynamic viscosity, [$N \cdot s/m^2$]
ν	kinematic viscosity, [m^2/s]
ρ	density, [kg/m^3]
ω	specific turbulence dissipation, [1/s]

Subscripts

i	Einstein summation convention: repeated indices in a single term are summed over 1, 2, and 3.
in	referring to the inlet
rms	root mean square
w	referring to the wall
x	referring to the x direction
y	referring to the y direction
z	referring to the z direction

Superscripts

$*$	dimensionless quantities normalized using U_b or h
$+$	dimensionless quantities normalized using u_τ or y

Acronyms

BSL	Baseline
CCD	charged coupled device
CFD	computational fluid dynamics
DNS	direct numerical solutions
IA	interrogation area
Nd: YAG	neodymium: Yttrium Aluminum Garnet
PIV	particle image velocimetry

LCT	liquid crystal thermometry
LDV	laser Doppler velocimetry
LES	large eddy simulation
LRR-IP	Launder, Reece and Rodi - Isotropization of Production
LRR-QI	Launder, Reece and Rodi - Quasi-Isotropic
RANS	Reynold-averaged Navier Stokes
SAR	super abrasion resistant
SMC	second moment closure
SSG	Speziale, Sarkar and Gatski
SST	shear-stress transport

Chapter 1

Introduction

Turbulent flow occurs in nature and engineering applications. Typical examples in nature are rivers flow, clouds in a storm, volcano eruption, atmospheric and ocean currents. Out of the many occurrences in engineering applications, a few examples are flow in turbines (hydraulic, gas, or wind), flow in pipelines, internal flow in heat exchangers, flow over aircraft wings and vehicles, combustion processes, flow dispersions from a chimney, and jets discharging in air conditioning systems. The study of turbulent flow is essential in those examples for a variety of reasons. In aerodynamic studies of moving objects such as turbines, aircraft, and vehicles, the interest lies in the performance coefficients, such as drag and lift. The degree of understanding and predictive accuracy of turbulent flows can help reduce energy losses, increase performance, and consequently improve the application efficiency.

Turbulence also influences transport of momentum, heat, and mass transfer, has attracted considerable attention due to its industrial importance. A common example is a turbulent flow over structured surfaces (a modulated topology in the wall surface), which occur in many engineering systems. This modulated topology can assume a variety of shapes from simple geometries such as squares or triangles to customized curved shapes. The surface topology could also contain a certain roughness that modulates that surface for its purposes. The applications of modulated topology on the wall surface can be seen in the use of wavy corrugated walls in plate heat exchangers, for example, where the wavy wall increases the transport of momentum, heat, and mass, as described in Kruse *et al.* [1]. In turbulent flow over natural terrains such as ocean and river beds, their topology can be seen as a modulated surface as well, which interferes with the turbulent flow over that particular surface. In recent studies, Hamed *et al.* [2] investigated the flow adjustment when the wall changes from a smooth to one with a modulated surface made of periodic large-scale sinusoidal wavy walls. This geometry also has significance in gas flows over liquids, the flowing gas sees the liquid

as something like a wavy wall, as noted by De Angelis *et al.* [3]. The problem of a modulated topology in the wall surface using a sinusoidal geometry has attracted many researchers for decades and it is still of strong engineering interest. Moreover, a thorough understanding of turbulent flow over structured surfaces is essential to the design and performance in many applications.

There are two main perspectives to be considered when studying turbulent flows. The first view is the further advancement of the understanding of the physical phenomena itself, which is of keen interest to the research community because of turbulence physics is still an unsolved problem. Physical understanding of turbulence can encompass a vast range of areas, from single point statistical moments to spatial and temporal structures of the turbulent flow. The second view is the creation of suitable mathematical models that can be numerically solved to predict the behaviour of turbulent flows. The advances of computational resources have made possible a wide range of tools that can provide simulations that can aid design engineering. However, when modelling turbulent flows, the shortcomings of some of the currently available models can become an obstructive factor to solving some engineering problems. The designer must not only have resources but adequate knowledge on the different turbulence modelling options.

1.1 Scope of the Research

The scope of the current research project encompassed the use of experimental and numerical techniques to investigate the turbulent flow over a modulated surface, specifically a sinusoidal wavy shape which is described in Section 2.2.1. A comprehensive literature review of research involving flow over sinusoidal wavy walls is presented (Section 2.2) to provide a further understanding of the problem and the state of knowledge on this topic. The literature review revealed that previous experimental and numerical work established the characteristics of the flow in the fully periodic region. However, the non-periodic region has not been thoroughly

investigated. This particular geometry provided the opportunity to further explore turbulent flow statistics for the non-periodic region along the wavy bottom wall in a channel. The literature review also shown that a Reynolds number range ($Re_b \approx 3000$ to 13000), the separation and reattachment of the flow was present in the averaged statistical quantities for wavy geometries of $\frac{\lambda}{a} = 10$ or 20. The current research focused on a similar geometry and Reynolds number, in order to study the flow separation and reattachment along the wavy channel. Moreover, it was also possible to compare numerical studies to previous experimental data for validation in the fully periodic region for specific statistical quantities. The heat transfer enhancement is also of interest in some engineering applications, such as heat exchangers that use this type of geometry modulation. Scenarios, where heat transfer was present, were beyond the scope of the results presented in this project. However, several works studied heat transfer along with the turbulent flow statistics in the literature. They showed the close correlation between turbulent flow and heat transfer phenomena.

1.2 Thesis Outline

In Chapter 2, background information is thoroughly presented. First, a theoretical framework on turbulent flows (Section 2.1) provides the necessary information needed to interpreted the literature review and the results. The literature review (Section 2.2) presents experimental and numerical studies of turbulent flows in a channel with a wavy bottom wall. Chapter 3 presents the methodology for both the experimental and numerical studies. Section 3.1 describes the experimental procedures, which contains a description of the test facilities, test conditions, PIV system, measurement procedures, uncertainty and convergence studies. Section 3.2 presents the numerical procedure, which includes the description of the mathematical models, grid generation, and numerical solution methods.

Chapter 4 presents the experimental results. Single-point statistics, such as mean velocity, Reynolds stresses, and turbulent kinetic energy production are presented in both the

non-periodic and fully periodic regions. New experimental data for the flow development upstream of the fully periodic condition are presented to further improve the understanding of the flow physics for this region. Chapter 5 presents the numerical results produced using a variety of turbulence models. Results for the mean velocity, wall shear stress, and Reynolds stresses are presented for the same regions as in the experiments. The new experimental data for the flow development region was used in the assessment of the turbulence models. A conclusion presents the significant outcomes of this work, the lessons learned, and future work recommendations.

Appendix A presents the experimental data convergence tests. The Reynolds Averaged Navier Stokes (RANS) models formulations are described in Appendix B. A description of the approaching flow conditions is in Appendix C for both experimental and numerical studies provides an appropriate description of the incoming boundary conditions prior to the wavy channel for the problem. Additional experimental results are presented in Appendix D.

Chapter 2

Research Background

2.1 Theoretical Frameworks: Turbulent Flow

As mentioned earlier, turbulent flow occurs in diverse applications. Due to its complex nature, it presents a challenge regarding understanding the flow physics and its modelling. These have attracted the scientific community for a considerable amount of time, and it still is an active research topic. One of the first turbulent flow visualizations is from more than 500 years ago, by Leonardo da Vinci [4]. He was able to characterize the flow as random and unpredictable phenomena. A precise definition of turbulent flow is not possible. The key characteristics of turbulence, as presented in Tennekes and Lumley [5], are irregularity, diffusivity, large Reynolds number, three-dimensional, rotational, dissipative, and a continuum phenomenon. Nevertheless, each turbulent flow is different even if they present similar characteristics [5].

Flow observation is a conventional technique employed to investigate turbulent flows. In the earliest flow observations, the scientific community was restricted to qualitative descriptions based on observation of nature. The technique then evolved to more controlled environments using water and wind channels, which was still limited to qualitative studies. Eventually, experimental techniques progressed to a stage, where quantitative statistical information could be accurately obtained from measurements methods that are based on taking images of the flow. Laser Doppler Velocimeter (LDV) and Particle Image Velocimetry (PIV) are examples of these experimental techniques. Quantitave flow statistics obtained from the techniques are used for the validation of turbulence flow models implemented in Computational Fluid Dynamics (CFD) simulations.

Since turbulent flows are random and irregular, statistical description of turbulent flow

is a common approach used to study turbulence. As mentioned in Ting [6] the statistical characteristics are reproducible. For this reason, statistical methods are useful for the study of turbulence. In turbulent flows, both the mean and fluctuating velocity components are also of interest. In Equation 2.1, U represents the instantaneous velocity component, in terms of its averaged value, $\langle U \rangle_i$, and its fluctuation, u_i. The subscript i is a free index which can take on the values 1, 2, 3. Thus Equation 2.1 is in fact three separate equations, one for each direction of the Cartesian coordinate system.

$$U_i = \langle U \rangle_i + u_i \tag{2.1}$$

The velocity fluctuations can be analyzed to understand the level of turbulence in a certain flow condition, where the fluctuations of the velocity components characterize the degree of turbulence within the flow.

Reynolds-Averaged Governing Equations

The most common statistical description of turbulent flow is based on the averaged governing equations, commonly referred as Reynolds-averaged Navier-Stokes (RANS) equations [5,7–10]. The averaging makes use of the approach presented in Reynolds [11], where the instantaneous components are decomposed into mean and fluctuating components (Eq. 2.1). The mean and fluctuating components replace the instantaneous terms in the Navier-Stokes equations, which are then averaged to produce the well known RANS equations. For incompressible, steady-state flow, of a Newtonian fluid, the continuity and momentum equations are defined in Equation 2.2 and 2.3 below:

$$\frac{\partial \langle U \rangle_i}{\partial x_i} = 0 \tag{2.2}$$

$$\underbrace{\rho \langle U \rangle_j \frac{\partial \langle U \rangle_i}{\partial x_j}}_{\text{I}} = \overbrace{-\frac{\partial \langle P \rangle}{\partial x_i}}^{\text{II}} + \underbrace{\frac{\partial}{\partial x_j}\left[\mu(\frac{\partial \langle U \rangle_i}{\partial x_j})\right]}_{\text{III}} - \overbrace{\rho \frac{\partial \langle u_i u_j \rangle}{\partial x_j}}^{\text{IV}} \tag{2.3}$$

where ρ is the density, $\langle P \rangle$ is the mean static pressure, and μ is the dynamic viscosity. The terms identified in Equation 2.3 are: I: convection term, II: pressure term, III: viscous diffusion term, and IV: Reynolds stress term. The Reynolds stress term in Equation 2.3 generated nine new terms, but there are only 6 independent terms, due to symmetry. Thus, the Reynolds averaging approach generated a total of ten unknowns that exceed the four available mean flow equations (Equation 2.3 and 2.3). It is not possible to have a closed set of equations for turbulent flow. This issue is known as the turbulence closure problem, and is discussed in Section 2.1.

An equation can also be derived for the Reynolds stress itself as shown in Eq. 2.4, as presented in [4, 9].

$$\underbrace{\rho \langle U \rangle_j \frac{\partial \langle u_i u_k \rangle}{\partial x_j}}_{C_{ij}} = \overbrace{\left\langle p \left[\frac{\partial u_i}{\partial x_k} + \frac{\partial u_k}{\partial x_i} \right] \right\rangle}^{\phi_{ij}} \underbrace{-\rho \left[\langle u_i u_j \rangle \frac{\partial u_k}{\partial x_j} + \langle u_k u_j \rangle \frac{\partial u_i}{\partial x_j} \right]}_{P_{ij}}$$
$$\underbrace{-\frac{\partial}{\partial x_j} \{ \langle p u_k \rangle \delta_{ij} + \langle p u_i \rangle \delta_{kj} \}}_{D^p_{ij}} \underbrace{-\frac{\partial}{\partial x_j} \{ \rho \langle u_i u_k u_j \rangle \}}_{D^t_{ij}} \underbrace{-\frac{\partial}{\partial x_j} \{ 2\mu [\langle s_{ij} u_k \rangle + \langle s_{kj} u_i \rangle \}}_{D^\mu_{ij}} \tag{2.4}$$
$$\underbrace{-2\mu \left[\left\langle s_{ij} \frac{\partial u_k}{\partial x_j} \right\rangle + \left\langle s_{ij} \frac{\partial u_i}{\partial x_j} \right\rangle \right]}_{\epsilon_{ij}}$$

where p is the fluctuating static pressure, δ_{ij} is the Kronecker delta, $s_i s_j$ is the fluctuating strain rate defined in Equation 2.5.

$$s_{ij} = \frac{1}{2} \left(\frac{\partial u_i}{\partial x_j} + \frac{\partial u_j}{\partial x_i} \right) \tag{2.5}$$

Equation 2.4 is of great relevance in turbulence because its understanding can reveal the interaction between the turbulence motion and the mean flow. The individual terms in Equation 2.4 are important for the understanding of turbulence and its modelling and are identified as follows: C_{ij}: convection term ϕ_{ij}: pressure-strain rate term P_{ij}: production

term D_{ij}^{p}: pressure diffusion term D_{ij}^{t}: turbulent diffusion term D_{ij}^{μ}: molecular diffusion term and ϵ_{ij}: dissipation term.

The turbulent kinetic energy (TKE), k, is also an important quantity for studying turbulent flows and is defined as, $k = 0.5(\langle u^2 \rangle + \langle v^2 \rangle + \langle w^2 \rangle)$. The transport equation for the TKE is Equation 2.6 [4].

$$\underbrace{\rho \langle U \rangle_j \frac{\partial \langle k \rangle}{\partial x_j}}_{\text{I}} = \underbrace{-\frac{\partial}{\partial x_j} \{\langle p u_i \rangle \delta_{ij}\}}_{\text{II}} \underbrace{-\frac{\partial}{\partial x_j} \left\{\frac{\rho}{2} \langle u_i u_i u_j \rangle\right\}}_{\text{III}} \underbrace{+\frac{\partial}{\partial x_j} \{2\mu \langle s_{ij} u_i \rangle\}}_{\text{IV}} \underbrace{-\rho \langle u_i u_j \rangle \frac{\partial \langle U \rangle_i}{\partial x_j}}_{\text{V}} \underbrace{-2\mu \langle s_{ij} s_{ij} \rangle}_{\text{VI}} \tag{2.6}$$

The terms in Equation 2.6 are identified as follow: I: convection by the mean flow, II: pressure diffusion, III: turbulent diffusion term, IV: molecular diffusion, V: turbulent production, and VI: dissipation rate.

In cases where the study of the temperature or concentration field is of interest, a similar procedure used to obtain the conservation of momentum equation can be employed to obtain the Reynolds averaged governing equations for those scalar quantities. The energy equation for temperature is presented in Equation 2.7, and the concentration equation in Equation 2.8.

$$U_j \frac{\partial \langle T \rangle}{\partial x_j} = \frac{\partial}{\partial x_j} \left[\alpha \left(\frac{\partial \langle T \rangle}{\partial x_j} + \frac{\partial \langle T \rangle}{\partial x_i}\right)\right] - \frac{\partial \langle u_i T' \rangle}{\partial x_j} \tag{2.7}$$

$$U_j \frac{\partial \langle C \rangle}{\partial x_j} = \frac{\partial}{\partial x_j} \left[D \left(\frac{\partial \langle C \rangle}{\partial x_j} + \frac{\partial \langle C \rangle}{\partial x_i}\right)\right] - \frac{\partial \langle u_i C' \rangle}{\partial x_j} \tag{2.8}$$

where T is the mean temperature, α is the thermal diffusivity, $T^{'}$ is the fluctuating temperature, C is the number concentration, and C' is the fluctuating concentration. Note the $\langle u_i T' \rangle$ and $\langle u_i C' \rangle$ terms which are the energy and mass transport equivalents of the Reynolds stresses.

The analysis of the different terms in all the governing equations presented here can clarify and advance the understanding of turbulence. The averaged governing equations are

also essential for the understanding of the quantities studied in experiments. They also form the basis for the closure problem discussions and turbulence modelling equations discussed next.

Turbulence Closure Problem and modelling

On the one hand, the original Navier-Stokes equations are a closed problem, where the unknowns variables match the number of equations. On the other hand, the Reynolds-averaged Navier-Stokes equations (Eq. 2.3 to 2.6) are not closed because the Reynolds averaging approach generated 6 new unknowns for a total of ten unknowns that exceed the four available mean flow Equation 2.2 and 2.3. The derivation of a Reynolds stress Equation 2.4 linking the Reynolds stresses with the mean motion generated another seventy-five unknowns that again exceed the ten available equations (Eq. 2.2, 2.3, and 2.4). The objective of obtaining an Reynolds stresses transport equation that relate the Reynolds stresses and the mean flow motion has in fact created a more complex equation set, which is also not closed. It is necessary to close the equations to implement those equations in a RANS model CFD simulation. There are several approaches to close the RANS equations. Thus commonly used approaches to close the system are eddy viscosity and second moment closure.

The eddy viscosity method uses the Boussinesq approximation to close the momentum Equation 2.3. This method in analogous to the relation between the viscous stress and the flow motions; it relates the Reynolds stress to the mean velocity gradient via a turbulent eddy viscosity as given in Equation 2.9:

$$-\rho \langle u_i u_j \rangle = \mu_t \left(\frac{\partial \langle U_i \rangle}{\partial x_j} \right) - \frac{2}{3} \delta_{ij} \rho k \tag{2.9}$$

In Equation 2.9, μ_t is the turbulent dynamic eddy viscosity. This approximation replaces the Reynolds stress term in Equation 2.3. Detail of this is presented in Section B.1. This method is used in zero-equation, one- equation or two-equation eddy viscosity models. In the

two-equation eddy viscosity models, two additional transport equations are solved. They are considered to be complete models when compared to zero or one equations models. There are several two-equation models in the literature, and include the following models: standard k–ϵ [12], Realizable k–ϵ [13], k-ω [14], and the SST and BSL models [15]. The eddy viscosity models implemented in this study are discussed in detail in Sections 3.2.3 and B.1.

As mentioned in Dewan [10], models that make the use of the Boussinesq approximation have limitations because of two main assumptions: first, that the Reynolds stresses are proportional to the mean strain rate, and second, that eddy viscosity is assumed to be isotropic; the various Reynolds stress (both normal and shear) components are considered to be equal between them. These two assumptions are particularly problematic in situations where the flow contains significant mean strain rates, curvatures or rotation. In wall-bounded turbulent flows, a critical portion of the flow is in the near wall regions. This region represents a modelling challenge for RANS models because it is profoundly affected by viscosity. Note that TKE is reduced to zero at the wall. A number of near-wall treatments have been developed to model this region [8, 16] and a description of the techniques used in this study are presented in Section B.1.

The eddy viscosity approach closes Equation 2.3, where as the Second-Moment Closure (SMC) method closes Equation 2.4 instead. The SMC models solve the individual components of the Reynolds stress given in Equation 2.4. The solution of the individual equations for each Reynolds stress provides, in theory, a more accurate prediction of the Reynolds stress and turbulence anisotropy [8]. Nonetheless, it is necessary to model high order moments that appear in the Reynolds stress transport equation (Eq. 2.4). Therefore, the accuracy of the solution is intimately linked to the accuracy of the models for these higher order terms. As mentioned in Sandham *et al.* [8], these models do not always live up to expectation, i.e, show better predictions than the two-equation models. Particular attention to the wall regions is also necessary for the SMC models, as detailed in Section B.1. Further details on SMC models are described in Section B.2.

Sandham *et al.* [8] provided detailed discussion on the various strategies available to solve the closure problem. They considered the RANS model approach to be a robust, easy to use and cost-effective flow-prediction tool. They argued that the RANS models are relatively cheaper methods to compute turbulent flows when compared to more advanced numerical simulations, such as Large Eddy Simulations (LES) and Direct Numerical Simulations (DNS).

DNS solves the partial differential equations for the instantaneous quantities and therefore does not require any modelling. However, DNS requires enormous amount of computational resources, which restricts its use to relatively low Reynolds numbers and simple geometries [10]. The LES technique also solves the instantaneous flow quantities but only for the large scales of turbulence, while the small scales are modeled [10]. LES is computationally less demanding than DNS, and it presents great potential to become a design tool. As will be discussed later, numerous numerical studies for wavy walls were solved using LES and DNS methods. Even though LES and DNS could have been used for this present study, the purpose of the study is to explore further the use of RANS models that are commonly used in industry today.

In the past few decades, Computational Fluid Dynamics (CFD) simulations have gained significant importance in the design process in many industries and the turbulence research community. CFD uses a set of appropriate governing equations that are solved numerically for a particular computational domain. The majority of the engineering applications of interest involve the simulations of turbulent flows, which are only possible when one has the appropriate governing equations that can be numerically solved to describe the flow. CFD simulations are now extensively used to evaluate engineering systems performance, and, in most of the cases, the CFD codes rely on Reynolds-Averaged Navier-Stokes (RANS) turbulence models.

Turbulence modelling for Separated Flows: Two-Equations and SMC models

An important phenomena that occurs in the flows of interest of this work is flow separation. Therefore, this section presents a brief discussion of how different turbulence models performed for a few turbulent flow applications in which flow separation occurs. Iaccarino [17] tested a low-Reynolds number version of the Launder and Sharma k–ϵ model [18]. This model makes the use of damping functions in the near wall region. They also implemented the $\overline{v'^2}$-f model, which models the near-wall without the need for damping or wall functions. Their geometry of interest was a channel diffuser, where flow separation occurs. The low-Reynolds number k–ϵ model failed to predict flow recirculation, justified by its incapability to capture the adverse pressure gradient. The $\overline{v'^2}$-f model predicted the recirculation size reasonably well, but it underestimated the maximum negative velocities in the recirculation region. The turbulent kinetic energy k was also compared to both models and even though the $\overline{v'^2}$-f model captured flow separation, and the turbulent intensities in the diffuser, it under-predicted the intensities' values in the region after the reattachment. The low-Reynolds number k–ϵ model had a very poor prediction of k. In conclusion, their work demonstrated the importance of the turbulence model selection, and that results from turbulence model such as the $\overline{v'^2}$-f model compared very well with experiments and LES results.

Pathak *et al.* [19] implemented both the standard k–ϵ and a SMC model. Their studies considered a heated turbulent jet into a cross flow, which is characterized by considerable three-dimensional effects, and is highly anisotropic. They found that the SMC model matched well with experimental data and its performance was better than the standard k–ϵ model. Paul *et al.* [20] used four turbulence models, k–ϵ [12], k–ω [14], SST model [15], and SMC model refereed here as LRR-IP model [21] for a turbulent cross-flow in a staggered tube bundle. Their study revealed that the overall performance of the two equations models was better than the SMC model.

2.1.1 Summary

The overview on turbulent flow physics presented some of its features, the challenges in understanding turbulence, and experimental approaches used to study turbulent flow statistics and investigate flow structures within a turbulent flow. The RANS equations for turbulent flows and some of the modelling techniques available in the literature are also presented. It was demonstrated that a wide variety of options can be employed to study and predict turbulent flows. A few examples of RANS turbulence model predictions for separated flow cases demonstrated that SMC models do not always produce superior performance than two-equation models and that some of the RANS models can predict accurate results even when compared to LES simulations.

2.2 Literature Review: Turbulent Flow over a Wavy Bottom Wall Channel

This section provides a detailed overview of the experimental and numerical studies of flow in a channel with a wavy bottom wall, based on the geometry definition in Section 2.2.1. It provides insights into the turbulence flow characteristics studied by previous authors, and it brings this study in perspective to the current stage of the research for this particular problem for both experimental and numerical approaches. Considerable research has been undertaken in the past to understand the turbulence characteristics of this flow, which are quite complicated compared to canonical turbulent flows over flat walls because of repeated flow separation and reattachment. The geometry not only presents a challenge for turbulent flow understanding, but it also has a wide variety of engineering applications, which makes its study relevant.

2.2.1 Wavy Channel Definition

The geometry of interest in this study is shown in Figure 2.1, where $2h$ is the mean channel height, y_{wall} is the bottom surface position, λ is the wave length, and a is the wave amplitude. Note that y_{wall} is equal to zero at the mean wave level, equal to a at $\tilde{x} = 0.0$, and equal to $-a$ at $\tilde{x} = 0.5$, where $\tilde{x}$ is a local definition of position along each wave.

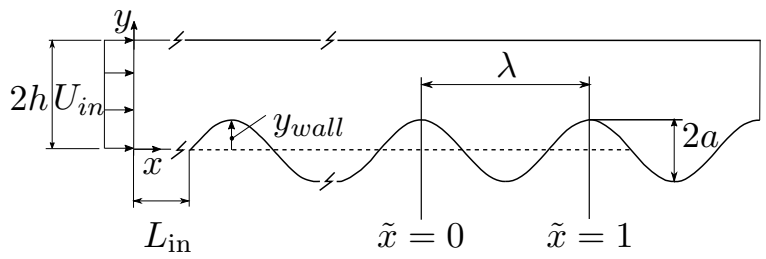

Figure 2.1: Model Domain and Wavy Geometry

The bulk Reynolds number, Re_b, is defined in Equation 2.10 in terms of the half channel height, h, and bulk velocity, U_b, where ρ is density and μ is the dynamic viscosity.

$$\text{Re}_\text{b} = \rho U_b h/\mu \tag{2.10}$$

The U_b value is obtained from the local velocity profile, $U(y)$, in Equation 2.11.

$$U_b = (2h - a)^{-1} \int_{y_{\text{wall}}=a}^{2h} U(y)dy \tag{2.11}$$

The wavy surface position y_{wall}, defined in Equation 2.12, was used to define both the experimental and numerical geometry.

$$y_{\text{wall}} = a\ \cos(2\pi\tilde{x}) \tag{2.12}$$

2.2.2 Experimental Studies

Relevant experimental studies are listed in Table 2.1 in chronological order. The table contains the following information for each article: the experimental method, main geometrical

features ($\frac{\lambda}{a}$ and $\frac{(2h+a)}{a}$), bulk Reynolds number ($\mathrm{Re_b}$), and flow quantities studied.

The fully periodic region findings will be discussed first, and later in the experimental literature review, the development region is presented and discussed. Results from the fully periodic region in Zilker *et al.* [22], Zilker and Hanratty [23], and Kuzan *et al.* [24] demonstrated that the flow regime changes from a non-separated to a separated regime with a decrease in λ/a. Zilker and Hanratty [23] observed that reverse flow is possible for λ/a smaller than 60.6. They also concluded that the Reynolds number range where reverse flow exists increases with a decrease in λ/a. Zilker *et al.* [22] also focused their work on evaluating linearized momentum equations to describe non-separated flows, where pressure, shear stress and velocity profiles were well predicted. Those results and non-separated flows are not further reviewed here because the current study is focused on separated flow conditions.

The works from Zilker *et al.* [22] and Zilker and Hanratty [23] did not examine the wavy wall effects on higher order turbulence statistics. It can be seen in Table 2.1 that a more in-depth study of the turbulent flow statistics started with Buckles *et al.* [25] and Kuzan *et al.* [24]. These works investigated the streamwise turbulence intensities, $\sqrt{\langle u'^2 \rangle}$. The term under the square root is also know as the streamwise Reynolds normal stress. Buckles *et al.* [25] and Kuzan *et al.* [24] studied the flow physics of a turbulent flow over a large amplitude wavy surface with flow separation, with $\lambda/a = 10$. Their velocity measurements revealed an inner boundary layer formation downstream from the reattachment location. This thin inner boundary layer moves away from the wall at the separation point and forms a free shear layer.

Hudson *et al.* [26] extended previous authors' findings by studying the Reynolds shear stress and the turbulent kinetic energy production. Their studies concluded that the separated shear layer is characterized by large Reynolds shear stress values, which lead to high turbulent production in the inner region of the flow. The inner region is defined as the region where the wavy wall effects is significant.

Table 2.1: Experimental studies summary: turbulent flow over a wavy channel.

Source	Year	Method	$\frac{\lambda}{a}$	$\frac{(2h+a)}{a}$	Reynolds Number	Flow Quantities Studied
Zilker *et al.* [22]	1977	hot-film probe, electrochemical,	160 40	161 41	2727 to 15325 3087 to 16328	τ_w^*, P_w^* , and $\langle U \rangle^*$
Zilker and Hanratty [23]	1979	hot-film probe, electrochemical,	40 10	41 11	2564 to 15384 4611 to 8811	τ_w^*, P_w^*, and $\langle U \rangle^*$
Buckles *et al.* [25]	1984	LDV	10	10.33	12000	τ_w^*,P_w^*,U^+, $\langle U \rangle^*$, $\sqrt{u'^2}^*$, $\sqrt{p'^2}^*$, S_u, and F_u
Kuzan *et al.* [24]	1989	LDV	40 10	41 11	8500 4000 to 30000	$\langle U \rangle^*$, U^+, $\sqrt{u'^2}^*$ P_w^*, τ_w^*
Hudson *et al.* [26]	1996	LDV	20	21	3380	$\langle U \rangle / u_\tau$,$\langle V \rangle / u_\tau$,$\sqrt{u'^2}/u_\tau$, $\sqrt{\langle v'^2 \rangle}/u_\tau$,$\langle -uv \rangle / {u_\tau}^2$,$P_k$
Kruse *et al.* [27]	2003	PIV	10	11	4500	$u/\langle U \rangle$ and POD_u

Continued on next page

Table 2.1 – continued from previous page

Source	Year	Method	$\frac{\lambda}{a}$	$\frac{(2h+a)}{a}$	Reynolds Number	Flow Quantities Studied
Gunther and von Rohr [28]	2003	PIV	20	21	500 to 7300	u'^*, v'^*, $\langle U\rangle^*$, $\langle V\rangle^*$, $\sqrt{u'^2}^*$, $\sqrt{v'^2}^*$, $-\langle uv\rangle^*$, and POD_k(u and v)
Kruse *et al.* [1]	2006	PIV	10 20	11 21	11200	U^+,$\langle U\rangle/u_\tau$, $\sqrt{u'^2}$, $\sqrt{v'^2}$, R_{uv}, P_k, k, τ, POD_k, and POD_{uv}
Kruse and Rudolf von Rohr [29]	2006	PIV; LCT	20	21	2400 to 20500	$\langle U\rangle^*$, $\langle V\rangle^*$, T^*, $\sqrt{u'^2}^*$, $\sqrt{v'^2}^*$, $\sqrt{T'^2}^*$, R_{uv}, R_{uT}, R_{vT}, and POD_k
Wagner *et al.* [30]	2007	PIV	20	21	2800 to 11200	$\langle U\rangle^*$, $\sqrt{u'^2}^*$, $\sqrt{v'^2}^*$ $\langle c\rangle/c_0$, and c'/c_0
Hamed *et al.* [31]	2015	PIV	20	23.5	4000 and 40000	u^*, v^*, $\langle U\rangle^*$, $\langle V\rangle^*$, k^*, P_k, $-\langle uv\rangle^*$, and POD_k
Hamed *et al.* [2]	2017	PIV	20	23.5	36900 41200	$\langle U\rangle^*$, k, and $-\langle uv\rangle^*$

Kruse *et al.* [27] investigated the flow dynamics by analyzing the temporal flow behavior and stated that the large-scale flow structures provide a mechanism for momentum or scalar transport between the wavy wall and the bulk fluid. Kruse *et al.* [1] showed that Reynolds stresses, Reynolds stress correlations, and turbulent kinetic energy in the outer flow are independent of turbulence generated at the wall. Kruse *et al.* [1] also confirmed the large values of the production associated with the development of the shear layer, in particular at the shear layer initiation. In Kruse *et al.* [29], particle image velocimetry (PIV) and liquid crystal thermometry (LCT) techniques were used to include heat flux measurements in a wavy channel flow. They found that low-momentum high-temperature fluid coming from the heated wall replaces high-momentum lower-temperature liquid, which advects towards the wall. This study reinforced the argument that such geometries are beneficial to heat exchangers applications, as they promote flow mixing.

Gunther and Rohr [28] further investigated the flow over the same wavy geometry as in Hudson *et al.* [26] by performing Proper Orthogonal Decomposition (POD) of the streamwise velocity component with the snapshots method. POD is a mathematical approach often used to characterize the behaviour of large scale flow structures [27, 28]. Gunther and Rohr [28] revealed that the POD mode 1 contributed to 33% of the turbulent kinetic energy, for a sample size of 250 at $\mathrm{Re_b}$=3350, and their studies gave insights into the large-scale three-dimensional flow structures in separated flow over waves. Kruse *et al.* [27] performed a POD analysis, for a $\lambda/a = 10$ and showed that POD modes 1 and 2 contributed 25 % of the turbulent kinetic energy, for a sample size of 900 at $\mathrm{Re_b}$=4500. They also investigated the flow dynamics by analyzing the temporal flow behavior and stated that the large-scale flow structures provide a mechanism for momentum or scalar transport between the wavy wall and the bulk fluid.

Hamed *et al.* [31] also identified the shear layer that enhances turbulence that was noted by previous authors for the 2D wavy wall. Their work also included a 3D wavy wall case which defined an additional wave in the spanwise direction superimposed on the 2D wall. The

3D wall geometry presents different flow dynamics with significantly lower turbulence levels than for the 2D wall. In Hamed *et al.* [2], further results are presented for 2D and 3D wavy walls for higher Reynolds numbers. The development of the flow was investigated to assess the turbulent boundary layer adjustment to a 3D topography and differences compared to a 2D wavy wall. Wagner *et al.* [30] focused on scalar transport involving a point source in turbulent flow over wavy walls. They found that the wavy geometry and flow field interaction governed the scalar transport and that large-scale structures of the velocity caused very good mixing of the tracer dye introduced at the scalar source point.

The majority of the previous work studied only the region where the flow statistics are periodic. The flow development region, however, is also of great importance because in real engineering applications the flow conditions are not always periodic and regions of development are present. In a recent paper, Hamed *et al.* [2] clearly stated that the flow development remains an open problem for wavy walls. Discussions of the flow development at the wavy section are brief in most of the previous experimental results. Zilker *et al.* [22] showed no significant changes in the wall shear stress after the second wave, for a geometry with $\lambda/a = 64$ for a case with no flow separation. Buckles *et al.* [25] demonstrated flow periodicity by comparing the streamwise mean velocities and turbulence intensities at $\tilde{x} = 0$ and $\tilde{x} = 1.0$ at the eighth wave.

2.2.3 Numerical Studies

Relevant earlier numerical studies are summarized in Table 2.2. Direct Numerical Simulation (DNS) was used in [3, 32–35]. Maass and Schumann [32, 33] investigated turbulent flow over a wavy wall and demonstrated good agreement with experimental data [26] for the mean velocity and Reynolds stresses, but the recirculation size was twice the size observed in the experiment [26]. De Angelis *et al.* [3] predicted reattachment at $\tilde{x} = 0.73$, which is 46% higher than the value in the Hudson *et al.* [26] experiments.

Table 2.2: Numerical studies summary: turbulent flow over a wavy channel.

Source	Year	Method	$\frac{\lambda}{a}$	$\frac{(2h+a)}{a}$	Reynolds Number	Flow Quantities Studied	Data used
Patel *et al.* [36]	1991	RANS: k–ϵ	10	11	8160		[25]
Maass and Schumann [32]	1994	DNS	20	21	2390	$\langle U\rangle$,$-\langle uv\rangle^*$,$\langle v^2\rangle^*$,$\langle u^2\rangle^*$	[26]
						P_w^*	
Maass and Schumann [33]	1996	DNS	20	21	3380	$\langle U\rangle^*$, $\langle V\rangle^*$, $\sqrt{u'^2}^*$, $\sqrt{v'^2}^*$,	[26]
						$\sqrt{w'^2}^*$, $-\langle uv\rangle^*$, $\langle P\rangle^*$	
De Angelis *et al.* [3]	1997	DNS	20	20.23	3300	$\langle U\rangle^*$,$\sqrt{u'^2}^*$,$\sqrt{v'^2}^*$,$\sqrt{w'^2}^*$	[22, 25]
			40	20.13		P^*, τ_w^*,$-\langle uv\rangle^*$, P_k,	[26]
						and TKE Budget Terms.	
Cherukat *et al.* [34]	1998	DNS	20	21	3460	u,v, $\langle U\rangle^*$, U^+,$\langle V\rangle^*$,$\sqrt{u'^2}^*$	[26]
						$\sqrt{v'^2}^*$,$\sqrt{w'^2}^*$,$-\langle uv\rangle^*$,k,	
						τ, τ_w^*,$\sqrt{\langle p'^2\rangle}^*$,$\langle P\rangle^*$,$P_k$	
Henn and Sykes [37]	1999	LES	10	10	10600	u and v (velocity vector),	[25]
			16	17	10800	$\langle U\rangle^*$, ψ, $\sqrt{u'^2}^*$, $\sqrt{v'^2}^*$,	
			20	21	10580	$\sqrt{w'^2}^*$, $-\langle uv\rangle^*$, S_u, F_u,	[26]
			40	41	11050	P_w^*, τ_w^*	
			64.5	65.5	6560		[23]

Continued on next page

Table 2.2 – continued from previous page

Source	Year	Method	$\frac{\lambda}{a}$	$\frac{(2h+a)}{a}$	Reynolds Number	Flow Quantities Studied	Data used
Cui *et al.* [38]	2003	LES	10	11	10000	$\langle U\rangle^*$, k, U^+	[25]
Dellil *et al.* [39]	2004	RANS: k–ϵ	10 to 50	11 to 51	3380	$\langle U\rangle^*$,k,T^+,I, C_f, C_p T, Nu_x, $\langle \mathrm{Nu}\rangle$	[33]
Yoon *et al.* [35]	2009	DNS	20 to 100	21 to 101	3380	u, $\langle U\rangle^*$, $\langle V\rangle^*$,k,$-\langle uv\rangle^*$, P_w^*, τ_w^*, C_f, and C_p	[33, 34]
Wagner *et al.* [40]	2011	LES	20	21	5600 15000	$\langle U\rangle^*$, U^+ $\langle V\rangle^*$, $\langle u^2\rangle^*$, $\langle v^2\rangle^*$, $\langle w^2\rangle^*$, $-\langle uv\rangle^*$, C_f, T_w^+, $\langle T\rangle^+$, $\langle \mathrm{Nu}\rangle$, $\langle T'T'\rangle^*$, $\langle u'T'\rangle^*$, $\langle v'T'\rangle^*$	[30, 33]
Knotek and Jicha [41]	2012	RANS:k–ω SST,k–ϵV2F	20	21	3380	P_w^*, τ_w^*, $\langle U\rangle^*$, $\langle V\rangle^*$,	[35]
Khaled *et al.* [42]	2015	RANS: k–ϵ	20	21	3380	$\langle U\rangle^*$, $\langle V\rangle^*$, C_f,and Nu_x	[33]

The De Angelis *et al.* [3] work also included an in-depth analysis on turbulent flow structures and the TKE budget terms. Their study has a complete TKE budget analysis, which includes turbulent production, pressure diffusion, turbulent diffusion, pressure strain, viscous diffusion and dissipation.

Cherukat *et al.* [34] DNS results were in agreement with Hudson *et al.* [26] for the mean velocity and turbulence intensities. They also observed similar physics as in previous studies, such as a considerable spatial variation of the Reynolds stresses in the inner region, $y/2h < 0.125$, and high levels of turbulence production within the separated shear layer. Yoon *et al.* [35] investigated the effects of changing the $\frac{\lambda}{a}$ value on the turbulent flow. They found that the recirculation size increased with the decrease of (λ/a), in agreement with previous studies [22–24].

The predictive performance of RANS models was assessed in [36, 41–43]. Patel *et al.* [36] used the standard k–ϵ turbulence model with a one-equation model or a standard wall function for the near-wall region. Their predicted mean velocity profiles demonstrate the poor performance of a standard wall function treatment. Knotek and Jicha [41] used the k–ω, SST, and $\overline{v'^2}$-f models. The three models predicted the separation location reasonably well, but the reattachment point was over-predicted by all models. The $\overline{v'^2}$-f model achieved the most accurate prediction when compared to the DNS results from Yoon *et al.* [35]. Khaled *et al.* [42] used a standard k–ϵ turbulence model with enhanced wall treatment and captured the separation and reattachment locations well.

Dellil *et al.* [39] used a k–ϵ turbulence model and the near the wall region is resolved with an one-equation model, and their results matched the experiments [33] well. They demonstrated the wavy amplitude effects on drag coefficient, pressure coefficient, and Nusselt number; these are important factors when designing a heat exchanger that would apply such wavy geometry. Their findings showed both a Nusselt number and pressure drop increase when the wave amplitude increases, corresponding to decreasing λ/a.

Predictions using Large Eddy Simulation (LES) were presented in [37, 38, 40]. Henn and Sykes [37] made detailed comparisons of mean velocity and turbulence intensities to the experimental data in [25]. They studied wave amplitudes that ranged from large λ/a (no flow separation) to small λ/a (with flow separation). They mention that the large-scale eddies generated by the separating shear layer allowed the LES to solve a larger region of the flow field. Henn and Sykes [37] provided evidence for large lateral velocity fluctuations in a region located on the upslope of the wave. Cui *et al.* [38] predicted an earlier separation and a later reattachment when compared to the experimental data [25]. They focused on the validation of new methods for treating the flow over a rough surface for an LES approach. Wagner *et al.* [40] considered the heat transfer, by applying a constant heat flux condition to the lower wall. They also observed the importance of the wall treatment because of deviation from the standard log-law velocity profile. Their conclusion reinforced the importance of integration up to the wall for the RANS models, as mentioned earlier in Patel *et al.* [36].

2.3 Objectives

The objective of the current experimental study is to further improve the physical understanding of the turbulent flow over an isothermal wavy geometry using single point statistical moments obtained using a Particle Image Velocimetry (PIV) technique, for both developing and periodic regions. The experiments provided insight into the flow physics and also as validation data for numerical simulations. Consequently, high-quality experimental data are relevant for the better understanding of turbulent flows physics and modeling.

For the numerical investigations, the scope is limited to Reynolds-averaged Navier-Stokes (RANS) turbulence models, specifically the two-equation and Second Moment Closure (SMC) models (SMC). The models are presented in detail in Section 2.1, and in the turbulence models descriptions for the specific models used here (Appendix B). It should be noted that industrial CFD simulations rely mainly on two-equation turbulence models; they

are widely used and well-known tools for engineering design. Having confidence in their predictive capabilities is crucial, so the research uses a variety of two-equation turbulence models for the current analysis and provides a systematic evaluation of their performance for future reference for engineers when selecting those models. The research used two CFD codes (ANSYS CFX and Fluent) because they are commonly used in many industries. The study also explores SMC models to understand their accuracy for this particular application because no previous studies have systematically evaluated these models for this particular problem.

In this work, both the experimental and numerical studies have, as the key characteristic of the wavy channel, $\lambda/a = 10$. A second characteristic is $(2h + a)/a$ which is equal to 11 for the experimental data, and 10.33 for the numerical study. The $(2h + a)/a$ value is slightly smaller for the numerical work because it was performed earlier to match experiments from Buckles *et al.* [25]. The Reynolds number was studied for the particular values of 5040, 8387, 10671, and 13039.

Chapter 3

Methodology

This chapter describes in detail the methodology used to perform the experimental and numerical studies. The experimental procedures are presented first, followed by the numerical procedures.

3.1 Experimental Procedure

This section presents the experimental procedures used for the velocity measurements in this research. It includes a description of the water channel facility, the test section, test flow conditions, the particle image velocimetry system, the measurement procedure, and measurements uncertainty. Convergence tests for the sample size and spatial resolution tests for the interrogation area sizes are in Appendix A.

3.1.1 Water channel facility and the PIV system

The experiments were conducted in a recirculating open water channel as shown in Figure 3.1. The recirculating open water channel has overall dimensions of 2500 (length) $\times$ 200 (width) $\times$ 200 (height) mm^3. The side walls of the channel were made of smooth transparent acrylic to facilitate optical access. The water is recirculated by a centrifugal pump, controlled by a variable speed drive motor. The motor's frequency was adjusted to obtain the desired flow velocities. The water channel has a flow conditioning unit placed prior to a six-to-one ratio contraction section. The flow conditioning unit is made of a series of steel plates and honey combs. The combination of the flow conditioning unit with the contraction section prior the flow entrance in the test section is able to break down the large scale turbulence, accelerate

the flow, and provide a uniform inlet flow. The water channel also contains piping, valves, supporting framework and a filtering system.

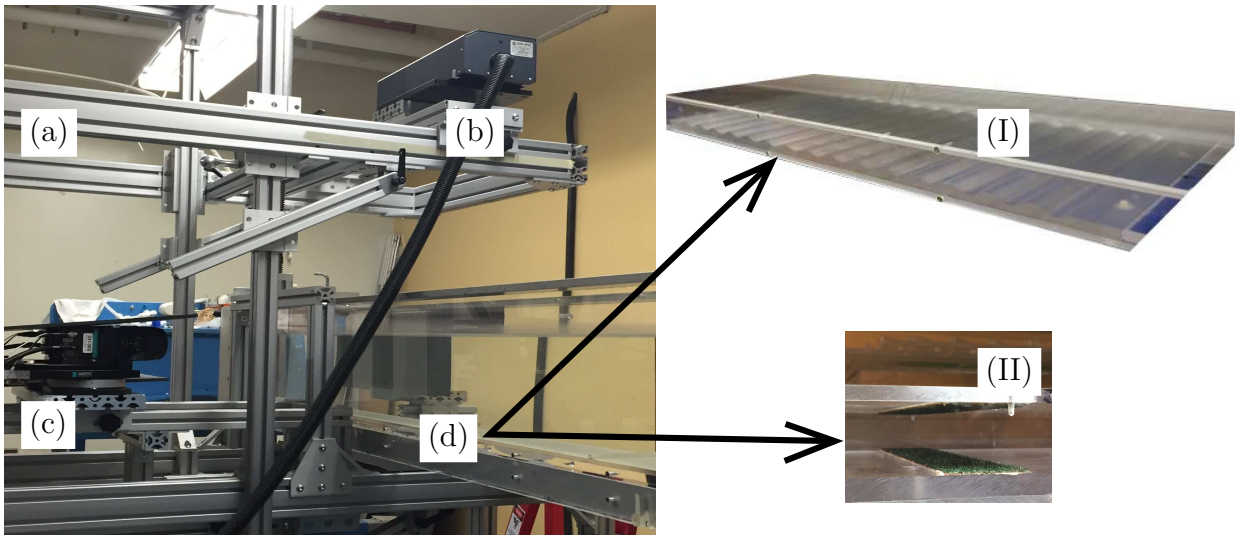

Figure 3.1: Experimental setup: (a) transverse system, (b) Nd:YAG double-pulsed laser, (c) CCD camera, (d) recirculation water channel, which contains both the wavy bottom wall test section (I) and the entrance sand paper sheets (II).

A channel test section (Figure 3.2) was placed into the recirculating water channel, from the inlet to the outlet of the main water channel. The test section channel is 2500 mm in length with an internal cross section 188 mm wide and 30 mm high (the y direction in Figure 3.2). The test section was made of 6 mm thick clear acrylic plates to facilitate optical

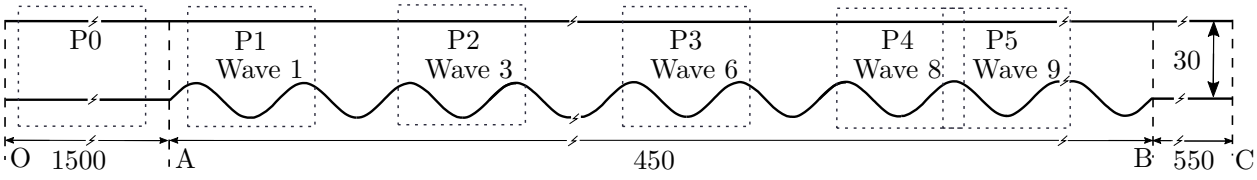

Figure 3.2: Schematic of the experimental test section. Dashed squares represent the x–y measurement planes and dimensions are in mm.

access. The aspect ratio, defined as width to channel height ($W/2h$), is 6.2. The bottom wavy section (A) starts 1500 mm from the water channel entrance (O), and is composed of 15 waves, where the mean wave level is at the same height as the upstream smooth surface lower wall. The sinusoidal wavy shape section (AB) was machined and 450 mm long, where the wave details are in Figure 2.1. The bottom wavy section is followed by a 550 mm downstream section (BC). The turbulent boundary layer development was accelerated before the wavy section by tripping the flow with a 12 grit-sandpaper sheet measuring 188 mm in width and 35 mm in length (in the flow direction) placed at the leading top and bottom edges of the test channel.

3.1.2 Test Conditions

The experimental flow conditions studied were for the bulk Reynolds number ($\mathrm{Re_b}$) of 5040, 8387, 10671, and 13039 with respective bulk velocity values of $U_b = 0.340$, 0.565, 0.719, and 0.788 m/s, and $h = 15$ mm. The fluid properties were taken as $\rho = 998$ kg/m^3, and $\mu = 0.00101$ kg/m·s at the temperature of 20° Celsius. Details of the approaching flow over the smooth wall prior the wavy wall are presented in Appendix C.

3.1.3 System Components

The flow measurements were performed using a two-component planar PIV system at streamwise/wall-normal planes located at the mid-span along the test section as illustrated in Figure 3.2. The PIV is a non-intrusive technique that measures the instantaneous velocity for an entire predetermined field of view [44]. The current PIV system is composed of the following components: fluorescent polymer seeding particles, a Nd:YAG double-pulsed laser, a CCD camera, and a data acquisition system, and are described in detail in the following sub-sections.

Fluorescent polymer seeding particles

Because the PIV system does not measure the fluid velocity but the particles within the fluid, it is necessary that those particles faithfully follow the fluid motion in order to ensure the correct velocity measurements. In the present study, fluorescent polymer seeding particles (Rhodamine B) of mean diameter of 10 μm, specific gravity of 1.19, and reflective index of 1.48 were homogeneously distributed throughout the flow to reflect the laser light to the camera, where the particles positions are recorded. To confirm that the particles indeed follow the fluid motion, it is necessary to calculate a few parameters involving the fluid and particles properties such as the settling velocity (v_s), which is estimated from Stokes drag law for flow around a sphere using Equation 3.1, and the response time (t_r) of the seeding particles, Equation 3.2, both found in Raffel *et al.* [44].

$$v_s = \frac{(\rho_p - \rho_f) g {d_p}^2}{18\mu_f} \tag{3.1}$$

$$t_r = \rho_p \frac{{d_p}^2}{18\mu_f} \tag{3.2}$$

In these equations ρ_p is the particle density, ρ_f is the fluid density, g is the acceleration due to gravity, d_p is the particle diameter, and μ_f is the dynamic viscosity of the fluid. Particles with negligible settling velocity and quick response time are desirable. The estimated values of settling velocity and response time were 1.02×10^{-6} m/s and 6.53×10^{-6} s, respectively. It is also noted that the settling velocity is negligible compared to the flow bulk velocities used in this study. A second observation that can be made is the negligible response time of the particles, when compared to the repetition rate between the two successive flow field images captured by the CCD camera of 268×10^{-6} s . It is therefore concluded that the particles followed the flow faithfully.

Nd:YAG double-pulsed laser

A New Wave Solo Nd:YAG (neodymium-yttrium-aluminum-garnet) double-pulsed laser illuminated the flow field from the top of the channel. Nd:YAG is considered one of the most important solid-state lasers used for PIV measurements because it provides a monochromatic light with high intensity illumination [44]. The particular laser used in the present study emits green light with a maximum energy of 120 mJ per pulse at a wavelength of 532 μm and a maximum repetition rate of 15 Hz. The laser also enables two illuminations with an adjustable separation time between them, referred to here as Δt. Another important consideration is that the laser passes through a set of lenses, that create a plane sheet of light at the mid-span of the water channel.

CCD camera

A camera is used to capture two successive flow field images. For this study a high-resolution 2048×2048 pixel 12-bit couple-charged device (CCD) camera with a 7.4 μm pixel pitch was used. The quality of the velocity vectors is improved by the use of an orange filter on the camera and the fluorescent particles. A synchronizer controlled the trigger rate of the laser and the CCD camera image capturing time. The field of view used in this study was of 50×50 mm. The images are divided into grids of small regions called interrogation areas (IAs).

Data acquisition system

A data acquisition system was used to record, process and store the captured images. The guidelines suggested by Prasad *et al.* [45] and Forliti *et al.* [46] were followed to minimize bias and precision errors. During the image acquisition, the maximum particle displacement was less than 8 pixels (i.e., 1/4 of the 32 × 32 interrogation area) which produced a dynamic

range of 80 with 0.1 sub-pixel accuracy for the IA size of 32×32 pixels. The particle image diameter was approximately 2 pixels. The commercial software Dynamic-Studio version 4.1 supplied by Dantec Dynamics was used for data acquisition and post processing the image pairs. The adaptive correlation algorithm was used within the software to determine the local displacement vector (Δs) of the particles between the first and second images captured by the camera for each interrogation area (IA). A velocity vector is calculated for each IA by dividing the particle displacement (Δs) for the time between two images (Δt). This process generates a vector map for the entire field of view. A transversing system was used to allow both camera and laser to be placed in the desired location along the closed water channel. An upstream plane (P0) in Figure 3.2 located 100 mm before the wavy section was analyzed to verify fully developed turbulent flow before the wavy section. The flow development and periodicity test was accomplished by measurements of the flow field for Waves 1 (P1), 3 (P2), 6 (P3), 8 (P4) and 9 (P5), as shown in Figure 3.2.

3.1.4 Convergence and Spatial Resolution Tests

For the present study, a convergence test was performed to determine the sample size required to evaluate the quantities studied here, and the results are presented in Appendix A. As shown, the streamwise mean velocity, wall normal mean velocity, Reynolds stresses and triple velocity correlations were compared for a variety of sample sizes. It was found that a sample size of 7500 was adequate for these flow statistics because the results converged for the sample sizes greater than 2000. Because the sample size of 2000 was also found to be sufficient to evaluate the characteristics of the flow, it was used for the flow periodicity and inlet conditions measurements.

Spatial resolution tests were performed to determine if the interrogation area size used was suitable. The results, which are presented in Appendix A, showed that the IA size of $\Delta x \times \Delta y = 32$ pixels $\times$ 32 pixels with 50% overlap was appropriate because of the good

agreement among the different IA sizes considering the experimental uncertainty.

3.1.5 Measurement Uncertainty

The uncertainty calculations are based on the signal analysis theory from Bendat and Piersol [47] and the following equations were used:

$$\epsilon_{\langle U \rangle} = \frac{Z_c u}{\sqrt{N} \mid U \mid} \tag{3.3}$$

$$\epsilon_{\sqrt{\langle u^2 \rangle}} = \frac{Z_c}{\sqrt{2N}} \tag{3.4}$$

$$\epsilon_{\langle uv \rangle} = \frac{Z_c}{\sqrt{N}} \tag{3.5}$$

where, Z_c is the confidence coefficient (equal to 1.96 for 95% confidence level), $\langle U \rangle$ is the streamwise mean velocity, $\sqrt{\langle u^2 \rangle}$ is the root-mean square of the streamwise fluctuating velocity and $\langle uv \rangle$ is the Reynolds shear stress.

The measurement uncertainty for a 2000 sample based on theory of the signal analysis from Bendat and Piersol [47] for the ensemble averages are estimated to be less than $\pm 3.0\%$ of the streamwise mean velocity and $\pm 4.4\%$ of the Reynolds shear stress at a 95% confidence level. For the 7500 sample case, the uncertainty for the ensemble averages is estimated to be less than $\pm 1.0\%$ of the streamwise mean velocity and $\pm 2.3\%$ of the Reynolds shear stress at a 95% confidence level.

3.2 Numerical Procedure

The numerical simulations were performed using the commercial CFD codes ANSYS CFX (release 17.2), and ANSYS Fluent (release 17.2) to model the experimental cases. This section provides an overview of the procedures adopted when numerically solving the problem in question, including the solution domain, governing equations, and numerical solution method. The computational mesh was constructed using ICEM CFD (release 16.2). Grid independence tests are also presented.

3.2.1 Solution domain

A three dimensional geometry was constructed using the domain shown in Figure 2.1 with a small z-direction distance. The computational mesh is structured, non-orthogonal, and body-fitted, allowing the mesh to conform to the domain geometry. A mesh was generated for a single typical module first using ICEM CFD (release 16.2), and then the full computational domain was obtained by merging the entrance section of length L_{in}, 1/4 of a typical wave module, 11 typical wave modules of length (λ), and an outlet section. The mesh spacing was uniform in the x-direction but non-uniform in the y-direction. The first mesh spacing adjacent to the wall was specified to obtain $y^+ \leq 1$ by using a geometric expansion in the y-direction. Three nodes were uniformly distributed in the z-direction. The x-y plan of the sample mesh for a typical wave module is shown in Figure 3.3.

3.2.2 Boundary Conditions

Water enters the domain at the channel inlet, with a specified velocity, $U(y)_{in}$, at the distance $L_{in} = 126h$ upstream of the wavy section. The specified velocity distribution $U(y)_{in}$ was obtained from a preliminary simulation of a smooth wall duct of length equal to $296h$, where a fully developed turbulent flow was obtained. At the channel outlet, an average static

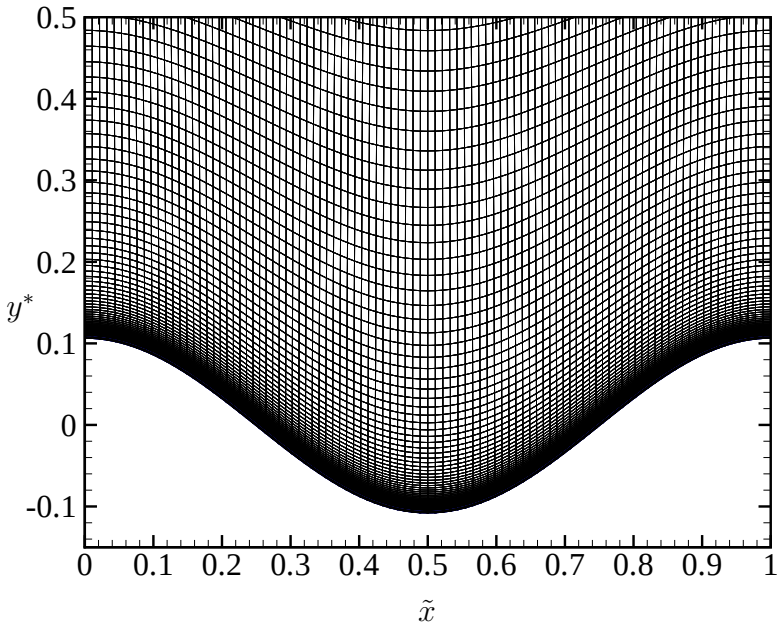

Figure 3.3: Mesh details for a typical wavy module using Grid 3.

pressure equal to zero reference pressure was prescribed. Symmetry conditions were applied in the two x-y planes so that the flow domain is considered two-dimensional. A smooth wall with no slip conditions was prescribed on the top and bottom walls.

The bulk Reynolds number ($\mathrm{Re_b}$) is 10700 for the numerical simulation with U_b = 0.458 m/s, and h = 23.7 mm. The fluid properties were taken as ρ = 998 kg/m^3, and μ = 0.00101 kg/m.s. The Reynolds number ($\mathrm{Re_b}$) is equivalent to an inlet Reynolds number, $\mathrm{Re_{in}}$, of 9753 with an averaged inlet velocity value of U_{in} = 0.409 m/s. The turbulence intensity was set to 5%, which is commonly defined as a medium turbulence intensity. The turbulent viscosity ratio, μ_τ/μ, is set to 10 at the inlet of the channel for the numerical simulations. These conditions are considered appropriate for the particular study case and additional details are presented in Appendix C.

3.2.3 Mathematical Model

The governing equations consist of transport equations for mass, momentum, and turbulence quantities. The flow is modeled as steady-state, isothermal, incompressible, and non-buoyant flow. Four two-equation eddy viscosity and three SMC models were used to predict the flow. A summary of the turbulence models, wall treatment and commercial code used is provided in Table 3.1. A transport equation for the turbulent kinetic energy, k, is solved by all four eddy viscosity models. The standard k–ϵ model solves the second equation for the turbulence eddy dissipation (ϵ). The Realizable k–ϵ model uses the turbulence eddy dissipation (ϵ) equation derived from the mean-square vorticity fluctuation. The k–ω model computes the second equation for the specific turbulence dissipation (ω). The SST model solves a blended transport equation of dissipation rate (ϵ) in the outer part of the boundary layer and specific turbulence dissipation (ω) within the near-wall region (boundary layer).

The three SMC models solve six partial differential transport equations for the Reynolds stresses instead of using the Boussinesq eddy viscosity assumption. The SMC models also solve a transport equation for the dissipation rate (ϵ) or the turbulence frequency (ω) in addition to the Reynolds stress equations. The LRR-IP model solves for the dissipation rate (ϵ). This model uses a linear correlation to model the pressure strain from the differential transport equations for the Reynolds stresses. The second ϵ–based model is the Linear Pressure-Strain (LPS). The SMC-ω solves the turbulence frequency (ω), and it has a different pressure-strain correlation. The Reynolds stress transport equations for this model are written in terms of ω instead of ϵ.

It is important to mention that the current study is a wall-bounded flow. In such cases, the wall has significant influence in the flow field, so it is noteworthy that the k-ϵ model in ANSYS CFX (release 16.2) offers only the scalable wall function (SWF) to model the near wall region. The SWF wall treatment may not be appropriate for cases of substantial recirculation regions. It is important to note that Fluent (release 16.2) offers a better variety

of near the wall modelling to take into effect the influence of the wall on the flow field, such as the enhanced wall treatment (EWT).

The near-wall treatments used for the turbulence models are now briefly described. They are described in detail in Appendix B (Section B.3). All ω-based turbulence models in CFX 16.2 and 17.2 (k–ω, SST, and SMC-ω) use an Automatic Wall Treatment (AWT) that uses an analytical expression for ω into the viscous sublayer. It is recommended that y^+ should be lower than one. The LRR-IP model uses a scalable wall function in CFX, which applies standard wall functions near the wall when the boundary layer is not fully resolved. The standard wall function uses the logarithmic law for the velocity variation near the wall. The Fluent 17.2 simulations use Enhanced Wall Treatment (EWT) for the ϵ-based models (k–ϵ, Realizable k–ϵ, and LPS). This method uses a two-layer model that subdivided the computational domain into two regions: a viscosity-affected region, where it solves the Wolfstein one-equation model, and a fully turbulent region, where the original turbulence model equations hold.

Table 3.1: Turbulence Models (RANS models) Summary.

Specific Model	Wall Treatment
Two-Equation	
Fluent (release 17.2) - Standard k-ϵ	EWT
Fluent (release 17.2) - Realizable k-ϵ	EWT
CFX (release 17.2) - Wilcox k-ω	AWF
CFX (release 17.2) - SST	AWF
SMC (ϵ-based)	
CFX (release 17.2)- LLR-IP	SWF
Fluent (release 17.2) - LPS	SWF/EWT
SMC (ω-based)	
CFX (release 17.2) - SMC-ω	AWT

3.2.4 Numerical solution method

ANSYS CFX discretization of the governing equations using a finite volume method with a finite element approach to representing the geometry. The mass conservation discretization uses a non-staggered grid with a Rhie-Chow type of pressure-velocity coupling. The Barth and Jesperson high-resolution advection scheme was used for the momentum equations and first order upwind for the turbulence quantities. ANSYS CFX computations of the coupled discretized equations are performed iteratively using additive correction multigrid acceleration, and the calculations use double precision. Solutions were considered converged when the root mean square of the normalized residual of each of the discretized equations was less than 1×10^{-6}. ANSYS Fluent uses a pressure-based coupled algorithm to solve the governing equations, and the spatial discretization uses a least squares cell-based method. Pressure and momentum equations use a second order upwind scheme and the turbulence quantities use a first order upwind scheme. Convergence was declared when the maximum value of continuity equation residuals was less than 1×10^{-5}, and the highest values of momentum and turbulence equation residuals were less than 1×10^{-7}. Additional details of the solution methods are given in [48].

3.2.5 Grid independence study

A variety of computational grids based on y^+ values, simulation results, and convergence behaviour was used to conduct preliminary studies. This study led to a baseline grid selection referred to here as Grid 3. A new set of grids was then generated to established a grid independence test. Table 3.2 summarizes grid properties for a typical wavy module, in descending order of the total number of nodes in the x–y plane, N_t. Grids 1 and 5 were based on Grid 3, except with a change in the number of nodes in the x direction, N_x. Grids 2 and 4 were based on Grid 3 except with a change in the number of nodes in the y-direction, N_y.

Table 3.2: Typical wavy module grids

Grid	y^+	N_x	N_y	N_t
1	0.14	118	150	17700
2	0.14	98	170	16600
3	0.14	98	150	14700
4	0.14	98	130	12740
5	0.14	78	150	11700

Differences in the streamwise mean velocity were quantified using a range-normalized root mean square parameter, $\mathrm{RMS}_{\mathrm{RN},\phi}$, defined in Equation (3.6).

$$\mathrm{RMS}_{\mathrm{RN},\phi} = 100 \times \sqrt{\frac{1}{N_{\mathrm{rms}}} \sum_{i=1}^{N_{\mathrm{rms}}} \left(\frac{\phi_{1,i} - \phi_{2,i}}{\max(\phi_1) - \min(\phi_1)} \right)^2} \tag{3.6}$$

where N_{rms} is the total number of samples taken along each location. The $\phi_{1,i}$ and $\phi_{2,i}$ are the values being compared, where $\phi_{2,i}$ contains interpolated values when the number of nodes is different than $\phi_{1,i}$ in the y-direction. Table 3.3 summarizes comparisons of overall pressure drop (ΔP) and the mean streamwise velocity ($\langle U \rangle^*$) for grids 2 to 5 compared to Grid 1, along the eighth wave using the k–ω turbulence model, with N_{rms} equal to 150. It is noted that the $\mathrm{RMS}_{\mathrm{RN},\langle U \rangle^*}$ values for Grids 4 and 5 are higher than those for Grids 2 and 3. The percentage difference of the pressure drop is below, 0.1% for all five meshes, revealing practically identical values for the pressure drop. Grid 3 was considered the most appropriate balance of mesh density and computational effort. For Grid 3, the entrance section had 150 nodes in the y-direction with the first node at $y^+ = 0.14$, and 1500 nodes along the x-direction. The number of nodes in the x-y plane was 225,000 for the entrance section, 14,700 for each typical module, and 6600 for the 1/4 module. The entire mesh arrangement had 1,179,900 nodes because of the three nodes in the spanwise direction.

Table 3.3: Grid independence study results

Grid	$\mathrm{RMS}_{\mathrm{RN},\langle U\rangle^*}$				ΔP (%)
	$\tilde{x} = 0.0$	$\tilde{x} = 0.3$	$\tilde{x} = 0.5$	$\tilde{x} = 0.7$	
2	0.097	0.066	0.056	0.074	0.037
3	0.035	0.063	0.056	0.091	0.032
4	0.125	0.139	0.142	0.171	-0.063
5	0.107	0.163	0.142	0.233	-0.020

Chapter 4

Experimental Results and Discussions - Wavy Wall

In this chapter, the wavy wall effects on the turbulent flow characteristics are experimentally investigated, for the given wavy channel geometry and Reynolds numbers. The region studied encompasses the developing region (which extends from Wave 1 to Wave 8), and the fully periodic region after Wave 8. This chapter presents the recirculation size, mean velocity, Reynolds stresses, and turbulent kinetic energy production. Comparisons of the different turbulence statistics over the different waves are used to provide insights into the flow development. The Reynolds numbers effects are also studied for the flow in the fully periodic region.

4.1 Recirculation Region Characterization

The literature review in Sections 2.2.2 and 2.2.3 revealed that, for this bulk Reynolds number range (Re_b = 3000 to 13000), the separation and reattachment of the flow should be evident in the averaged statistical quantities. The mean flow visualization reveals this notable feature within the entire flow field. In this section, three techniques are used to estimate the size of the recirculation region: mean dividing streamlines, 50% forward flow fraction, and zero mean streamwise velocity. The forward flow fraction identifies the percentage of forward flow within the flow field, where the 50% occurrence identifies the separated region. The three techniques are commonly employed to identify the separated flow in a variety of geometries. The flow development and Reynolds number effects are both studied with the three techniques. The streamlines plots are the only technique used to estimate the centers of the recirculating region. However, all three techniques were used to estimate the separation and reattachment

locations for completeness and accuracy.

The contour plots for the mean dividing streamlines, 50% forward flow fraction, and zero mean streamwise velocity are shown in Appendix D. The recirculation locations (separation ($\tilde{x}_s$), center ($\tilde{x}_c$), and reattachment ($\tilde{x}_r$)) are summarized for all three techniques over Waves 1, 3, 6, 8, and 9 in Table 4.1. The recirculation center locations, $\tilde{x}_c$, were only estimated with the mean streamlines plots, and demonstrated great similarity between all waves, except Wave 1.

The $\tilde{x}_c$ result at Wave 1, reveals a much larger recirculation region, where the $\tilde{x}_c$ value is at about 0.55, compared to $\tilde{x}_c$ values of about $\tilde{x}_c$=0.47 for Wave 3, 6, 8, and 9. At Wave 6, this value is 0.48. However, this technique is based on visual observations, and has an estimated margin of error of $\pm$ 0.01. It is shown that the $\tilde{x}_c$ value remained unchanged after Wave 3. The separation and reattachment locations, $\tilde{x}_s$ and $\tilde{x}_r$, based on the streamline technique are very similar for Waves 3, 6, 8, and 9; the differences are close to or within the uncertainty of determining the locations, except at Wave 1 where the recirculation region extends in a larger portion of the Wave 1 wall.

The 50% forward fraction technique also reveals significant differences in the recirculation locations for Wave 1. The separation and reattachment locations in Table 4.1 show almost identical values for all waves, except Wave 1. The zero mean velocity technique also reveals the same features described in the other two techniques presented, as seen in Table 4.1.

The individual techniques' results were discussed and average results are also presented for each quantity in Table 4.1. This average is based on the three techniques presented, and the $\pm$ values represent the uncertainty in the mean based on the three techniques measurements. The uncertainty of the experimental values of $\tilde{x}_s$ is $\pm$ 0.01 at Wave 1, and less than 0.01 at the other waves. The $\tilde{x}_s$ values for all three methods are within measurement uncertainty. For $\tilde{x}_r$ the uncertainty is $\pm$ 0.02 at Wave 1 and 8, and it is less than 0.01 for the other waves. An analysis of the average values indicates the features that were evident

in the three techniques: a larger recirculation bubble at Wave 1 and nearly identical at Wave 3, 6, 8, and 9. It is observed that the streamline method tends to provide $\tilde{x}_r$ values that are relatively larger compared to values from the other 2 techniques. Nonetheless, the observation that $\tilde{x}_r$ is similar for Wave 3, 6, 8 and 9 is still valid.

Table 4.1: Recirculation locations (separation ($\tilde{x}_s$), reattachment ($\tilde{x}_r$), and center ($\tilde{x}_c$)) for Waves 1, 3, 6, 8, and 9 and $\mathrm{Re_b} = 10700$.

	Technique			
	Dividing Streamline	50% Forward Fraction	Zero Mean Velocity	Average
$\tilde{x}_s$	0.12	0.10	0.11	0.11 ± 0.01
Wave 01 $\tilde{x}_r$	0.85	0.78	0.78	0.80 ± 0.02
$\tilde{x}_c$	0.55	-	-	-
$\tilde{x}_s$	0.13	0.14	0.13	0.14 ± 0.01
Wave 03 $\tilde{x}_r$	0.74	0.71	0.71	0.72 ± 0.01
$\tilde{x}_c$	0.47	-	-	-
$\tilde{x}_s$	0.15	0.14	0.14	0.14 ± 0.01
Wave 06 $\tilde{x}_r$	0.76	0.71	0.71	0.73 ± 0.01
$\tilde{x}_c$	0.48	-	-	-
$\tilde{x}_s$	0.13	0.13	0.14	0.13 ± 0.01
Wave 08 $\tilde{x}_r$	0.76	0.71	0.70	0.72 ± 0.02
$\tilde{x}_c$	0.47	-	-	-
$\tilde{x}_s$	0.12	0.13	0.13	0.13 ± 0.01
Wave 09 $\tilde{x}_r$	0.75	0.71	0.71	0.72 ±0.01
$\tilde{x}_c$	0.47	-	-	-

The Reynolds number effects were studied at Wave 9, and the results are summarized in Table 4.2 for $\mathrm{Re_b} = 5040, 8400, 10700$, and 13040.

Table 4.2: Recirculation locations (separation ($\tilde{x}_s$), reattachment ($\tilde{x}_r$), and center ($\tilde{x}_c$)) for Wave 9 and $\mathrm{Re_b} = 5040, 8400, 10700$, and 13040

Reynolds Number		Dividing Streamline	50% Forward Fraction	Zero Mean Velocity	Average
5040	$\tilde{x}_s$	0.12	0.12	0.11	0.12 ± 0.01
	$\tilde{x}_r$	0.75	0.74	0.73	0.74 ± 0.01
	$\tilde{x}_c$	0.49	-	-	-
8400	$\tilde{x}_s$	0.12	0.12	0.12	0.12 ± 0.01
	$\tilde{x}_r$	0.75	0.72	0.72	0.73 ± 0.01
	$\tilde{x}_c$	0.48	-	-	-
10700	$\tilde{x}_s$	0.12	0.13	0.13	0.13 ± 0.01
	$\tilde{x}_r$	0.75	0.71	0.71	0.72 ± 0.01
	$\tilde{x}_c$	0.47	-	-	-
13040	$\tilde{x}_s$	0.12	0.12	0.13	0.12 ± 0.01
	$\tilde{x}_r$	0.74	0.70	0.70	0.71 ± 0.01
	$\tilde{x}_c$	0.48	-	-	-

The results reveal that, for this range of Reynolds number, the recirculation size decreases slightly as the Reynolds number increases. It can be seen that the average values among the three techniques presented in Table 4.2, showed this slight decrease. The values, however, are very similar when considering the uncertainty. It can be concluded that the reattachment location reduces as the Reynolds number increases but only slightly (5% reduction).

Kuzan *et al.* [24] showed this slight decrease in the recirculation region size when the Reynolds number varied from 4000 to 12000 for this same geometry. The Reynolds number range of this study was limited to 13040, but other studies showed that at higher Reynolds numbers the time-averaged results do not present a recirculation region. For example in Hamed *et al.* [31] ($\mathrm{Re_b} = 40000$) and Kuzan *et al.* [24] ($\mathrm{Re_b} = 48000$). It should be noted

that at those high Reynolds numbers instantaneous reverse flow is still observed [24]. The results presented for the separation and reattachment locations are in good agreement with previous findings summarized in Table 2.1. For example, Buckles *et al.* [25] found a separation location ($\tilde{x}_s$) at 0.14 and reattachment location ($\tilde{x}_r$) at 0.69, using streamlines plots, showing very similar results to the current experiment of 0.13 $\pm$ 0.01 and 0.72 $\pm$ 0.01 at Wave 9.

4.2 Mean Velocity

The streamwise and wall-normal mean velocities are examined in this section by the use of contours, one-dimensional profiles, and quantitative analyses. The contours plots for the streamwise and wall-normal dimensionless mean velocities, $\langle U \rangle^*$ and $\langle V \rangle^*$, are shown in Figure 4.1 at Wave 1, 3, and 9.

The key features observed in this flow are the recirculation region and the shear layer formation, as earlier noted in the literature (e.g., in Buckles *et al.* [25]). These key features represent significant differences in the flow field when compared to canonical turbulent flows (e.g., flat wall channel). Important differences are: significant back flow, streamline curvature, and significant non-zero wall-normal velocity. Note that these non-zero wall-normal mean velocities and their non-negligible spatial gradient play a significant role in moment and turbulent transport that is not possible in the flat wall channel flow. Buckles *et al.* [25] velocity measurements revealed an inner boundary layer formation downstream from the reattachment location and this thin inner boundary layer moves away from the wall at the separation point and forms a free shear layer. This shear layer is the region just above the recirculation bubble in Figure 4.1 (a c, and e).

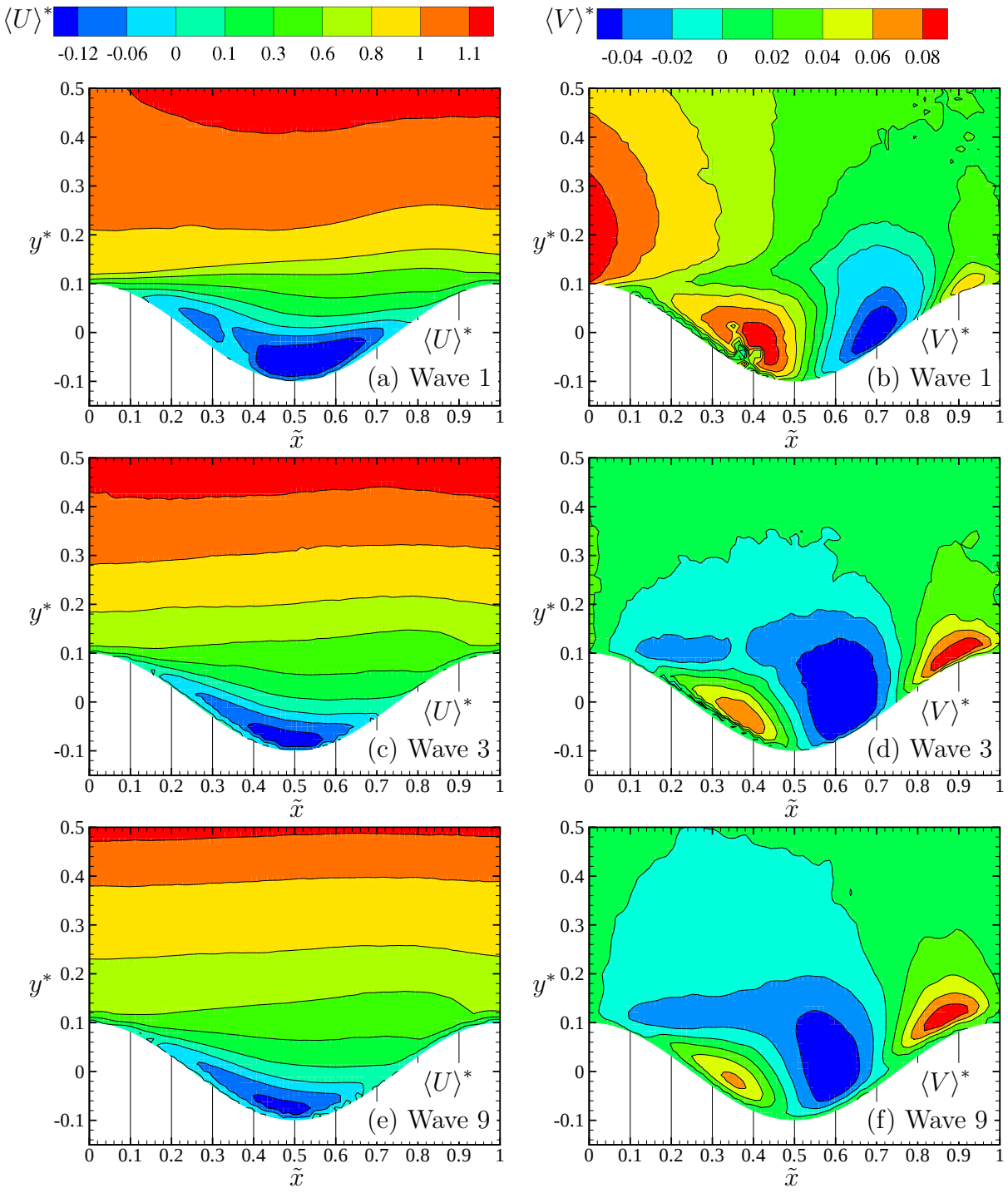

Figure 4.1: Contour plots of dimensionless streamwise mean velocity, $\langle U \rangle^*$, at Wave 1 (a), Wave 3 (c), and Wave 9 (e), and dimensionless wall normal mean velocity, $\langle V \rangle^*$, at Wave 1 (b), Wave 3 (d), and Wave 9 (f) for $\mathrm{Re_b} = 10700$.

When comparing the flow over the different Waves, Figure 4.1 shows that there are considerable differences in the recirculation region extent and height between Wave 1 and 9, whereas the recirculating zone at Waves 3 and 9 are similar. The recirculation region at Wave 1 (Figure 4.1 (a)) is relatively larger when compared to Wave 3 (Figure 4.1 (c)) and 9 (Figure 4.1 (e)). The recirculation region was extensively discussed in the previous section; therefore, this section will focus on the velocity distributions and the shear layer formed.

The velocity distributions in each direction, streamwise and wall-normal, have different patterns, but they are both influenced by the presence of the recirculation region. A clear flow inhomogeneity in the x and y directions is observed for all waves. The streamwise mean velocity is positive for most of the channel height and $\langle U \rangle^*$ reduces to zero or negative values when approaching the wavy walls because of the recirculation region. Reverse flow (negative $\langle U \rangle^*$) occurs in the inner region of the wave, beneath the zero mean velocity contour. The highest streamwise velocity contour location shifts upwards in the y direction for Wave 9 compared to Waves 1 and 3, Figure 4.1. Figure 4.1 (b, d, and f) for the wall normal mean velocity show high positive values between $\tilde{x} = 0.2$ and 0.4, where the flow streamlines show a flow moving upward and backward. Downstream of $\tilde{x}$ =0.7, flow moves upward and accelerates over the crest (between $\tilde{x} = 0.8$ and 0.95). The $\langle V \rangle^*$ value is as high as 0.08 at Waves 3 and 9, and as high as 0.04 at Wave 1. These high values between $\tilde{x} = 0.8$ and 0.95 are the consequence of straightening of the channel when compared to the greater channel height seen at $\tilde{x}$ of 0.5. The wavy geometry contraction after $\tilde{x} = 0.5$ is creating a favorable pressure gradient, which is causing the flow to reattach after $\tilde{x} = 0.7$.

The profiles of the streamwise mean velocity are shown in Figure 4.2 at Waves 1, 3, 6, 8, and 9. They show the previously observed behavior where the maximum $\langle U \rangle^*$ value is shifting upwards from Wave 1 to Wave 6. This behavior is not found in Wave 8 and 9, which also indicates a periodic flow after Wave 8. The maximum local streamwise mean velocity is located further away from the wall when compared to a channel turbulent flow despite the wave location. Another common feature is the streamwise mean velocity profiles inflection

point (i.e., a curve concavity change) at about $y^* = 0.1$ for all Waves where a reverse flow exists.

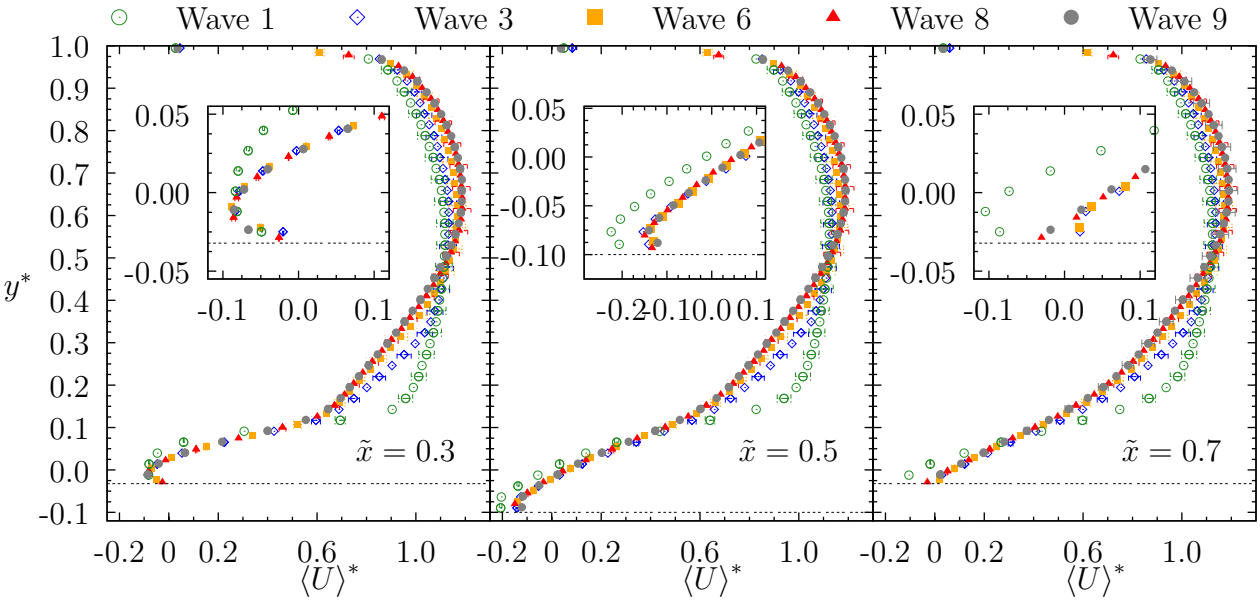

Figure 4.2: Profiles of dimensionless streamwise mean velocity, $\langle U \rangle^*$, at Wave 1, 3, 6, 8, and 9, at $\tilde{x} = 0.3$, 0.5, and 0.7, for $\mathrm{Re_b} = 10700$.

The maximum reverse flow at $\tilde{x} = 0.50$ for Waves 1 is of -0.22, which is higher than the maximum reverse flow of -0.14 at Wave 9. The reverse flows for Waves 3, 6, and 8 are the same as Wave 9 considering the measurements uncertainty. Figure 4.2 also shows the relatively larger recirculation region at Wave 1 because the Wave 1 profiles have near-wall negative values at $\tilde{x}$ =0.7, whereas all other waves have values close to zero.

The experimental uncertainties bars are plotted along with the profiles in Figure 4.2, at every fourth data point. These bars enable the assessment of the flow development realistically. At the region below $y^* = 0.1$ the bars are not visible due to its very small magnitude due to the small velocity measurements. The profiles for Wave 8, clearly demonstrated that, considering the uncertainty, both Waves 6 and 9, have nearly identical streamwise mean velocity profiles at the three location presented. At Wave 1, the profiles are significantly

different from those at Waves 6, 8, and 9 for nearly the entire channel, except for the very near wall regions at $\tilde{x} = 0.3$, where the flow velocity is approaching zero. Waves 3 and 1 have similar profiles in the outer region (above $y^* = 0.35$), when considering the uncertainty. Only Wave 1 has distinct profiles at the region between the wavy wall and $y^* = 0.05$ when compared to the other waves, at $\tilde{x} = 0.3$, 0.5, and 0.7. A quantitative study gave $\mathrm{RMS}_{\mathrm{RN},U^*}$ values when comparing the experimental data profiles at $\tilde{x} = 0.50$ for Waves 1, 3, 6, 8 to those for Wave 9, of 12.89%, 9.49%, 4.20%, and 3.00%, respectively. These results also illustrate the flow development and the close similarity between the flow at Waves 6, 8 and 9.

Figure 4.3 shows wall-normal mean velocity profiles extracted at $\tilde{x} = 0.3$, 0.5, and 0.7 to further compare the flow field among the different waves. The most evident features of Figure 4.3 is the difference between Wave 1 profiles and those of the other waves.

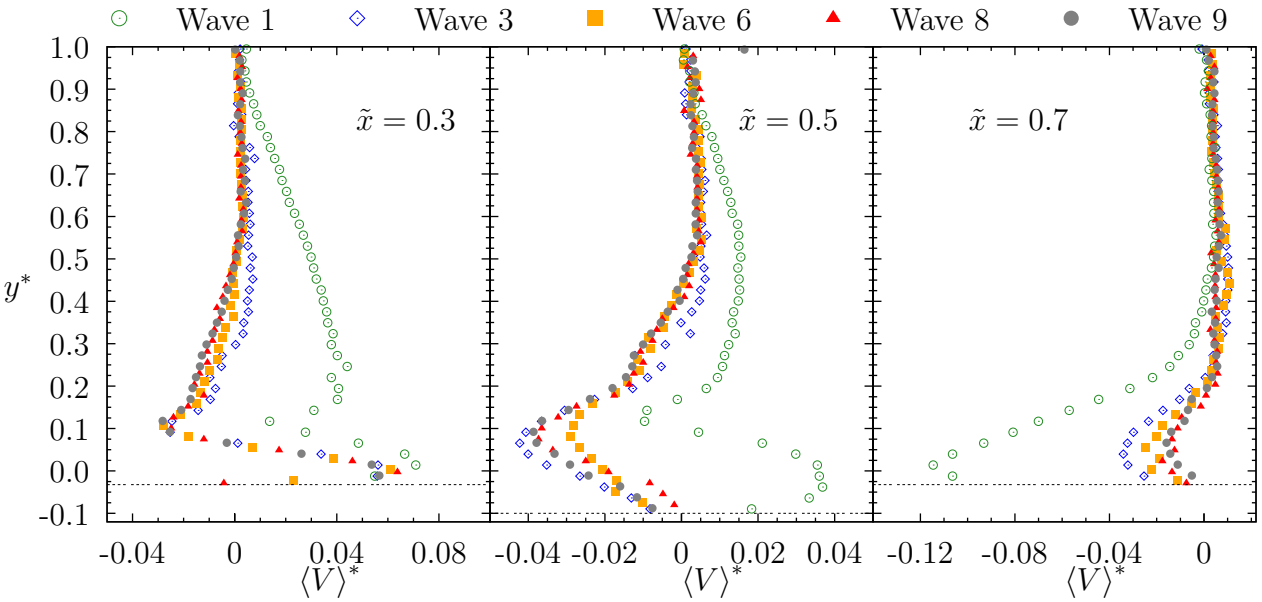

Figure 4.3: Profiles of dimensionless wall-normal mean velocity, $\langle V \rangle^*$, at Wave 1, 3, 6, 8, and 9, at $\tilde{x} = 0.3$, 0.5, and 0.7, for $\mathrm{Re_b} = 10700$.

Because the upstream flow has just reached the wavy wall at Wave 1, those differences are

expected. For example, the greater $\langle V \rangle^*$ magnitude along nearly the entire channel height at $\tilde{x} = 0.3$ compared to the other Waves. This is explained with the aid of the contour in Figure 4.1 (b) where high wall-normal mean velocity are observed in two regions; first, the region between $y^* = 0.1$ and 0.5 due to the recent flow acceleration due to the channel contraction when the flow reached the first wave; and second, at the inner region of the wave due to the higher recirculation region at Wave 1, as mentioned earlier. The $\langle V \rangle^*$ profiles at Wave 8 and 9 are nearly identical and fairly similar to Wave 6. Wave 3 results are not as quite similar to Wave 9, but they are closer to Wave 6 than to Wave 1. The wall-normal mean velocity is negative where the flow is moving downwards to the reattachment location, consistent with the recirculation region. The negative $\langle V \rangle^*$ values also imply a transport of high momentum from the core region of channel towards the wavy wall. The $\langle V \rangle^*$ profiles at $\tilde{x} = 0.7$ in Figure 4.3 show values as low as -0.12 at Wave 1 whereas for the other Waves values of less than -0.04. Indicating a higher momentum transport between the core region and the inner region at Wave 1.

The Reynolds number effects are studied in Figure 4.4, where profiles of the dimensionless mean streamwise velocity and wall-normal mean velocity are plotted at $\tilde{x} = 0.5$, for Wave 9. The results are plotted for $\mathrm{Re_b}$ of 5040, 8400, 10700, and 13040 from the present study and from Buckles *et al.* [25] at $\mathrm{Re_b} = 12000$. Buckles *et al.* [25] velocity profiles for $\mathrm{Re_b} = 12000$ are also plotted for comparison here, and they agreed well at Wave 9 with the current experiments as shown in Figure 4.4. Both the streamwise and wall-normal mean velocity profiles demonstrated that the changes in Reynolds number do not have significant effect on the flow field. The maximum reverse flow at $\tilde{x} = 0.5$ was relatively the same for all Reynolds numbers. At $\mathrm{Re_b} = 13040$, slightly higher negative wall-normal mean velocity value (-0.045) is observed compared to a value of -0.040 at $\mathrm{Re_b} = 5040$. It is concluded that the first order statistics are not significantly different over the range of Reynolds number presented here.

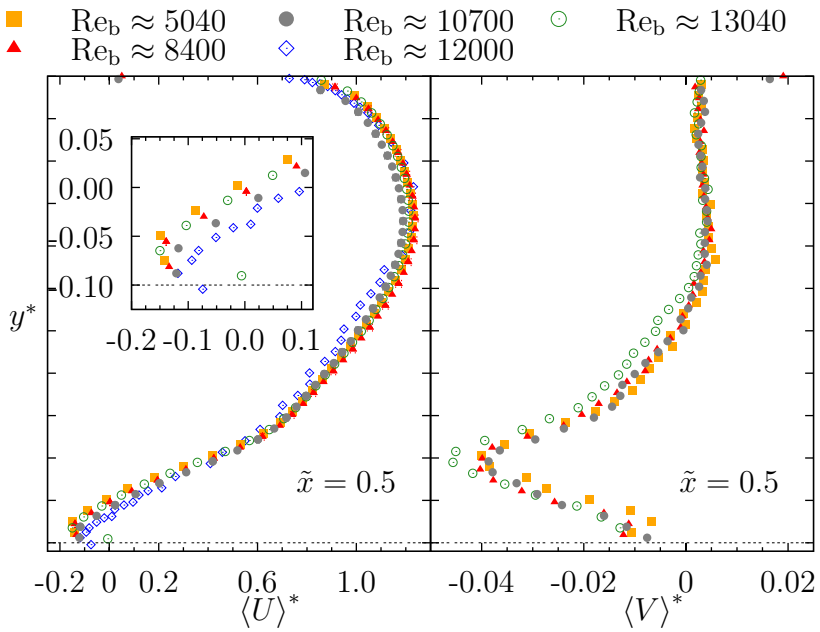

Figure 4.4: Profiles of dimensionless streamwise mean velocity, $\langle U \rangle^*$, and wall-normal mean velocity, $\langle V \rangle^*$, at Wave 9 and $\tilde{x} = 0.5$, for $\mathrm{Re_b} = 5040, 8400, 10700, 12000$ [25], and 13040.

4.3 Reynolds stresses

4.3.1 Reynolds normal stresses

Contour plots of dimensionless streamwise and wall-normal Reynolds stresses, $\langle u^2 \rangle^*$ and $\langle v^2 \rangle^*$, are presented in Figure 4.5 at Waves 1, 3 and 9 for $\mathrm{Re_b} = 10700$. Streamlines are superimposed in Figure 4.5 (e) for reference. The main feature observed is the significantly higher levels of the Reynolds stresses just above the recirculation region than any other area of the channel for all the waves studied. The wave shape induces small variations in the outer area of the flow, which will also be seen in Figures 4.6 and 4.7. Kruse *et al.* [1] had previously shown that the outer flow characteristics are independent of turbulence generated at the wall.

The highest $\langle u^2 \rangle^*$ values occur at $y^* = 0.1$, and between $\tilde{x} = 0.1$ and 0.7. The highest $\langle v^2 \rangle^*$ values occur at about $y^* = 0.1$, and between $\tilde{x} = 0.2$ and 0.7.

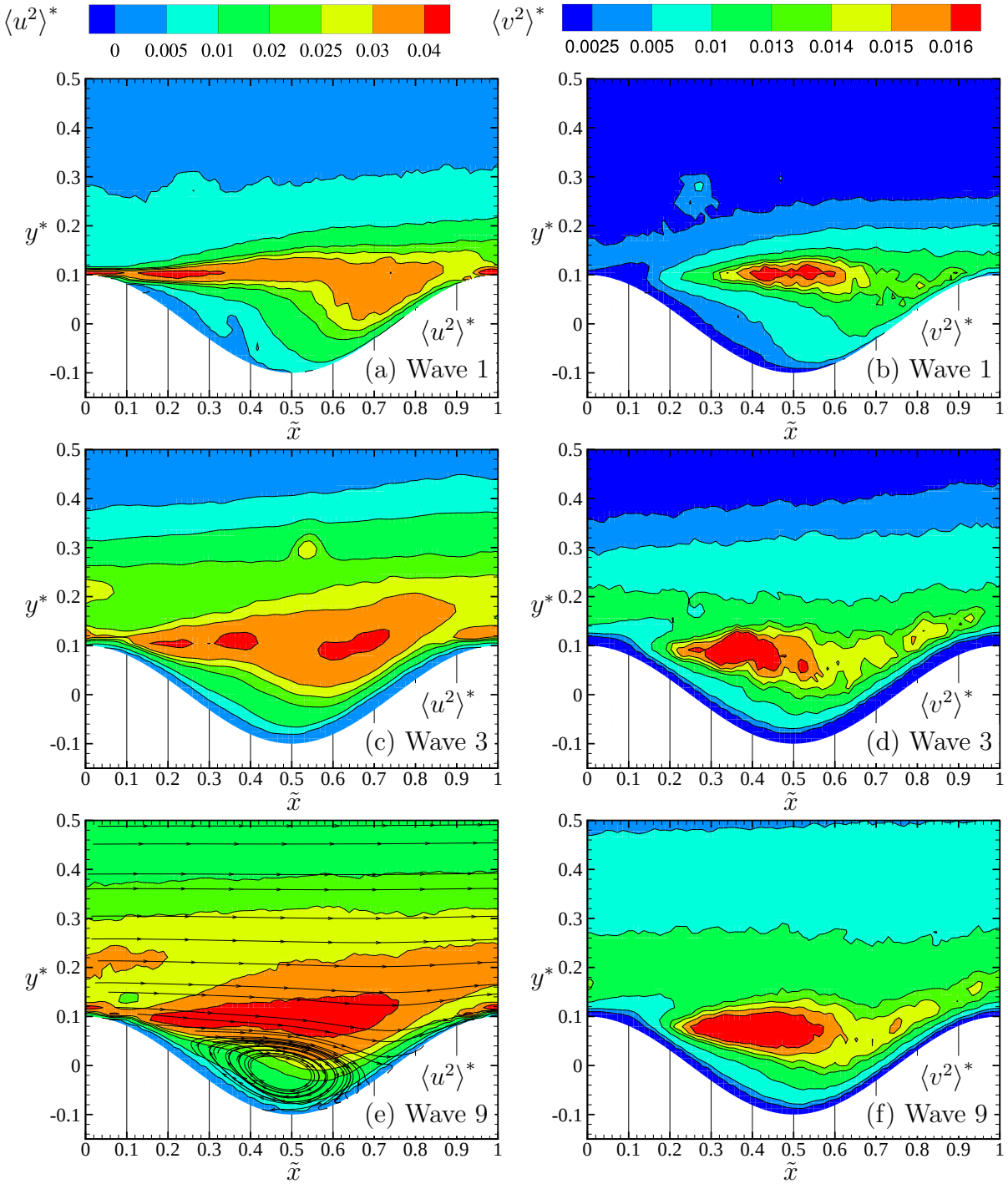

Figure 4.5: Contour plots of dimensionless Reynolds normal stresses in the streamwise direction, $\langle u^2\rangle^*$, (a, c, e) and in the wall-normal direction, $\langle v^2\rangle^*$, (b, d, f) at Wave 1, 3, and 9 at $\mathrm{Re_b} = 10700$.

This elevated level of the Reynolds stresses is typically attributed to the presence of energetic large scales structures associated with a separated shear layer [1, 26, 34]. At Wave 9, the peak values of streamwise Reynolds stresses are 0.042 which is about 2.5 times bigger than the peak of wall-normal Reynolds stresses, 0.017. This is similar for the other waves. One important implication of this observation is that, in principle, turbulence models that assume isotropic turbulence will not be able to reproduce the flow characteristics accurately.

A feature of the flow development can be observed in the contours plots (Fig. 4.5); the continued increase of both streamwise and wall-normal Reynolds stresses influence in the outer region of the flow. For example, the $\langle u^2 \rangle^*$ contour level of 0.005 is at $y^* = 0.3$ at Wave 1, at $y^* = 0.4$ at Wave 3, and above $y^* = 0.5$ at Wave 9. The $\langle v^2 \rangle^*$ contour level of 0.005 also shows the same trends; it is at $y^* = 0.2$ at Wave 1, at about $y^* = 0.3$ at Wave 3, and at $y^* = 0.5$ at Wave 9.

Those quantities are further investigated, including the Wave 6 and 8 results, with one-dimensional profiles at $\tilde{x} = 0.3$, 0.5, and 0.7 in Figure 4.6 and 4.7. The peaks of maximum $\langle u^2 \rangle^*$ and $\langle v^2 \rangle^*$ in the one-dimensional profiles provide a more detailed assessment of the Reynolds stresses. The profiles in Figures 4.6 and 4.7 show steep increase in $\langle u^2 \rangle^*$ and $\langle v^2 \rangle^*$ from Wave 1 to Wave 6 between $y^* = 0.2$ and $y^* = 0.6$ and smaller increases from Wave 3 to Wave 8. This trend ceases between Wave 8 and 9. Examination of the results showed that the levels of Reynolds stresses for Wave 1, 3, 6, 8, and 9 remained nearly identical for $y^* \geq 0.7$. The $\langle u^2 \rangle^*$ and $\langle v^2 \rangle^*$ magnitude and shape changes from Wave 1 to Wave 9 are seen in the region below $y^* = 0.7$. This particular region shows the flow evolution from Wave 1 to Wave 9 in Figure 4.6.

At Wave 1, the overall $\langle u^2 \rangle^*$ profiles are significant lower when compared to Waves 3, 6, 8, and 9. The values of $\langle u^2 \rangle^*$ at Waves 8 and 9 are nearly identical considering the measurement uncertainty. Results at Wave 6 are similar to those at Waves 8 and 9, except slightly lower. The $\langle u^2 \rangle^*$ results at Waves 1 and 3 have significant lower values when compared to Waves 6,

8, and 9. It should be noted that all locations and waves have peak values of $\langle u^2 \rangle^*$ at $y^* = 0.1$. For example for Wave 9 the $\langle u^2 \rangle^*$ peak values are about 0.046, 0.042, and 0.042 (uncertainty of $\pm$ 0.001), at $\tilde{x} = 0.3$, 0.5 and 0.7, respectively. At Wave 1, the $\langle u^2 \rangle^*$ peak values are about 0.042, 0.035, and 0.035 (uncertainty of $\pm$ 0.002), at $\tilde{x} = 0.3$, 0.5 and 0.7, respectively. The higher Reynolds normal stresses are located in a region above the recirculation region and consistently positioned above the dividing streamline.

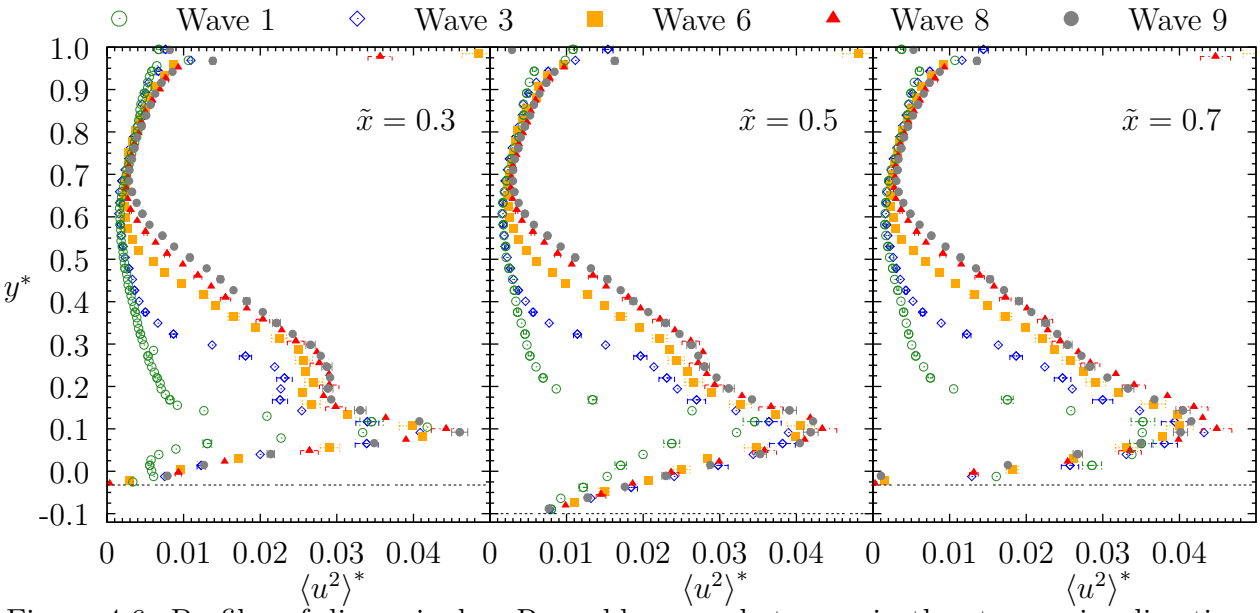

Figure 4.6: Profiles of dimensionless Reynolds normal stresses in the streamwise direction, $\langle u^2 \rangle^*$, at Wave 1, 3, 6, 8, and 9 at $\tilde{x}$ = 0.3, 0.5, and 0.7, for $\mathrm{Re_b} = 10700$.

The peaks in $\langle v^2 \rangle^*$ are also at $y^* = 0.1$ for all locations and waves presented. At Wave 9 the $\langle v^2 \rangle^*$ peak values are about 0.018, 0.017, and 0.015, at $\tilde{x} = 0.3$, 0.5 and 0.7, respectively. At Wave 1, the $\langle v^2 \rangle^*$ peak values are about 0.014, 0.016, and 0.014, at $\tilde{x} = 0.3$, 0.5 and 0.7, respectively. The maximum wall-normal Reynolds normal stress have increased from Wave 1 to Wave 9 at all locations presented. The peaks and the overall values of the Reynolds normal stresses are lower in the wall normal direction when compared to the streamwise direction. The $\langle u^2 \rangle^*$ and $\langle v^2 \rangle^*$ peaks also reveal a systematic decrease in value along the

wave length, particularly from $\tilde{x} = 0.3$ to 0.7.

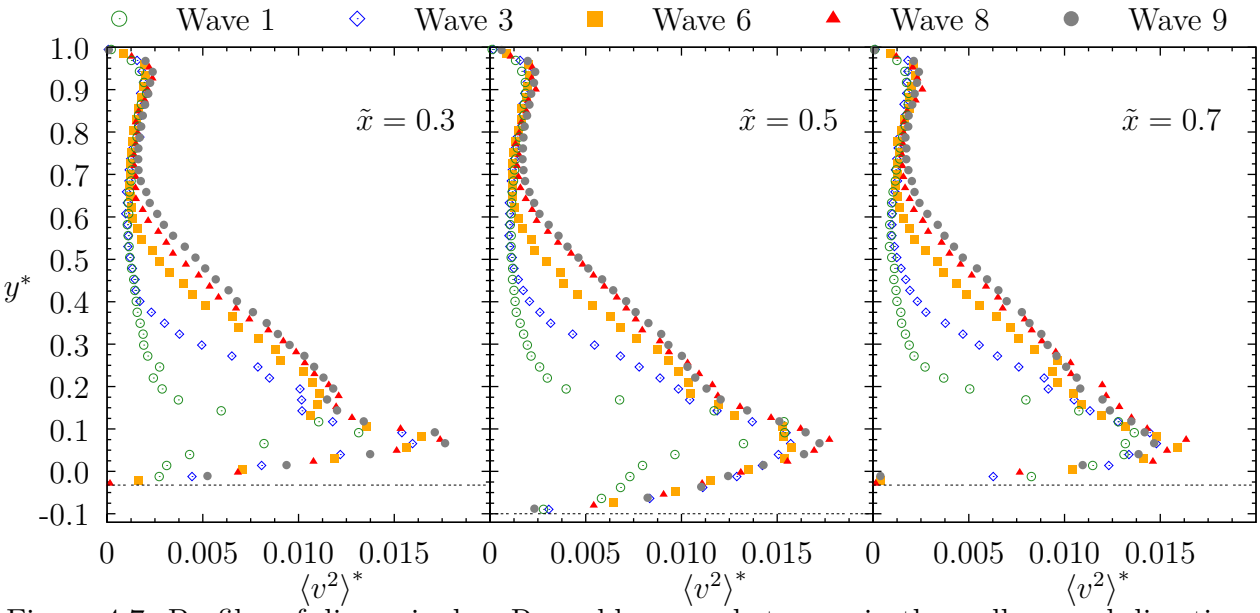

Figure 4.7: Profiles of dimensionless Reynolds normal stresses in the wall-normal direction, $\langle v^2 \rangle^*$, at Wave 1, 3, 6, 8, and 9 at $\tilde{x}$ = 0.3, 0.5, and 0.7, for $\mathrm{Re_b} = 10700$.

4.3.2 Reynolds Shear Stress and the Structural Parameter

Contours of the dimensionless Reynolds shear stress, $-\langle uv \rangle^*$, are presented in Figure 4.8 at Waves 1, 3, and 9 for $\mathrm{Re_b} = 10700$. As previously observed for the normal Reynolds stresses, a continual increase in $-\langle uv \rangle^*$ in the outer region of the flow is observed during the flow development over the different waves. The 0.005 contour level in Figure 4.8 is at $y^* = 0.15$ at Wave 1, at $y^* = 0.25$ at Wave 3, and $y^* = 0.4$ at Wave 9, reinforcing the increasing influence in the outer flow.

At Wave 1, the region of greatest Reynolds shear stress is within the thin shear layer above the recirculation zone. There is also a pocket of negative Reynolds shear stress at the entrance to Wave 1.

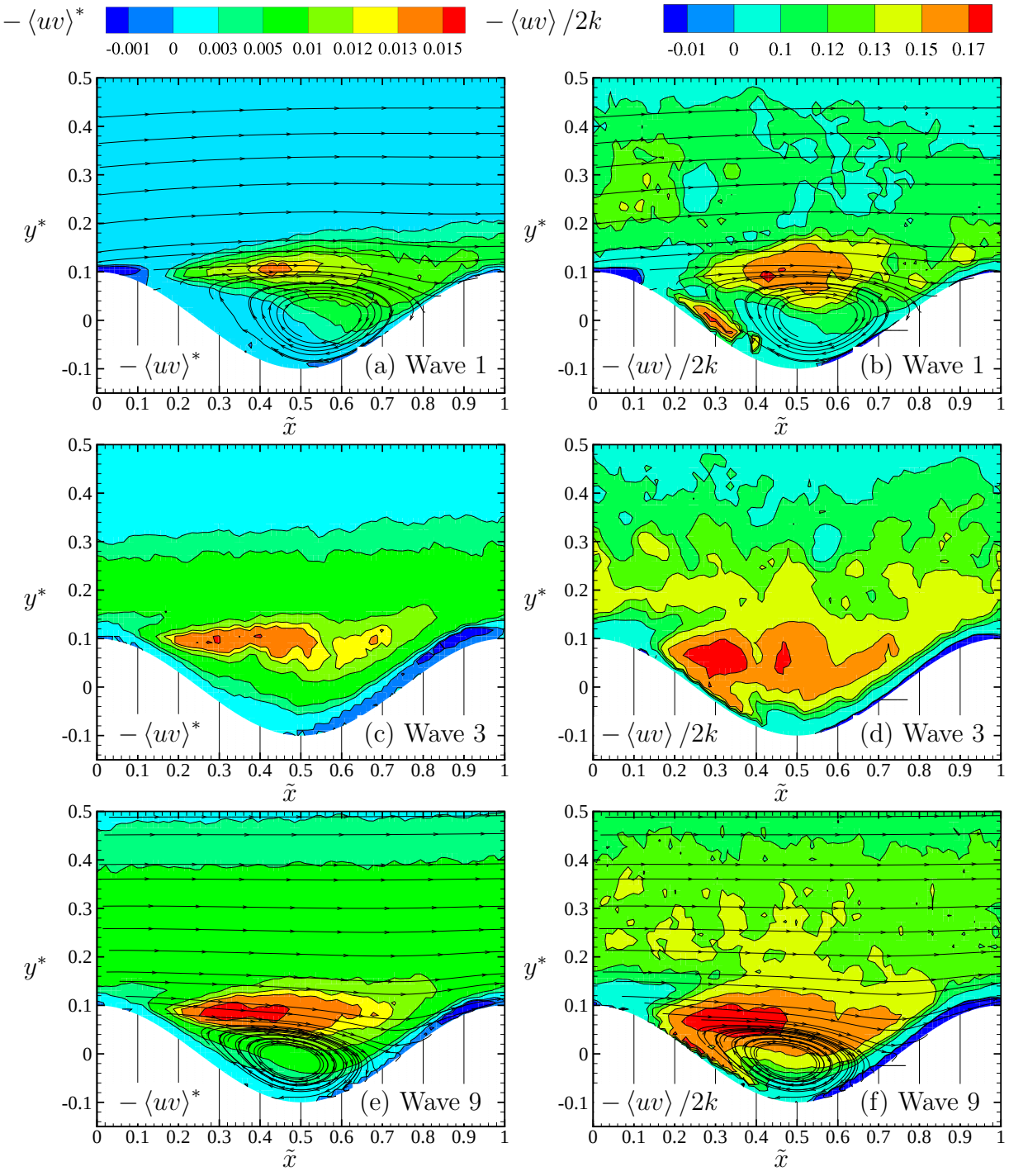

Figure 4.8: Contour plots of dimensionless Reynolds shear stress, $-\langle uv\rangle^*$, at Wave 1 (a), Wave 3 (c), Wave 9 (e), and structural parameter, $-\langle uv\rangle/2k$, at Wave 1 (b), Wave 3 (d), and Wave 9 (f), for $\mathrm{Re_b} = 10700$.

Hudson *et al.* [26] attributed the negative Reynolds shear stress region in the upstream side of Wave 9 to calculations of $-\langle uv \rangle^*$ values using the Cartesian coordinate system, and they showed that they assume positive values if calculated in a boundary-layer coordinate system.

The distribution of Reynolds shear stress is quite different at Wave 1 and 3 compared to at Wave 9, where there is a larger region of high values of Reynolds shear stress in the shear layer above the smaller recirculation zone. The Reynolds shear stress topology indicates a larger momentum and more efficient momentum transport at Wave 9 compared to Wave 1. In Hudson *et al.* [26] the maximum shear stress locations indicated the shear layer centre height, which was evident in the contours plots, where the maximum $-\langle uv \rangle^*$ values are just above the diving streamline, where the shear layer was present. It is observed in Figure 4.9 that there is a maximum value at $\tilde{x} = 0.3$, and a decrease from $\tilde{x} = 0.3$ to 0.7.

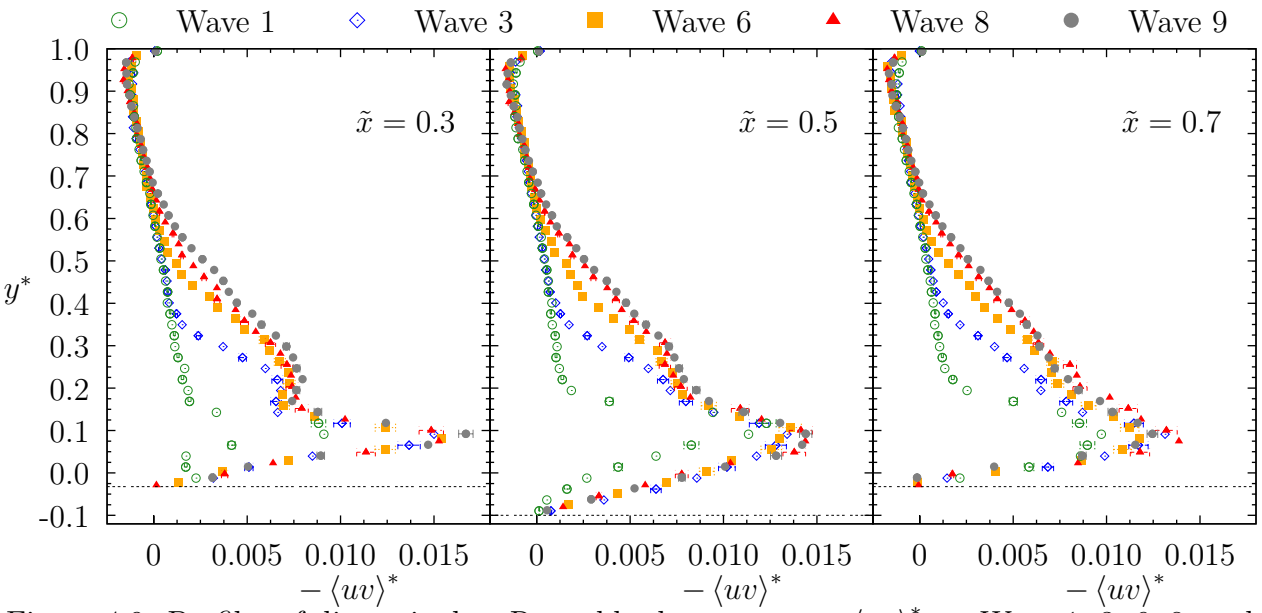

Figure 4.9: Profiles of dimensionless Reynolds shear stress, $-\langle uv \rangle^*$, at Wave 1, 3, 6, 8, and 9 at $\tilde{x}$ = 0.3, 0.5, and 0.7, for $\mathrm{Re_b} = 10700$.

Figure 4.9 also shows a steep increase in $-\langle uv \rangle^*$ from Wave 1 to Wave 6 between $y^* =$

0.2 and $y^* = 0.6$ and a smaller increase from Wave 3 to Wave 8; this trend ceases between Wave 8 and 9. A quantitative study shows this $-\langle uv \rangle^*$ increase. The $\mathrm{RMS}_{\mathrm{RN},-\langle uv \rangle^*}$ values by comparing the experimental data profiles at $\tilde{x} = 0.50$ for Waves 1, 3, 6, 8 to those for Wave 9, yields the following values 25.00%, 13.90%, 7.00%, and 3.25%.

Figure 4.8 also shows, for Waves 1, 3, and 9, contours of the structural parameter, $a_1 = -\langle uv \rangle / 2k$, where k is the turbulent kinetic energy estimated as $k = 0.75(\langle u^2 \rangle + \langle v^2 \rangle)$. The structural parameter is used to estimate the well known turbulence model coefficient, C_μ, which is calculated as $(2 \times a_1)^2$. In many turbulence models (e.g. k–ϵ, R-k–ϵ, k–ω, and others), C_μ has a constant of value 0.09, which means that a_1 value should be 0.15. Figures 4.8 and 4.10 reveal considerable variation in a_1 values, for most of the flow field, and for all waves presented. In Figure 4.10, the a_1 profiles show peak values of more than 0.20 for Waves 9, 8, and 6, at $y^* = 0.1$, which consistently agree with previous findings of higher $\langle u^2 \rangle^*$ and $\langle v^2 \rangle^*$ at that particular location when compared to flat channel flows.

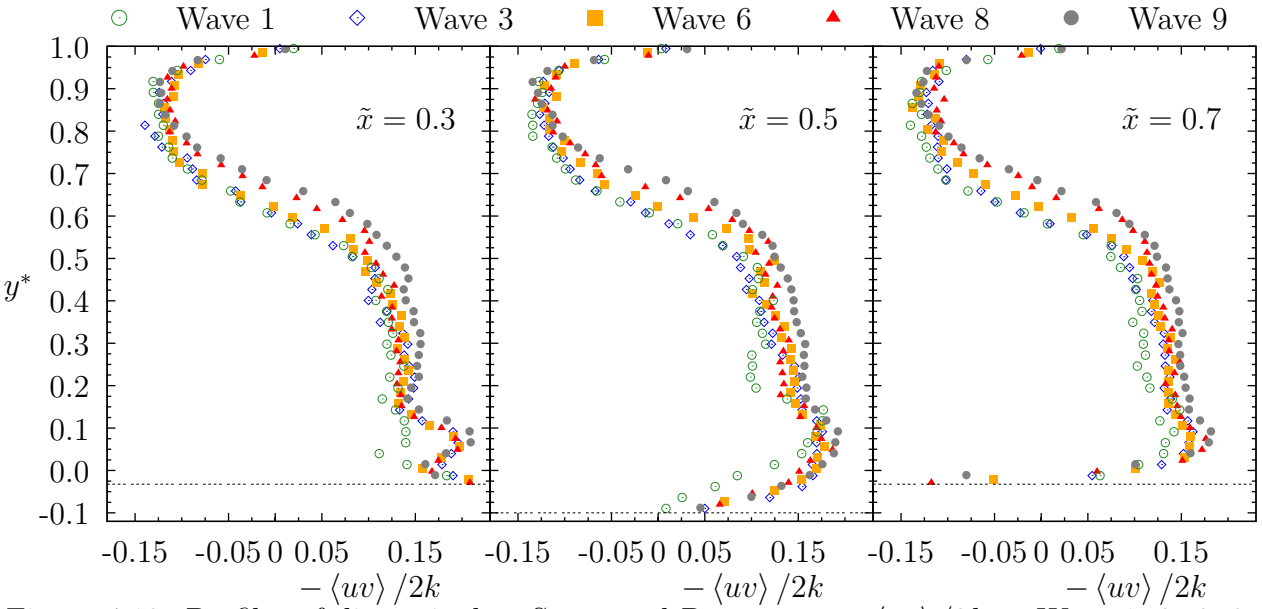

Figure 4.10: Profiles of dimensionless Structural Parameter, $-\langle uv \rangle / 2k$ at Wave 1, 3, 6, 8, and 9 at $\tilde{x} = 0.3$, 0.5, and 0.7, for $\mathrm{Re_b} = 10700$.

The C_μ coefficient calibration in the turbulence models is made in flat wall channels, which makes their performance difficult in conditions where the Reynolds stress are affected differently by the shear layer formation and recirculation region, such as those presented in this experiment. The study of the coefficients such as C_μ could reveal potential deficiencies of some turbulence models. However, it is not attempted here to formulate new turbulence models coefficients but to emphasize some of the inconsistencies between experimentally and modeled obtained flow characteristics.

4.3.3 Reynolds Number Effects in the Reynolds Stresses

Figure 4.11 shows the variation with Reynolds number of the three components of the Reynolds stresses.

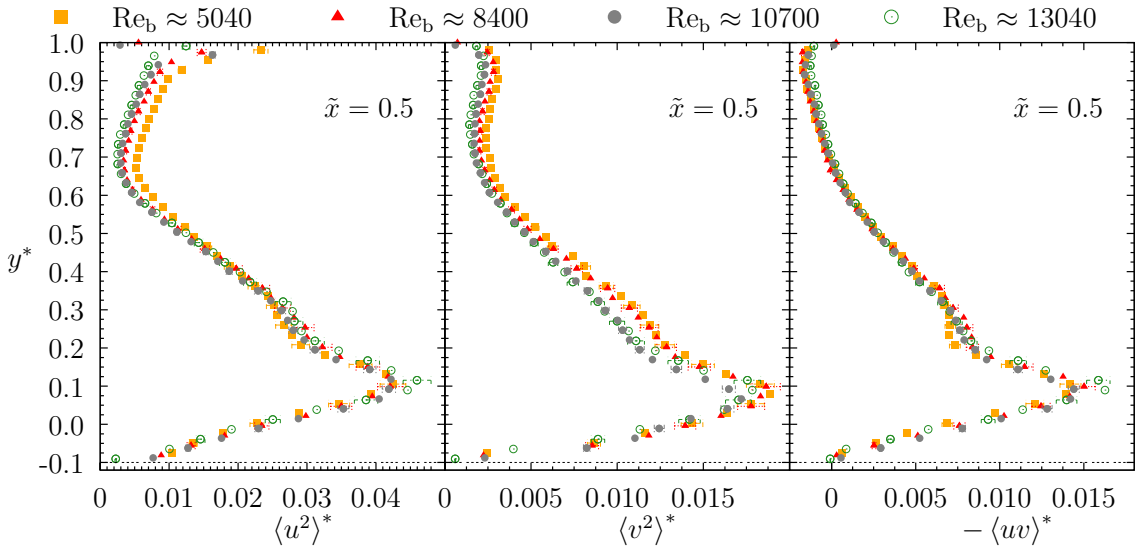

Figure 4.11: Profiles of dimensionless Reynolds normal stresses in the streamwise direction, $\langle u^2 \rangle^*$, wall-normal direction, $\langle v^2 \rangle^*$, and Reynolds shear stress, $-\langle uv \rangle^*$, at Wave 9 and $\tilde{x} = 0.5$, for $\mathrm{Re_b} = 5040, 8400, 10700$, and 13040.

The Reynolds shear stress values are nearly identical for the entire channel for the four Reynolds number. The $-\langle uv \rangle^*$ peak values were almost identical when considering the

uncertainty for all Reynolds numbers, with a maximum value of about 0.015. The streamwise and wall-normal Reynolds stresses exhibited slightly different profiles in the outer region. The $\mathrm{Re_b} = 5040$ results show the most prominent differences in the outer region. For $\langle u^2 \rangle^*$, the profiles for $\mathrm{Re_b} = 13040, 10700$, and 8400 are nearly identical for the entire channel height. For all Reynolds numbers, the peak values of $\langle u^2 \rangle^*$ and $\langle v^2 \rangle^*$ are about 0.046 and 0.018, respectively. In conclusion, the Reynolds number change did not affect these second order statistics significantly.

4.4 Turbulent Kinetic Energy

4.4.1 Turbulent Kinetic Energy Production

The study of the production of turbulent kinetic energy ${P_k}^*$ is fundamental to developing an understanding of turbulence. This section aims to investigate the influence of this geometry on the production of turbulent kinetic energy. Equation (4.1) gives the production of turbulent kinetic energy.

$$\begin{aligned} P_k &= \left\{ - \left\langle u^2 \right\rangle \frac{\partial \left\langle U \right\rangle}{\partial x} - \left\langle v^2 \right\rangle \frac{\partial \left\langle V \right\rangle}{\partial y} \right\} + \left\{ - \left\langle uv \right\rangle \frac{\partial \left\langle U \right\rangle}{\partial y} - \left\langle uv \right\rangle \frac{\partial \left\langle V \right\rangle}{\partial x} \right\} \\ &= \{P_n\} + \{P_s\} \end{aligned} \tag{4.1}$$

This equation is valid when the mean flow and turbulence do not vary in the z-direction. Kruse *et al.* [27] found that the flow is homogeneous in the z-direction at their measured location in the channel center, therefore, the approximation implied in Equation 4.1 is reasonable.

Figure 4.12 shows contours for dimensionless total production of turbulent kinetic energy, ${P_k}^*$, the dimensionless normal component, ${P_n}^*$, and the dimensionless shear stresses component, ${P_s}^*$. These quantities were made dimensionless by multiplying the values by $h/{U_b}^3$.

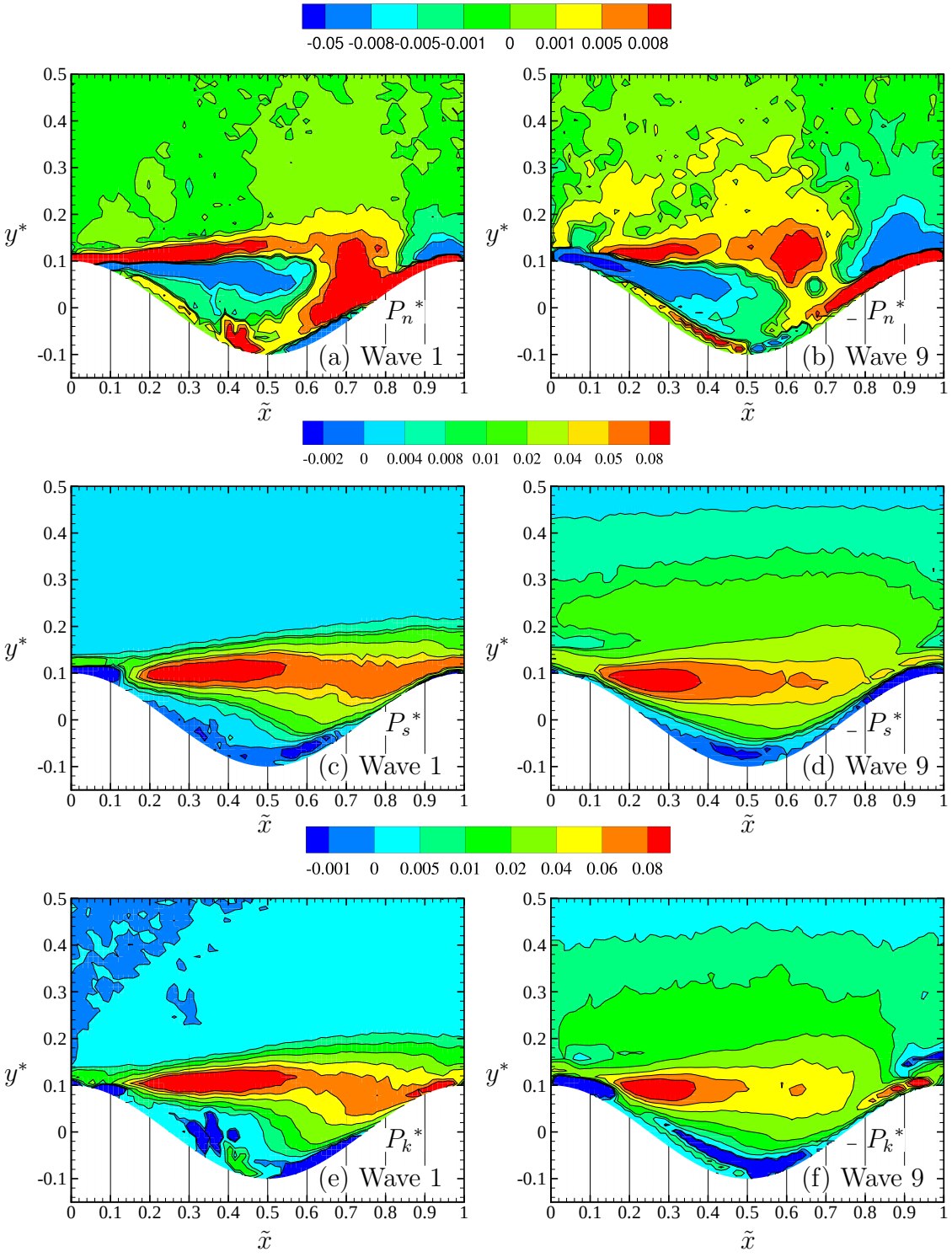

Figure 4.12: Total turbulent kinetic energy production, $P_k{}^*$, normal component P_n^*, and shear component, P_s^* contours at Wave 1 (a, c, e) and at Wave 9 (b, d, f), for $\mathrm{Re_b} \approx 10700$.

${P_n}^*$ is the total contribution from the two normal stresses and ${P_s}^*$ from the shear stresses. Waves 1 and 9 were chosen for the plots in Figure 4.12 to see the evolution of the production terms. Velocity gradients were examined (presented in Appendix D) and it was found that all velocity gradients have considerable magnitudes, in contrast with canonical turbulent shear flows where $-\langle uv \rangle \frac{\partial \langle U \rangle}{\partial y}$ is the only or dominant turbulence production term. Section 4.3 also demonstrated that the Reynolds stresses have unique distributions due to the wavy geometry. Therefore, it is expected that turbulent kinetic energy production will have a unique distribution for this flow because most of the terms could have a significant role in the k production.

Figure 4.12 shows that the P_n^* component at both Waves 1 and 9 is considerably smaller in magnitude than the P_s^* component. The P_n^* positive peak is about 0.008, compared to 0.08 for the P_s^*. That leads to the conclusion that the shear component might dictate the k production for most of the flow field. However, the negative values for P_n^* are about 25 times larger in magnitude than P_s^*. This high P_n^* negative region is observed at Wave 9 at $\tilde{x} \approx 0$ to 0.5 and $y^* \approx 0.1$ with a peak value of about -0.05. For P_s^*, the same region contains portions of small positive values and a positive peak of 0.08. The combination of the two components at that region is shown in the P_k^* contours, where a negative region appears because of the P_n^* influence. At Wave 1, similar dynamics is observed, but with some differences. At Wave 1, the P_n^* negative region starts at $\tilde{x} \approx 0.075$ instead of 0. This component change can be attributed to no influence from a previous wave. Also, at Wave 1, the P_s^* has a negative pocket near the wall, which is not observed at Wave 9 at $\tilde{x} \approx 0$ to 0.1. The P_k^* results for Wave 1 show that the combination of the two components at $\tilde{x} \approx 0$ to 0.5 and $y^* \approx 0.1$, has created a negative region. This region is in fact influenced by the P_s^* rather than the P_n^* component. The positive peak region from P_s^* has slightly reduced the P_k^* results at that region, due P_n^* influence, which is same observed in Wave 9.

A second interesting observation is made in Wave 9, at $y^* \approx 0.1$ and $\tilde{x} \approx 0.8$ to 1. In this region, P_n^* has high positive values very close to the wall and negative values just above this

positive region, whereas P_s^* has low negative values very close to the wall and small positive values just above this negative region. This combination leads to a total production at that region dominated by the normal component of the k production, where the P_k^* contour shows high positive values near the wall and high negative values just above the positive region. At Wave 1, there are significant differences are observed in that same area. First, the negative region just above the positive region, at $y^* \approx 0.1$ and $\tilde{x} \approx 0.8$ to 1 is considerably smaller than in Wave 9. Second, the P_s^* contour does not have the negative region very close to the wall. Figure 4.13 shows the individual terms in Eq. 4.1 at Wave 9.

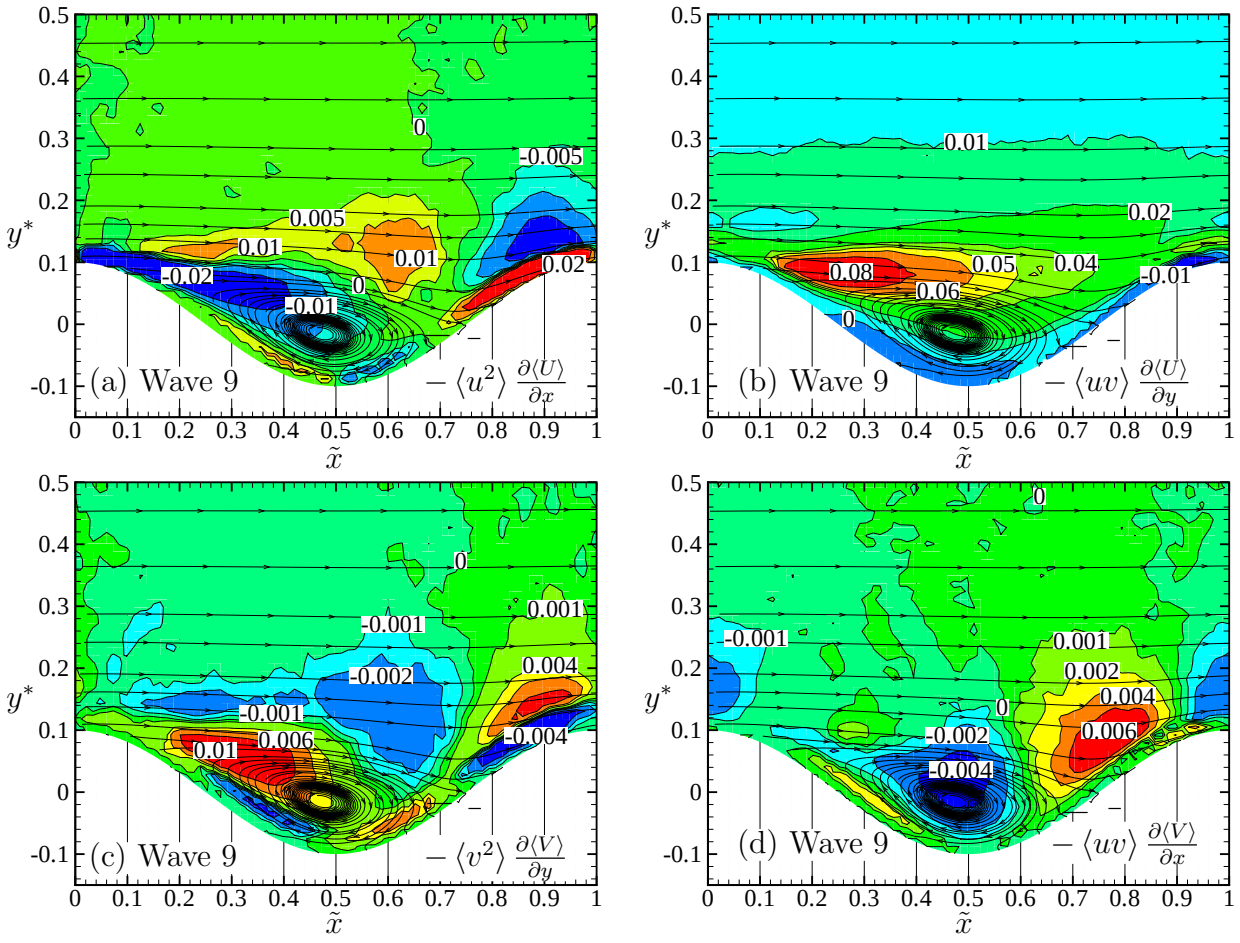

Figure 4.13: Contours of the individual terms in the total turbulent kinetic energy production in Equation 4.1 at Wave 9, for $\mathrm{Re_b} \approx 10700$.

These contours provide insights into how each term contributes to the total production within this flow field. The term $-\langle uv \rangle \frac{\partial \langle U \rangle}{\partial y}$ has the highest peak value (0.08) of the four terms. In Hudson *et al.* [26], the same term was found to be the most dominant throughout most of the two-dimensional field. They also observed that the term $-\langle u^2 \rangle \frac{\partial \langle U \rangle}{\partial x}$ is of the same order of magnitude as the $-\langle uv \rangle \frac{\partial \langle U \rangle}{\partial y}$ term in some regions. The region that extends from $y^* \approx 0$ and $\tilde{x} \approx 0.7$ to $y^* \approx 0.1$ and $\tilde{x} \approx 1$ shows values near 0.02 for the first term whereas the second term has values near -0.01. The other two terms present different patterns throughout the flow field. However, the magnitude of their values is relatively smaller when compared to the other terms.

A more detailed assessment of the turbulent kinetic energy production at Waves 1 and 9 is made in Figures 4.14 and 4.15. One-dimensional profiles of the individual terms in Eq. 4.1 are presented at $\tilde{x} = 0.3$, 0.5, and 0.7, for $\mathrm{Re_b} \approx 10700$ and both waves. The total production, P_k^*, is determined by $-\langle uv \rangle \frac{\partial \langle U \rangle}{\partial y}$, at both Waves 1 and 9 at all locations presented.

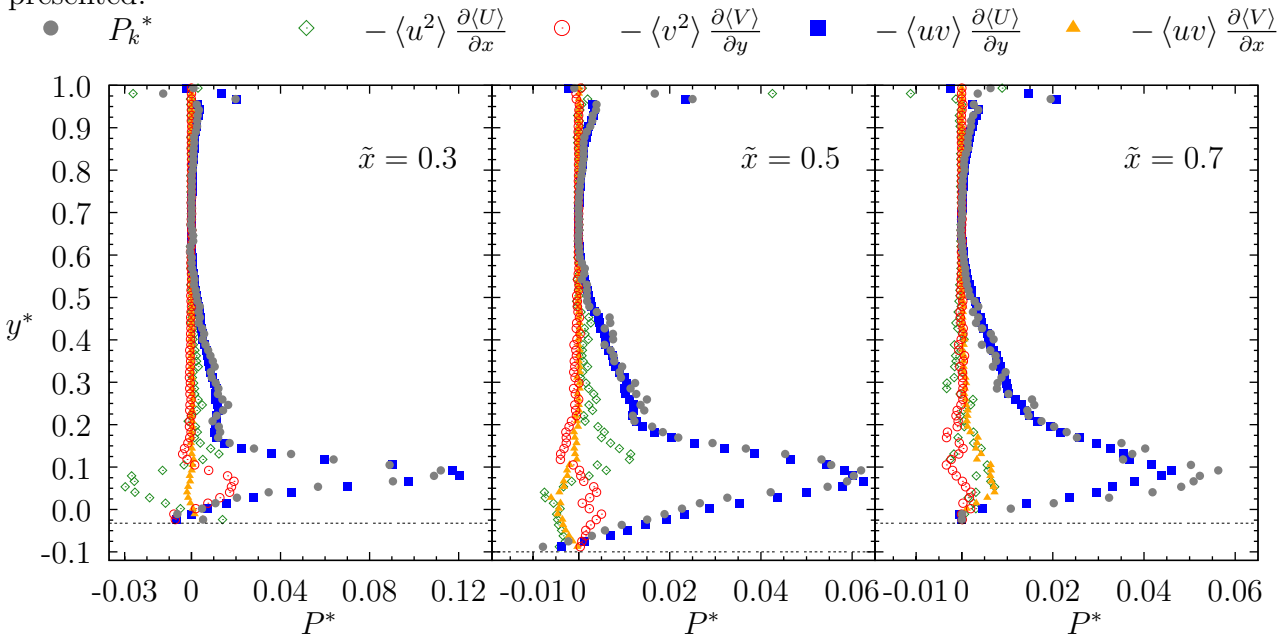

Figure 4.14: Dimensionless individual terms of total production of turbulent kinetic energy, P_k, at Wave 9 and $\tilde{x} = 0.3$, 0.5, and 0.7, for $\mathrm{Re_b} \approx 10700$.

For Wave 9 at $\tilde{x} \approx 0.3$, the $(-\langle u^2 \rangle \frac{\partial \langle U \rangle}{\partial x})$ term has significant negative values, which could potentially decrease the P_k^* values. At that same location, however, the $(-\langle v^2 \rangle \frac{\partial \langle V \rangle}{\partial y})$ term is positive and almost balances out the first term. The $(-\langle uv \rangle \frac{\partial \langle V \rangle}{\partial x})$ term has negligible influence on the total production. In Figure 4.15, the same trends are observed for Wave 1, except that the production extends less along the normal direction of the channel. The extent on Wave 1 is restricted to a smaller portion of the channel height and the P_k^* peaks are 0.16 at Wave 1 compared to 0.12 at Wave 9.

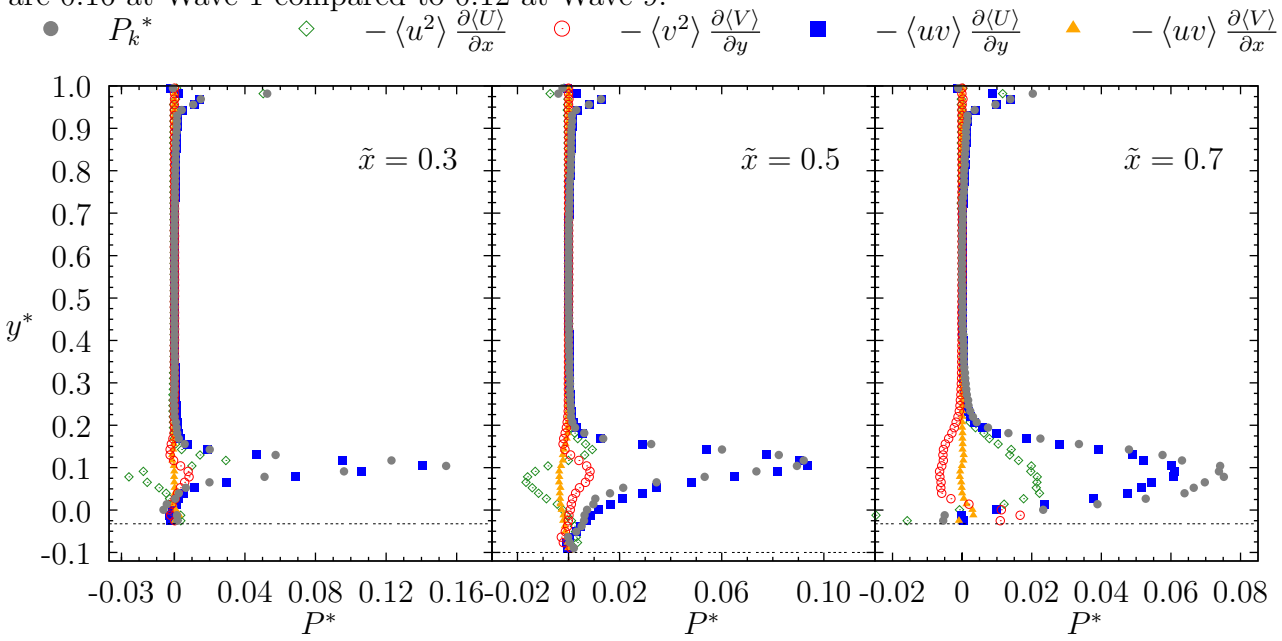

Figure 4.15: Dimensionless individual terms of total production of turbulent kinetic energy, P_k, at Wave 1 and $\tilde{x}$ = 0.3, 0.5, and 0.7, for $\mathrm{Re_b} \approx 10700$.

For Wave 9 at $\tilde{x} = 0.5$, the $-\langle u^2 \rangle \frac{\partial \langle U \rangle}{\partial x}$ term has slight influence in P_k^* between $y^* \approx 0.2$ to 0.5, while the greatest contribution still comes from the $-\langle uv \rangle \frac{\partial \langle U \rangle}{\partial y}$ term along the entire channel height. At Wave 1, a difference in behavior exists, where first and the last term have opposite signs at about $y^* \approx 0.08$, and they cancel out their influence in the total production. At $\tilde{x} = 0.5$, Wave 1 has a higher P_k^* peak value (0.01) compared to Wave 9 (0.07). At $\tilde{x}$ = 0.7, the $-\langle u^2 \rangle \frac{\partial \langle U \rangle}{\partial x}$ and $-\langle uv \rangle \frac{\partial \langle V \rangle}{\partial x}$ term are not negligible at Wave 9. Because the total

production is higher than the $-\langle uv\rangle \frac{\partial\langle U\rangle}{\partial y}$ term alone at $y^* \approx 0$ to 0.2, both terms increased the P_k^* total production at Wave 9. When observing Wave 1, only the $-\langle u^2\rangle \frac{\partial\langle U\rangle}{\partial x}$ term helped increase the total production and it has a higher influence on P_k^* at Wave 1 than at Wave 9. Again, the peak value of P_k^* at Wave 1 (0.08) is larger than the peak value at Wave 9 (0.06). Overall, the term $-\langle u^2\rangle \frac{\partial\langle U\rangle}{\partial x}$ switches from negative to positive values, from $\tilde{x} = 0.3$ to $\tilde{x}$=0.7. This is mostly evident at Wave 1, but also occurs at Wave 9. It is also noted that the peak of the total production is considerably higher at Wave 1 than at Wave 9.

4.5 Summary: Experimental Results

The experimental results are summarized in Table 4.3. The recirculation region was analyzed in Section 4.1, prior to the mean velocities to establish the overall view of the flow over the wavy geometry. The first order statistics ($\langle U\rangle^*$ and $\langle V\rangle^*$) were thoroughly discussed in Section 4.2 and provided insights on the mean velocity quantities characteristics and the influence of the recirculation region and the shear layer region in these mean quantities. The three Reynolds stresses ($\langle u^2\rangle^*$, $\langle v^2\rangle^*$, and $-\langle uv\rangle^*$) were presented and discussed in Section 4.3; they provided insights in the turbulence field for this particular problem allowing a further understanding of the Reynolds stresses and turbulence itself. Turbulent kinetic energy production, P_k^*, was examined to further advance the knowledge of the mechanisms of energy transfer within the flow field in such an anisotropic conditions.

Table 4.3: Experimental studies summary: turbulent flow over a wavy channel.

Reynolds Number	Flow Quantities Studied
5040, 8400	$\langle U\rangle^*$,$\langle V\rangle^*$,$\langle u^2\rangle^*$,$\langle v^2\rangle^*$,$-\langle uv\rangle^*$, a_1, P_k^*, P_n^*, P_s^*, and
10700, and 13040	velocity gradients ($\partial\langle U\rangle/\partial x$, $\partial\langle U\rangle/\partial y$, $\partial\langle V\rangle/\partial x$, and $\partial\langle V\rangle/\partial y$)

Chapter 5

Numerical Results and Discussions - Wavy Wall

Seven RANS turbulence models were used to study the wavy wall effects on the turbulent flow characteristics. The turbulence models used were: k–ϵ, R-k–ϵ, k–ω, SST, LRR-IP, LPS, SMC-BSL, and the SMC-ω, as described in Section 3.2.3. In this chapter, the models' predictions are compared to previously presented experimental data. The comparisons are performed within the developing region, which extends from Wave 1 to Wave 8, and the fully periodic region after Wave 8. The wavy channel geometry is the same as the one described in Section 2.2.1 and the bulk Reynolds number ($\mathrm{Re_b}$) is 10700. The main purpose of comparison is assessing the predictive performance of these turbulence models for this complex turbulent flow.

5.1 Mean Velocity and Recirculation Region

A comparison of flow characteristics over different waves reveals the development of the flow until a fully periodic region is established, as was demonstrated in Chapter 4. Contour plots of the results of some of the turbulence models are presented first, followed by velocity profiles for all the models. The initial contour plots are used to compare the results of models with different degrees of agreement with the experimental results. Contours plots of $\langle U \rangle^*$ at Waves 1 and 9 are presented from the numerical results for the k–ϵ and SST models in Fig. 5.1 and for the LPS and LRR-IP models in Fig. 5.2.

The recirculation region and the shear layer formation from the experiments were shown in Figure 4.1. It was shown that there are considerable differences in the recirculation region extent and height between Waves 1 and 9. The results from the k–ϵ model show much smaller regions of negative $\langle U \rangle^*$ compared to the experimental results. In addition, the k–ϵ results do not accurately reproduce the change in the size of the negative velocity region

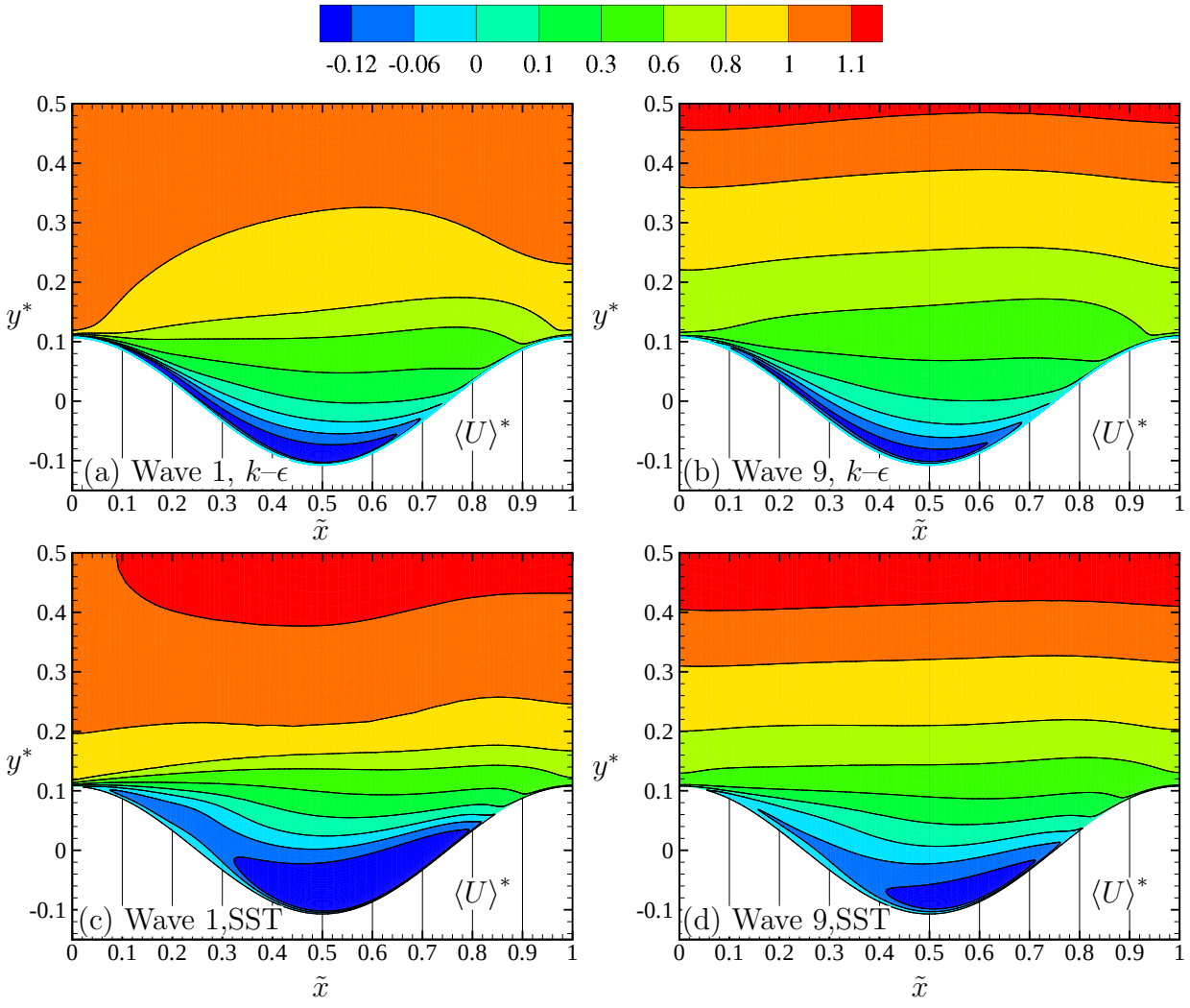

Figure 5.1: Contour plots of dimensionless streamwise mean velocity, $\langle U \rangle^*$, at $\mathrm{Re_b} = 10700$ for the k–ϵ model (a) at Wave 1 and (b) at Wave 9, and for the SST model (c) at Wave 1 and (d) at Wave 9.

between Waves 1 and 9. The results of the SST model, on the other hand, show regions that are closer to those in the experimental results, including a reduction in the size of the negative velocity region at Wave 9 compared to at Wave 1.

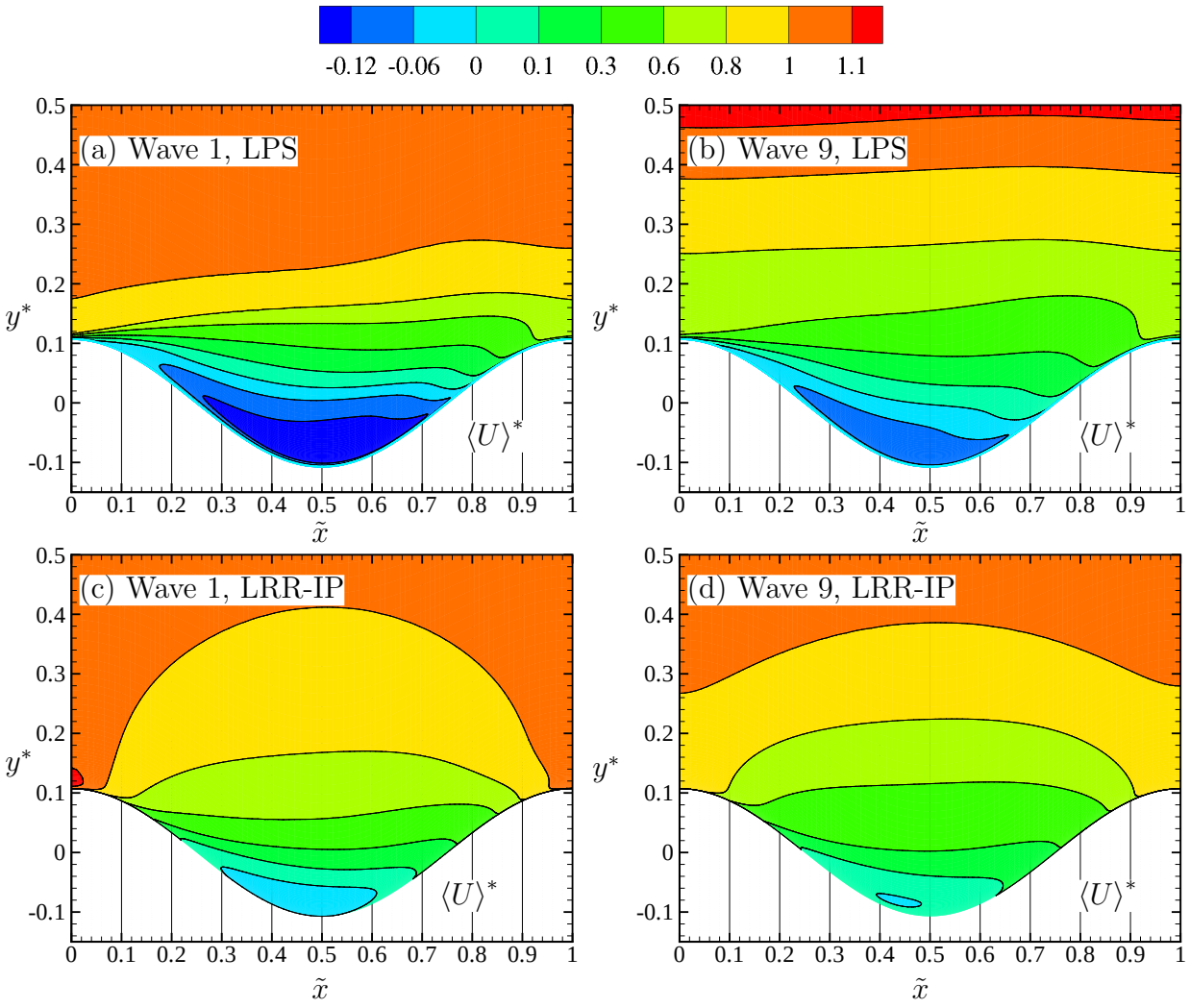

Figure 5.2: Contour plots of dimensionless streamwise mean velocity, $\langle U \rangle^*$, at $\mathrm{Re_b} = 10700$ for the LPS model (a) at Wave 1 and (b) at Wave 9, and for the LRR-IP model (c) at Wave 1 and (d) at Wave 9.

In Fig. 5.1 (a) and (b) for the k–ϵ model and in Fig. 5.2 (a) and (b) for the LPS model,

it is shown that the highest streamwise velocity contour location is shifted upwards in the y direction for Wave 9 compared to Wave 1 in these numerical results, which is in agreement with the experimental data; this behaviour is more evident in velocity profiles presented later. The results from the LPS model in Figs. 5.2(a) and 5.2(b) are qualitatively similar to the experimental results, whereas those from the LRR-IP in Figs. 5.2 (c) and 5.2(d) are qualitatively quite different. The LRR-IP model did not predict any regions of negative $\langle U \rangle^*$, and thus no recirculation zone.

The numerical results for the dimensionless streamwise mean velocity, at Waves 1, 3, and 6 at $\tilde{x} = 0.50$ are shown in Fig. 5.3 for all the eddy viscosity models and in Fig. 5.4 for all the SMC models.

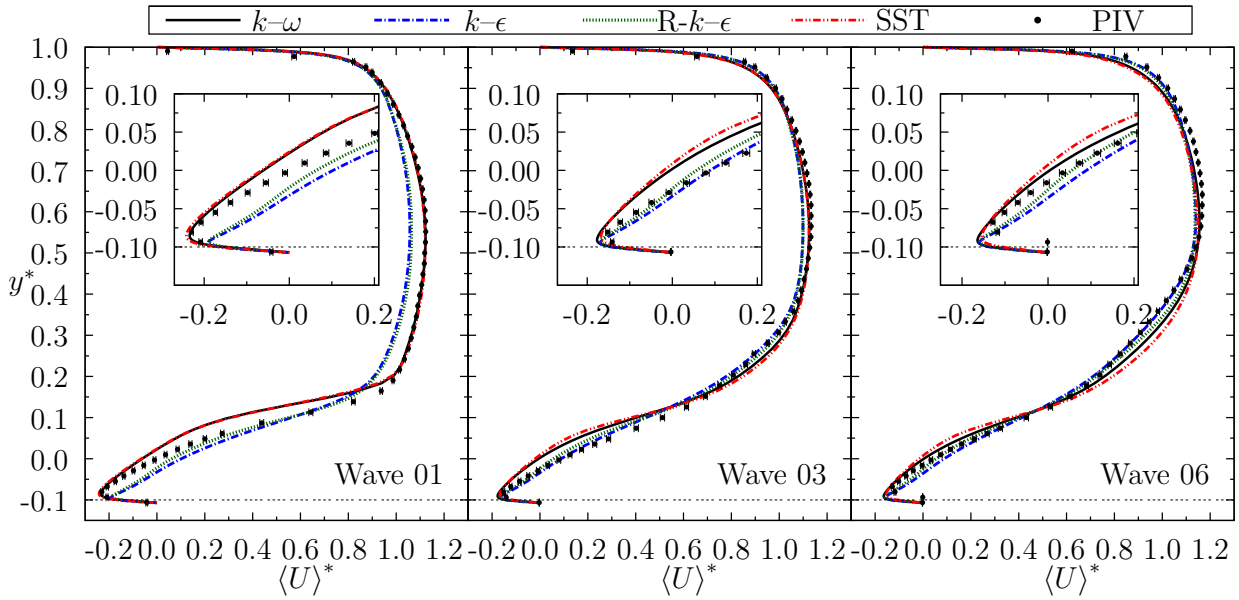

Figure 5.3: Eddy viscosity models: Dimensionless mean velocity, $\langle U \rangle^*$, distribution for Waves 1, 3, and 6 at $\tilde{x} = 0.5$ for $\mathrm{Re_b} = 10700$.

Figure 5.3 shows that the maximum $\langle U \rangle^*$ value is shifted upwards more in Wave 6 compared to Wave 1. This trend was noted earlier regarding differences between Waves 1 and 9. This upward shift is also observed in Fig. 5.4. The shift was not observed between

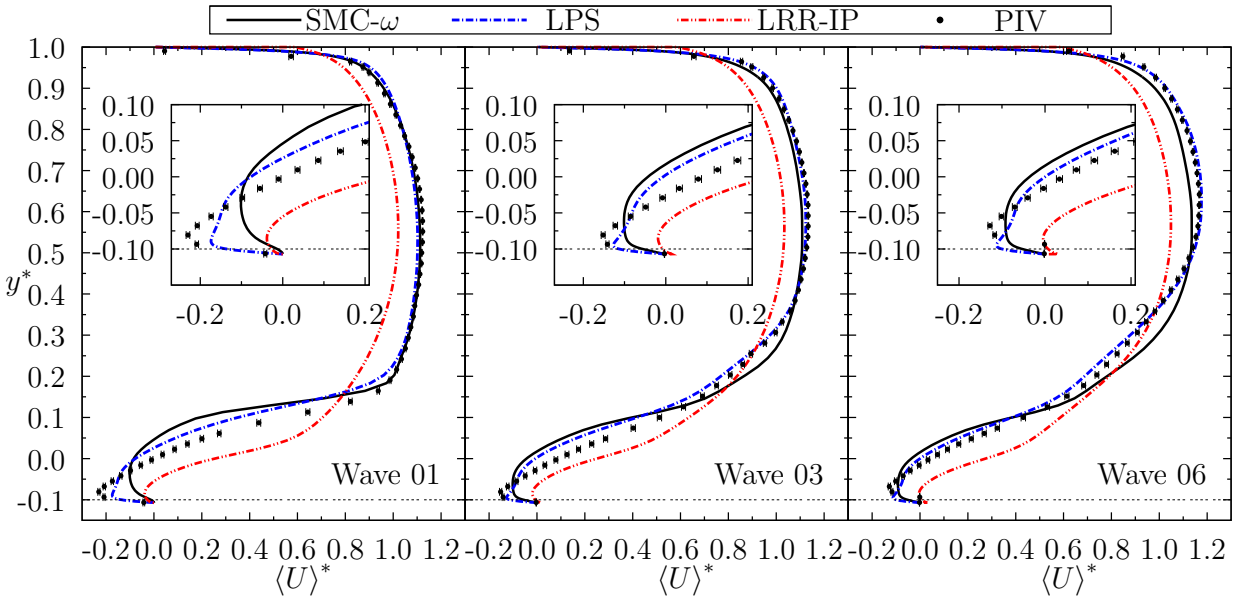

Figure 5.4: SMC models: Dimensionless mean velocity, $\langle U \rangle^*$, distribution for Waves 1, 3 and 6 at $\tilde{x} = 0.5$ for $\mathrm{Re_b} = 10700$.

Wave 8 and 9 for all models, which indicates a periodic flow after Wave 8. No matter what wave location, the maximum local streamwise mean velocity is located further away from the wall when compared to a flat channel turbulent flow.

The profile shape changes significantly from wave to wave in Figs. 5.3 and 5.4. In general, the eddy viscosity and SMC models predictions agreed with the experimental data, with the exception of the LRR-IP model. In the near wall region, the k–ϵ and R-k–ϵ model predicted negative $\langle U \rangle^*$ values for Wave 1 and 6 that are smaller in magnitude when compared to the experimental data. In the near wall region for Waves 1, 3, and 6, the SST and k–ω models predicted negative $\langle U \rangle^*$ values that are larger in magnitude when compared to the experimental data. The SMC models predictions for LPS and SMC-ω are in good overall agreement but the LRR-IP model did not predict the flow with good accuracy. The poor prediction is most likely associated with the standard wall treatment implemented with this model. The other two models, LPS and SMC-ω, show good agreement with the experimental

data for the streamwise mean velocity, except for the near wall region, where both models under predicted the maximum reverse flow.

Table 5.1 summarizes the $\mathrm{RMS}_{\mathrm{RN},\langle U\rangle^*}$ values (calculated using Equation (3.6)) when turbulence models results are compared to the experimental data at Waves 1, 3, and 6. Two regions were analyzed: the entire channel region and the near-wall region, which extends from the bottom wavy wall up to $y^* = 0.1$. Throughout the results section, the number of points used for the RMS calculations was 86 for the entire channel region and 17 for the near-wall region.

Table 5.1: $\mathrm{RMS}_{\mathrm{RN},\langle U\rangle^*}$ [%] values comparing numerical to experimental data, at $\tilde{x} = 0.5$

Model	Entire Height			Near-Wall		
	Wave			Wave		
	1	3	6	1	3	6
Standard k–ϵ	6.4	4.1	2.4	6.6	2.8	4.0
Realizable k–ϵ	5.7	4.2	2.5	4.5	3.9	3.5
Wilcox k–ω	6.5	4.9	3.4	8.0	7.3	4.3
SST	6.5	5.5	4.7	8.1	9.1	5.8
LRR-IP	11.9	9.1	9.5	18.5	11.7	14.7
LPS	6.2	4.6	2.5	7.2	6.7	3.8
SMC-ω	8.3	5.8	4.5	13.0	9.6	5.6

The $\mathrm{RMS}_{\mathrm{RN},\langle U\rangle^*}$ values in Table 5.1 demonstrate that the results from the eddy viscosity models are similar in both regions and that, in general, the lowest deviation from the experimental results was found at Wave 6. The flow in the near-wall region is captured with reasonable accuracy by the eddy viscosity models even though, for most of the models, there are slightly higher $\mathrm{RMS}_{\mathrm{RN},\langle U\rangle^*}$ values in the near-wall region than for the entire channel height. The LRR-IP model prediction inaccuracy is quantified in Table 5.1, where the model has significantly higher $\mathrm{RMS}_{\mathrm{RN},\langle U\rangle^*}$ values. The LPS model had the lowest $\mathrm{RMS}_{\mathrm{RN},\langle U\rangle^*}$ values among the SMC models and had agreement that was consistent with the eddy viscosity

models.

To characterize the recirculation region, the locations of the separation ($\tilde{x}_s$) and reattachment ($\tilde{x}_r$) of the flow are used. These values have been presented for the periodic region in previous studies. In this work, the values were examined to characterize the development of the flow. Table 5.2 presents the dimensionless separation and reattachment locations for Waves 1, 3, 6, and 9 for the experiments and all the turbulence models. The experimental values were discussed in detail in Section 4.1. Recall that the uncertainty of the experimental values of $\tilde{x}_s$ is ± 0.01 at Wave 1 and less than 0.01 at the other waves. For $\tilde{x}_r$, the uncertainty is ± 0.02 at Wave 1 and ± 0.01 for the other waves. The experimental results show that the separation and reattachment locations were very similar at Waves 3, 6 and 9; the differences are close to or within the uncertainty of determining the locations. At Wave 1, however, the separation and reattachment locations are quite different, revealing a larger recirculation region at Wave 1.

Table 5.2 shows that, for all waves and for all models except the LRR-IP model, the numerical predictions of the reattachment location are in reasonable agreement with the experiment with a trend toward over-prediction whereas the separation location is significantly under-predicted. The SST model predicted the lowest $\tilde{x}_s$ values for Waves 1, 6 and 9, and largest values of $\tilde{x}_r$ for Waves 3, 6 and 9. In all cases, the predicted recirculation region is larger than the experiments, and a recirculation size reduction was observed from Wave 1 to Wave 3. The numerical predictions of the separation and reattachment locations for Wave 6 are the same as for Wave 9 for all turbulence models. The numerical results in the fully periodic region show early separation and later reattachment for all turbulence models, except for the LRR-IP model that failed to predict a recirculation region. In conclusion, the two-equation model (k–ϵ) and the SMC model (LPS) had the most accurate prediction of the experimental and LES reattachment locations in Table 5.2.

Kuzan *et al.* [24] stated that the separation point occurs where the pressure gradient is

Table 5.2: Summary of experimental and numerical results for the recirculation region locations: separation ($\tilde{x}_s$) and reattachment ($\tilde{x}_r$).

Model	separation ($\tilde{x}_s$)				reattachment ($\tilde{x}_r$)			
	Wave				Wave			
	1	3	6	9	1	3	6	9
Experiments	0.11	0.14	0.14	0.13	0.80	0.72	0.73	0.72
Standard k–ϵ	0.04	0.05	0.06	0.06	0.74	0.77	0.74	0.74
Realizable k–ϵ	0.04	0.05	0.06	0.06	0.76	0.76	0.76	0.76
Wilcox k–ω	0.03	0.05	0.06	0.06	0.84	0.79	0.77	0.77
SST	0.02	0.05	0.05	0.05	0.84	0.81	0.81	0.81
LRR-IP	-	-	-	-	-	-	-	-
LPS	0.03	0.06	0.06	0.06	0.80	0.74	0.74	0.74
SMC-ω	0.03	0.05	0.06	0.06	0.81	0.78	0.77	0.77
Standard k–ϵ (Patel *et al.* [36])	n/a	n/a	n/a	0.08	n/a	n/a	n/a	0.73
LES (Henn and Sykes [37])	n/a	n/a	n/a	0.06	n/a	n/a	n/a	0.73
LES (Cui *et al.* [38])	n/a	n/a	n/a	0.1	n/a	n/a	n/a	0.7

unfavorable and the reattachment occurs just upstream of the maximum pressure. Martins Segunda *et al.* [43] found agreement with this statement. Their pressure predictions for the k–ω, SST, and BSL model (ω-based two-equations) and the $SMC-\omega$, and $SMC-BSL$ SMC models showed that the maximum pressure location prediction for all the ω-based models was positioned downstream from the experimental location. This is consistent because all models predicted reattachment locations further downstream when compared to the experimental data [25]. Their SMC models based on the dissipation rate (ϵ) equation were the SSG, LRR-IP, and LRR-IQ. Their pressure distribution results are not in agreement with experimental data and previous models results, so it was not possible to conclude about the maximum pressure location relation to the reattachment location.

The early separation in the fully periodic region in the current numerical simulations is not surprising, as the literature review shows that simulations using standard k–ϵ in

Patel *et al.* [36], 3D domains using the LES method used by Henn and Sykes [37], and LES in Cui *et al.* [38] also under-predicted the separation location for the same wavy characteristics and similar Reynolds number (Table 5.2). The LPS and Standard k–ϵ model reattachment locations ($\tilde{x}_r$) prediction are in great agreement with the experiments. Their prediction also agrees with the LES results from Henn and Sykes [37] and Cui *et al.* [38]. The early separation is seen for other wavy characteristics and Reynolds number in previous numerical studies listed in Table 2.2. For example, the SST model in Knotek and Jicha [41], standard k–ϵ in Khaled *et al.* [42], and DNS in Cherukat *et al.* [34] predicted the separation at 0.13, 0.13 and 0.14, respectively. Those values are under predicting Hudson *et al.* [26] experiment value of 0.3.

5.2 Wall Shear Stress Distributions for the Fully Periodic Region

The dimensionless wall shear stress, τ_w^*, profiles along Wave 8 are shown in Figures 5.5 for the two-equation models and in Figure 5.6 for the SMC models. The position where separation occurs was determined by the transition between a positive to a negative τ_w^* value for all turbulence models predictions, whereas the reattachment was determined by a transition from a negative to a positive τ_w^* value. The present numerical predictions for $\mathrm{Re_b} = 10700$ are compared to the experimental work [25] and the LES simulation results [37] at $\mathrm{Re_b} = 12000$, since the τ_w^* values were not obtained in this experiment.

Among the two-equation models, the k–ϵ and R-k–ϵ models had the closest prediction of the reattachment locations when compared to the LES [37], whereas the k–ω and SST models predicted higher reattachment locations. However, all models, including the LES, over predicted the experimental [25] reattachment location. The separation location is nearly identical between all two-equation models and the LES results [37]; they are all, however,

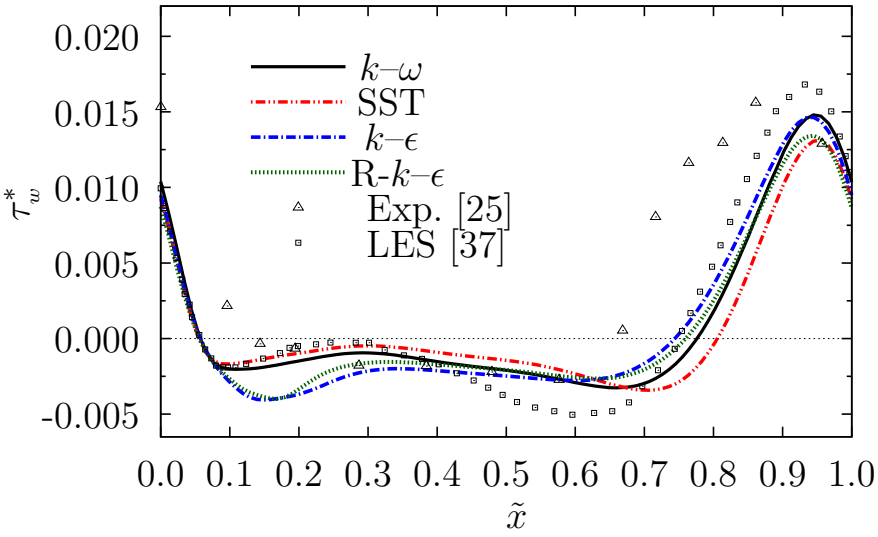

Figure 5.5: Two-equation models: Dimensionless wall shear stress, τ_w^*, distribution for Wave 8 at $\mathrm{Re_b} = 10700$.

lower than the experimental data [25]. The LPS model (Figure 5.6) shows excellent comparison to the LES [37] reattachment location, and it also predicted well the τ_w^* peak after the reattachment location. The LPS model performed better than any two-equation or SMC

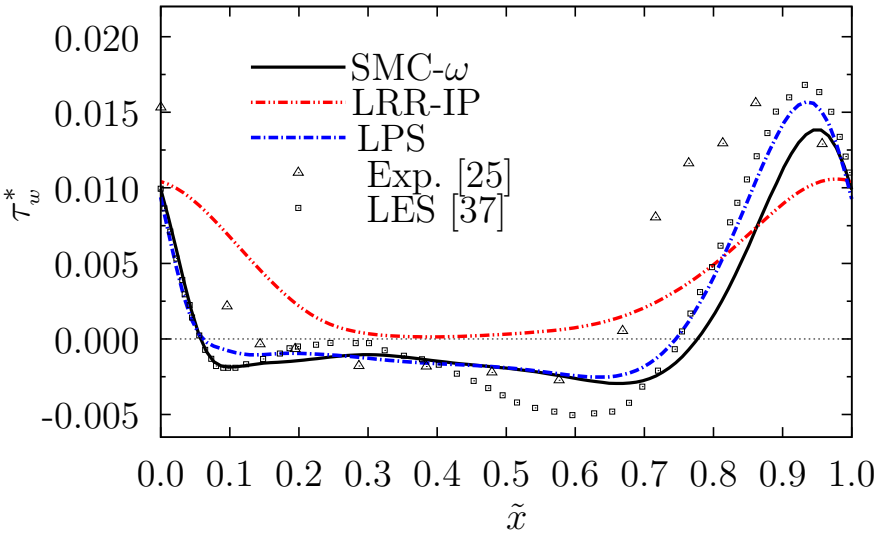

Figure 5.6: SMC models: Dimensionless wall shear stress, τ_w^*, distribution for Wave 8 at $\mathrm{Re_b} = 10700$.

model to predict the τ_w^* peak. The LRR-IP model has no transition between a positive to a negative value of the wall shear stress, confirming its inability to predict the recirculation region. The SMC-ω model has a later reattachment location, and it under-estimated the τ_w^* peak. The separation positions are the same for the different turbulence models presented and the value is the same as the LES simulation by Henn and Skyes [37] but they are lower when compared to the numerical work by Patel *et al.* [36], as presented in Table 5.2. All the numerical results presented are lower when compared to experimental data [25] and the current experimental results.

In the work of Martins Segunda *et al.* [43], the SMC models that used standard wall functions (SSG, LRR-IP, and LRR-IQ) showed no recirculation region, failing to predict the main feature of this flow. They also found that SMC models that do not use standard wall functions would be suitable for this geometry and flow conditions. This is demonstrated in this thesis, where the LPS turbulence model has great prediction of the recirculation region and other main features of the flow, whereas the LRR-IP has not predicted the recirculation region and other flow features such as the Reynolds stresses in the later Section 5.4.

In Buckles *et al.* [25], wall shear stress, τ_w^*, and pressure distributions results were also analyzed in detail and they revealed that the reattachment (negative to positive τ_w^* value location) occurred 0.05 λ before the maximum wall pressure. This agrees with the observations made in Kuzan *et al.* [24] that the reattachment occurs just upstream of the maximum pressure. At the same location, the Buckles *et al.* [25] study shows a high peak of the root-mean-square value of pressure fluctuations, $\sqrt{\langle p^2 \rangle}^*$, which they suggested to not be only caused by the reattachment location, but also influenced by the fluid flow impinging on the wall due to reattachment.

5.3 Mean Velocity for the Fully Periodic Region

The predictions of streamwise mean velocity are presented at three axial locations in Wave 9 in Fig. 5.7 for the eddy viscosity models. The profiles shows higher negative $\langle U \rangle^*$ values at $\tilde{x} = 0.7$ for the eddy viscosity models when compared to the experimental data, which is consistent with the slightly higher values of reattachment locations in Table 5.2. Figure 5.7 shows that all the eddy viscosity models performed similarly. The standard and realizable k–ϵ models had slightly better prediction than the other eddy viscosity models for the entire channel height.

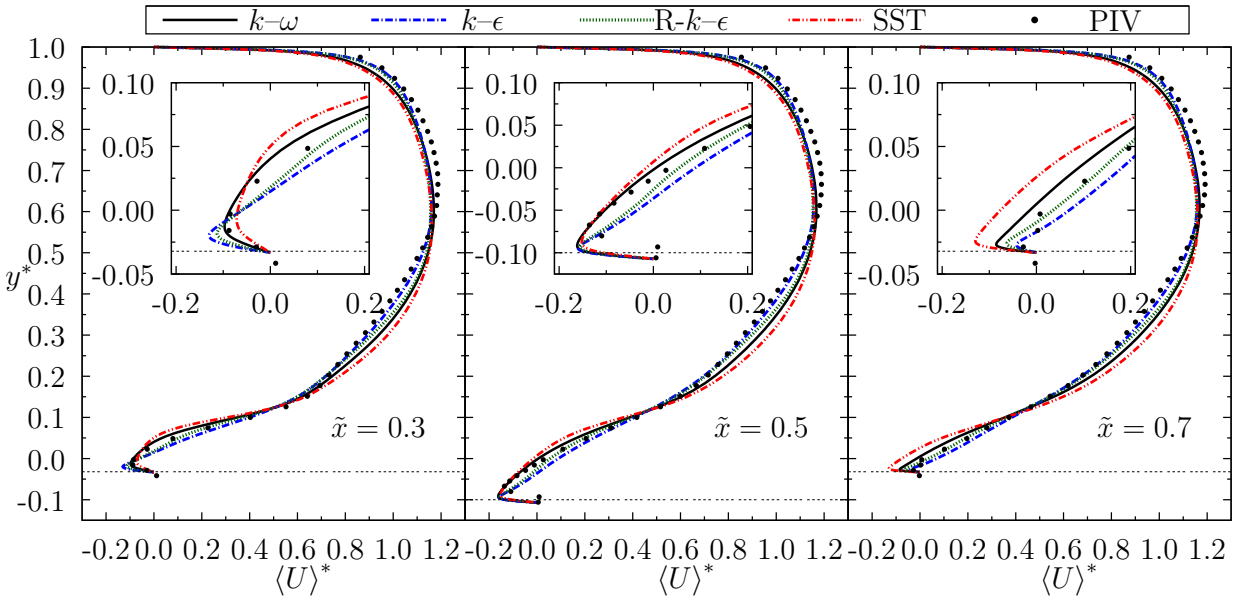

Figure 5.7: Eddy viscosity models: Dimensionless streamwise mean velocity, $\langle U \rangle^*$, distribution for Wave 9, at $\tilde{x} = 0.3$, 0.5, and 0.7 for $\mathrm{Re_b} = 10700$.

The results for the SMC models for the streamwise mean velocity are presented in Fig. 5.8 along Wave 9. The profiles for the LRR-IP model indicate that it did not predict reverse flow, as mentioned earlier. The LPS model had the best performance among the SMC models, in both the near-wall region and across the entire channel height. The SMC-ω model agreed

fairly well with experiments.

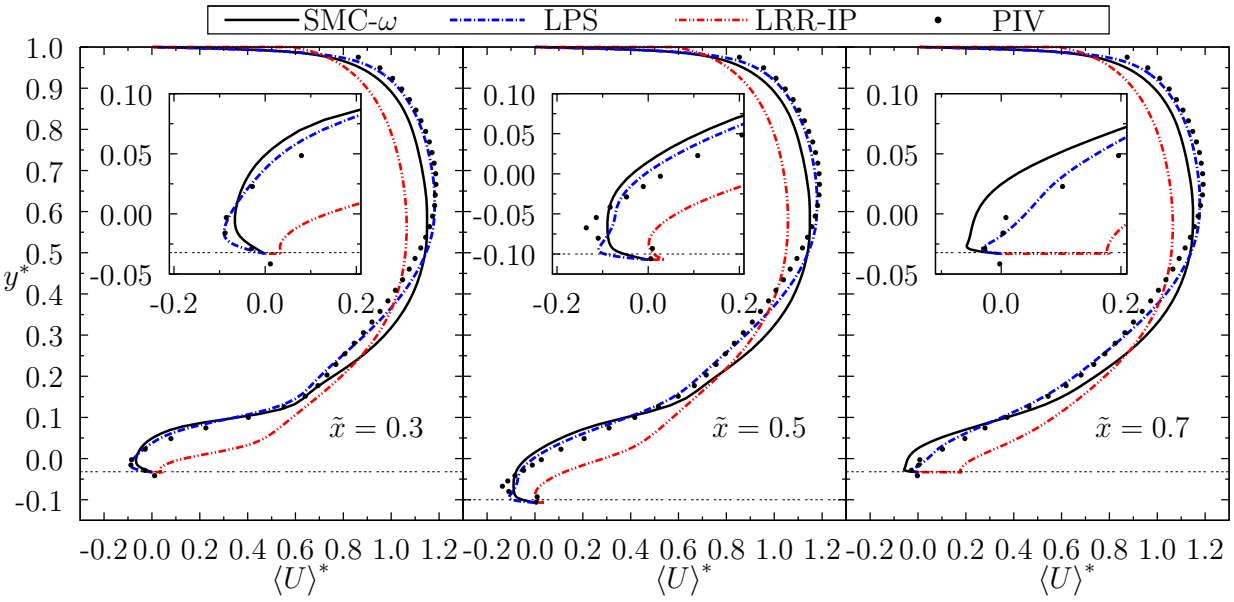

Figure 5.8: SMC models: Dimensionless streamwise mean velocity, $\langle U \rangle^*$, distribution for Wave 9, at $\tilde{x} = 0.3$, 0.5, and 0.7 for $\mathrm{Re_b} = 10700$.

Table 5.3 summarizes the $\mathrm{RMS}_{\mathrm{RN},\langle U \rangle^*}$ values at Wave 9, quantifying the profiles differences observed in Figs. 5.7 and 5.8. The values in Table 5.3 confirm that the eddy viscosity models all performed well. The SST model had the highest $\mathrm{RMS}_{\mathrm{RN},\langle U \rangle^*}$ values of all the eddy viscosity models. Among the SMC models, the LPS model had the lowest $\mathrm{RMS}_{\mathrm{RN},\langle U \rangle^*}$ values. It is important to note that, the experimental measurement uncertainty of 1% for the streamwise mean velocity represented a maximum change of less than 0.05% in Table 5.3 values. Therefore, the measurement uncertainty has no significant effect on the $\mathrm{RMS}_{\mathrm{RN},\langle U \rangle^*}$ values. A sensitivity study of the measurement locations demonstrated a maximum change for the entire channel and near wall region of 0.35% and 1.20%, respectively, when the measurement location was shifted by $\tilde{x} = 0.0166$, which corresponds to more than one IA size. This test indicated that uncertainty in the measurement location can have a significant effect on the $\mathrm{RMS}_{\mathrm{RN},\langle U \rangle^*}$ values.

Table 5.3: $\mathrm{RMS}_{\mathrm{RN},\langle U\rangle^*}$ [%] values comparing numerical to experimental data at Wave 9.

Model	Entire Height			Near-Wall		
	Location ($\tilde{x}$)			Location ($\tilde{x}$)		
	0.3	0.5	0.7	0.3	0.5	0.7
Standard k–ϵ	2.3	2.8	2.3	3.4	4.6	2.7
Realizable k–ϵ	2.8	3.1	2.8	2.1	3.8	1.3
k–ω	3.6	3.7	3.9	3.3	4.0	3.6
SST	5.2	5.2	6.1	6.1	5.5	7.5
LRR-IP	11.3	10.0	10.9	22.3	15.3	17.3
LPS	2.2	2.5	2.2	3.4	3.7	2.2
SMC-ω	4.8	5.0	5.6	5.2	5.4	6.2

In conclusion, the overall performance of the eddy viscosity models regarding predicting the mean flow is similar to the SMC models. This was demonstrated well in the earlier sections for the flow development when comparing the mean velocities and recirculation region sizes. At the fully periodic region, this was also demonstrated well by the mean velocity profiles at different locations at Wave 9, and the wall shear stress predictions. The eddy viscosity models successfully predicted the mean flow considering the observed large-scale anisotropy from the experimental data. The results also demonstrated the importance of near-wall treatment and its implication in the results. The LRR-IP model that used the Scalable Wall Function (SWF) had very poor mean flow predictions. Also, other SMC models had poor predictions when using the SWF, such as the SSG and LRR-IQ reported in Martins Segunda *et al.* [43]. The k–ϵ, R-k–ϵ, and LPS models used the Enhanced Wall Treatment (EWT) and they had in overall the best predictions. The k–ω, SST, and SMC-ω models that used the Automatic Wall Functions (AWF) also had good predictions, but slightly worse than the models with the EWT.

5.4 Reynolds Stresses

This section presents the numerical results for three Reynolds stresses predicted from the Second Moment Closure (SMC) models LPS, LRR-IP, and SMC-ω described in Section 3.2.3. The three Reynolds stresses examined here are the dimensionless streamwise normal stress $\langle u^2 \rangle^*$, the dimensionless wall-normal Reynolds normal stress $\langle v^2 \rangle^*$, and the dimensionless Reynolds shear stress $-\langle uv \rangle^*$, that were directly measured in the experiments. The numerical results are compared against the experimental data from this work. The stresses are made dimensionless by normalization using U_b^2.

Contours of $\langle u^2 \rangle^*$ predicted from the three SMC models at Waves 1 and 9 are plotted in Figure 5.9. The predictions from the three models show considerable differences among them at both Wave 1 and 9. The LPS model presents the most consistent results when compared to experimental data seen earlier in Figure 4.5. The LRR-IP model had the greatest deviation from the experiments among the three models; it also had the least accurate mean velocity predictions, as discussed in Section 5.3. All the SMC models consistently predicted the previously mentioned feature in the experiments of an increase of the influence in the outer region of Wave 9 when compared to Wave 1.

More detailed analyses of the $\langle u^2 \rangle^*$ numerical contours in Figure 5.9 show the following main differences from the experimental data: (1) the LPS model predicted $\langle u^2 \rangle^*$ maximum values above 0.045 compared to 0.04 measured in the experiments, (2) the LPS model predicted a significantly larger region of elevated turbulence level than observed in the experiment, (3) the LRR-IP model failed to predict the experimental $\langle u^2 \rangle^*$ values in the near-wall, and shear layer regions, and (4) the SMC-ω model gave better predictions than the LRR-IP model but was still quite different from the experimental and the LPS model results with, for example, much lower overall $\langle u^2 \rangle^*$ values and a completely different location for the $\langle u^2 \rangle^*$ peak.

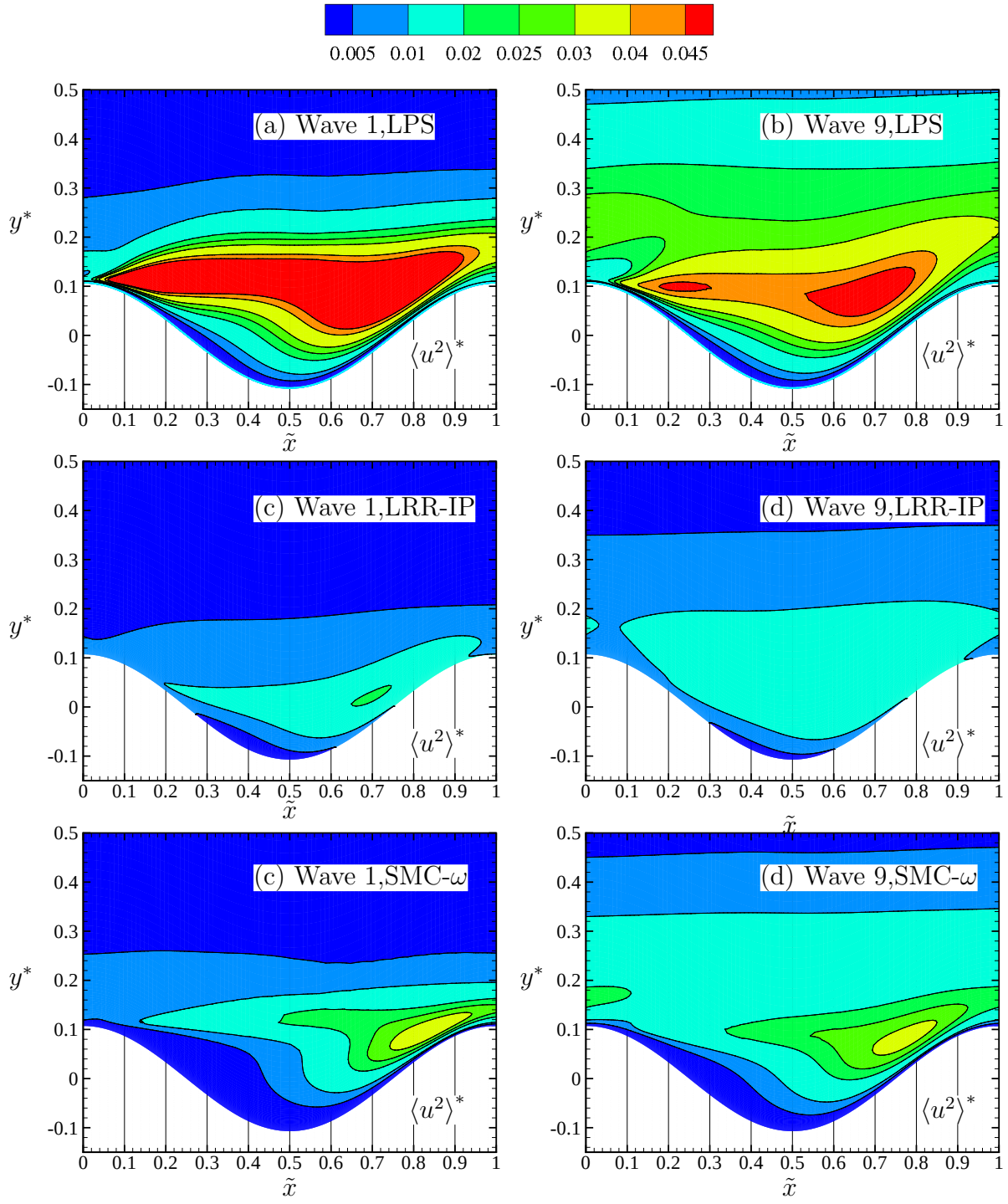

Figure 5.9: Contour plots of dimensionless streamwise Reynolds normal stresses, $\langle u^2 \rangle^*$, at $\mathrm{Re_b} = 10700$ for the LPS model (a) at Wave 1 and (b) at Wave 9, for the LRR-IP model (c) at Wave 1 and (d) at Wave 9, and for the SMC-ω model (e) at Wave 1 and (f) at Wave 9.

Contours of $\langle v^2 \rangle^*$ from the SMC model for Waves 1 and 9 are plotted in Figure 5.10. Similar to the $\langle u^2 \rangle^*$ results, the $\langle v^2 \rangle^*$ predictions also demonstrated an increasing influence in the outer region at Wave 9 when compared to Wave 1. The three models results show considerable differences among them at both Wave 1 and 9. The LPS model produced the most consistent results when compared to experimental data; the LRR-IP model had the greatest deviation from the experiments among the three models.

A closer examination of the results in Figure 5.10 reveals the following main differences between the numerical results and the experimental data: (1) the LPS model predicted $\langle v^2 \rangle^*$ maximum values above 0.025, which is 56% higher than the experimental maximum of about 0.016, (2) the LPS model results have a region of $\langle v^2 \rangle^*$ values between 0.015 to 0.020 that corresponds to a similar region in the experiments predictions between 0.014 to 0.016, revealing similar $\langle v^2 \rangle^*$ predictions overall, but with slight higher values overall and with notably higher values after $\tilde{x}$=0.7, (3) the LRR-IP model failed to predict the experimental $\langle v^2 \rangle^*$ values in the near-wall and shear layer regions and showed significant peak after $\tilde{x}$=0.7, which is inconsistent with the experimental peak, and (4) the SMC-ω model results show a slightly better prediction than the LRR-IP model but are still quite different from the experimental and LPS model results, with for example, much lower overall $\langle v^2 \rangle^*$ values and a completely different location for the $\langle v^2 \rangle^*$ peak.

Section 4.3 of the experimental results demonstrated that this flow is anisotropic by examining the Reynolds normal stresses. The SMC models compute the individual Reynolds stresses, whereas the eddy viscosity models consider the flow to be isotropic and use a model for the Reynolds stresses. The expectation that SMC models should always have better predictions of this anisotropic flow is not supported by the results here. Only the LPS model had good prediction of the mean flow and Reynolds stresses.

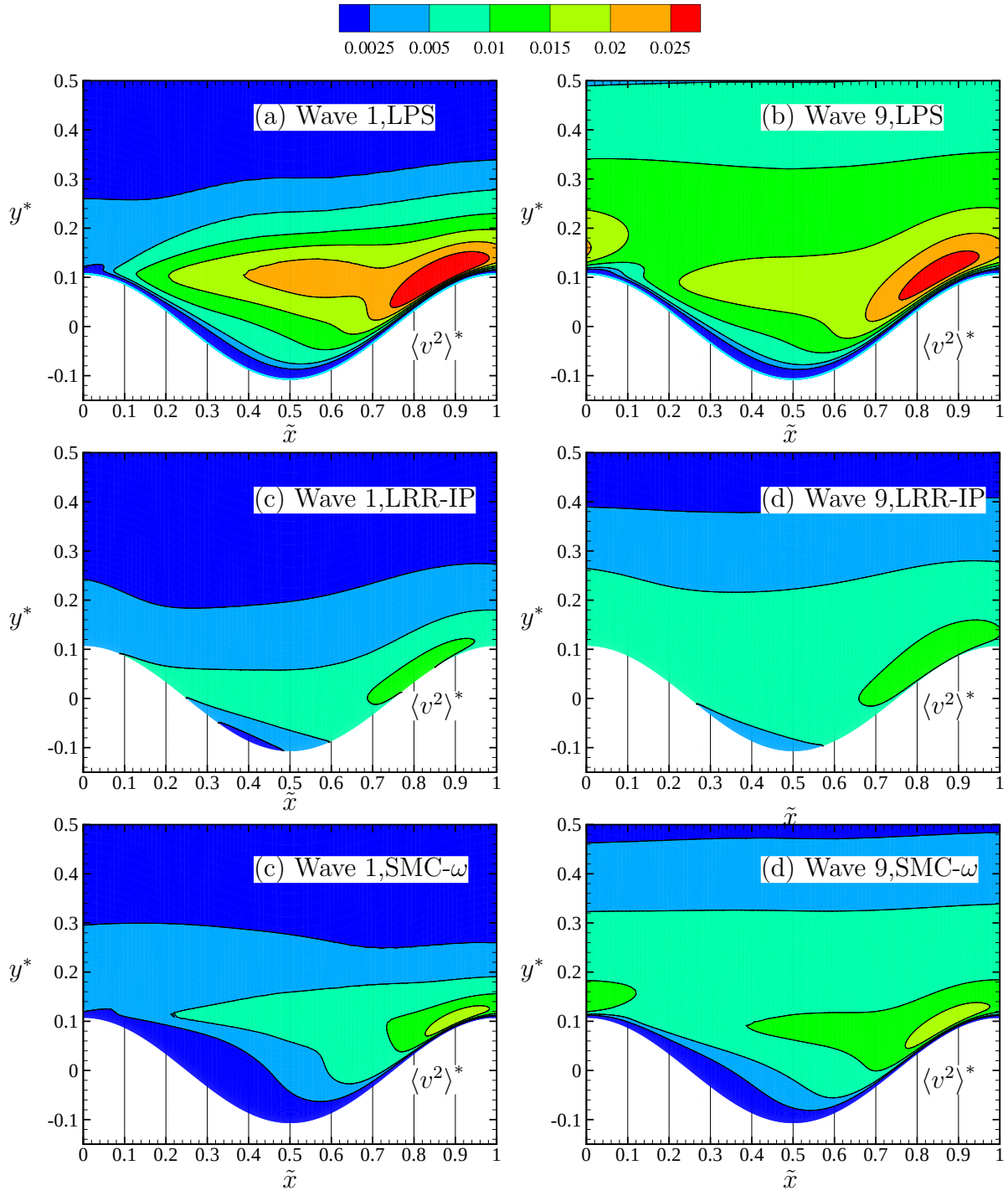

Figure 5.10: Contour plots of dimensionless wall normal Reynolds normal stresses, $\langle v^2 \rangle^*$, at $\mathrm{Re_b} = 10700$ for the LPS model (a) at Wave 1 and (b) at Wave 9, for the LRR-IP model (c) at Wave 1 and (d) at Wave 9, and for the SMC-ω model (e) at Wave 1 and (f) at Wave 9.

Contours of the SMC model predictions of dimensionless Reynolds shear stress, $-\langle uv \rangle^*$, for Waves 1 and 9 are plotted in Figure 5.11. The three distributions are quite different from each other. The experimental contours of the dimensionless Reynolds shear stress at Waves 1 and 9 were plotted in Figure 4.8. The results form the LPS model are closest to the experimental results because it has a higher region of Reynolds shear stress in the shear layer above the recirculation zone. The extent of that region is significantly over-predicted compared to the experiment. In the experiments, there was also a pocket of negative Reynolds shear stress at the entrance to Wave 1, which is not reproduced by any of the SMC models. The measured Reynolds shear stress is quite different at Wave 9 from the numerical predictions, where there is a larger region of high values of Reynolds shear stress in the shear layer.

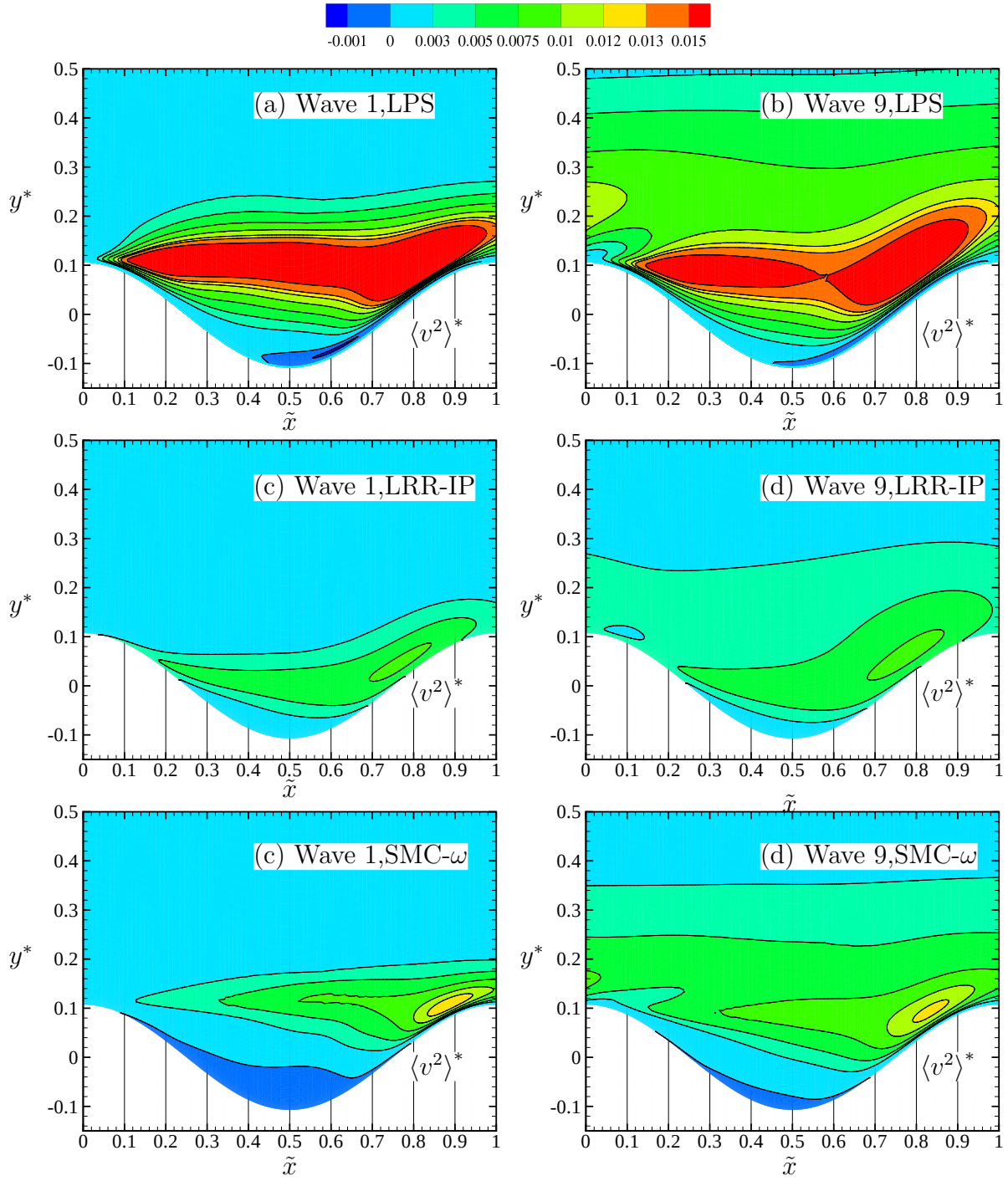

Figure 5.11: Contour plots of dimensionless Reynolds shear stress, $-\langle uv \rangle^*$, at $\mathrm{Re_b} = 10700$ for the LPS model (a) at Wave 1 and (b) at Wave 9, for the LRR-IP model (c) at Wave 1 and (d) at Wave 9, and for the SMC-ω model (e) at Wave 1 and (f) at Wave 9.

5.4.1 Reynolds stresses one-dimensional profiles

Figure 5.12 shows the $\langle u^2 \rangle^*$ and Figure 5.13 $\langle v^2 \rangle^*$ profiles predicted from the three SMC models at Wave 9 at $\tilde{x}$ = 0.3, 0.5, and 0.7 compared with the experimental data. For all three $\tilde{x}$ locations, the predictions are very similar among the models and experiments in the core region y^*=0.65 to 0.75. The models predicted $\langle v^2 \rangle^*$ values of about 0.001 for the three $\tilde{x}$ locations; this value is four times smaller than $\langle u^2 \rangle^*$ values (0.004) at the same region.

The $\langle u^2 \rangle^*$ values are significantly affected by the wavy wall below y^*=0.65, where the LPS model prediction of $\langle u^2 \rangle^*$ increased until reaching a maximum of 0.057 at y^* = 0.1 at $\tilde{x}$ = 0.3. A similar trend is seen at $\tilde{x}$ = 0.5 and 0.7, with peaks of 0.057 and 0.060, respectively, at y^* = 0.1. Note, that the experiments had values of 0.046, 0.042 and 0.042, at $\tilde{x}$ = 0.3, 0.5, and 0.7, respectively. The plots show that the LPS model had the best overall prediction all the three locations. However, it over predicted the experiments peaks by about 23%, 35%, and 42% at $\tilde{x}$ = 0.3, 0.5, and 0.7, respectively. Both the SMC-ω and LRR-IP models had considerably lower values and the LRR-IP model has the greatest deviation among them.

The LPS model predictions of $\langle v^2 \rangle^*$ increased until reaching a maximum of 0.030 at y^* = 0.05 for $\tilde{x}$ = 0.7. A similar trend is seen at $\tilde{x}$ = 0.3 and 0.5, with respective peaks of 0.021 and 0.022 at y^* = 0.1. The experiments, however, show a decrease along the wave, where the $\langle v^2 \rangle^*$ peaks are 0.018, 0.017 and 0.015, at $\tilde{x}$ = 0.3, 0.5, and 0.7, respectively. The plots show that the LPS model had the best overall prediction at all the three locations. However, it over predicted the experiments peaks by about 67%, 23%, and 50% at $\tilde{x}$ = 0.3, 0.5, and 0.7, respectively. At $\tilde{x}$ = 0.7, the SMC-ω had a better prediction for $\langle v^2 \rangle^*$. Both SMC-ω and LRR-IP models had considerably lower values, where the LRR-IP has the greatest deviation among them. The $\langle u^2 \rangle^*$ peaks are predicted slightly better than the $\langle v^2 \rangle^*$ peaks.

The Reynolds shear stress profiles from the SMC models at the three axial locations in Wave 9 are presented in Fig. 5.14. When examining the contour plot of the Reynolds shear stress for the experimental data, it was observed that there was a maximum value at $\tilde{x}$=0.3,

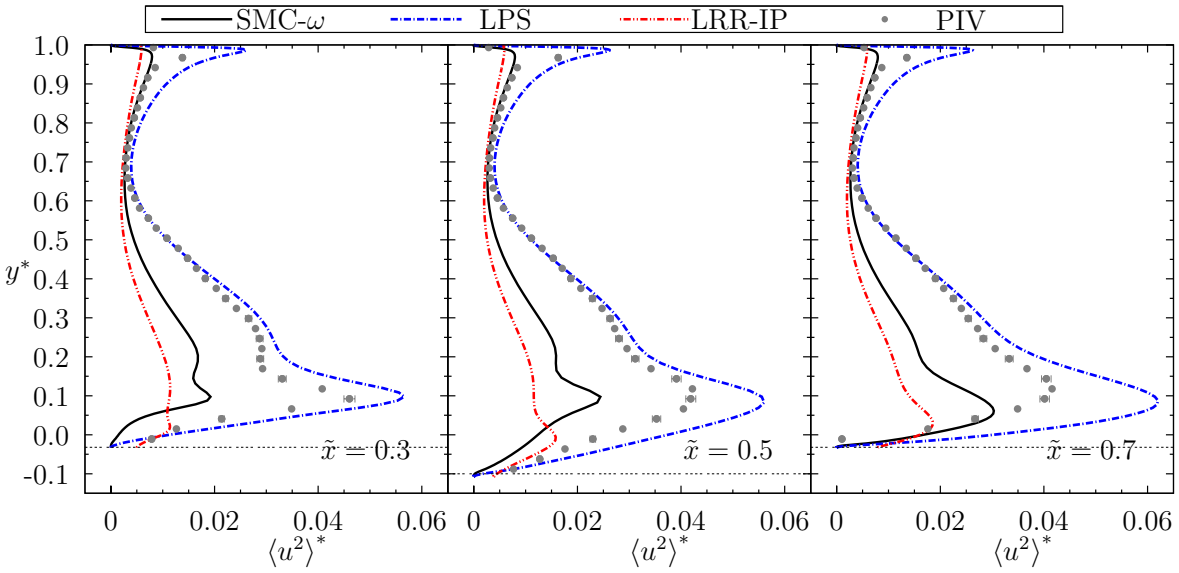

Figure 5.12: SMC models: Dimensionless streamwise Reynolds normal stresses, $\langle u^2 \rangle^*$, distributions at $\mathrm{Re_b} = 10700$ for Wave 9 at $\tilde{x} = 0.3$, 0.5, and 0.7.

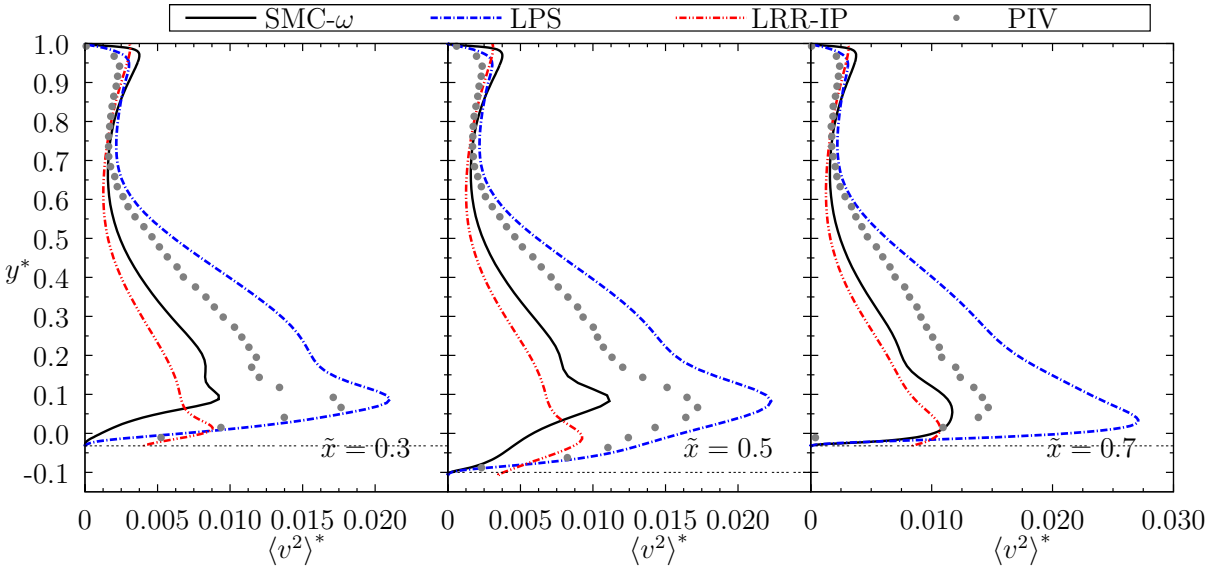

Figure 5.13: SMC models: Dimensionless wall normal Reynolds normal stresses, $\langle v^2 \rangle^*$, distributions at $\mathrm{Re_b} = 10700$ for Wave 9 at $\tilde{x} = 0.3$, 0.5, and 0.7.

and a decrease from $\tilde{x} = 0.3$ to 0.7. The LPS model has the best overall agreement with the experimental data. The LRR-IP model has significant deviations from the experimental data at all locations presented at Wave 9. The LPS model agreed fairly well at $\tilde{x} = 0.3$. It is noteworthy that all models failed to predict the correct levels of Reynolds shear stress at $\tilde{x}$ = 0.7. The SMC turbulence models also failed to predict the $-\langle uv \rangle^*$ decrease from $\tilde{x} = 0.5$ to 0.7 that was seen in the experimental data. Table 5.4 summarizes the$\mathrm{RMS}_{\mathrm{RN},-\langle uv \rangle^*}$ values for the predictions shown in Fig. 5.14. All models show relatively large $\mathrm{RMS}_{\mathrm{RN},-\langle uv \rangle^*}$ values in both the near-wall and entire channel regions.

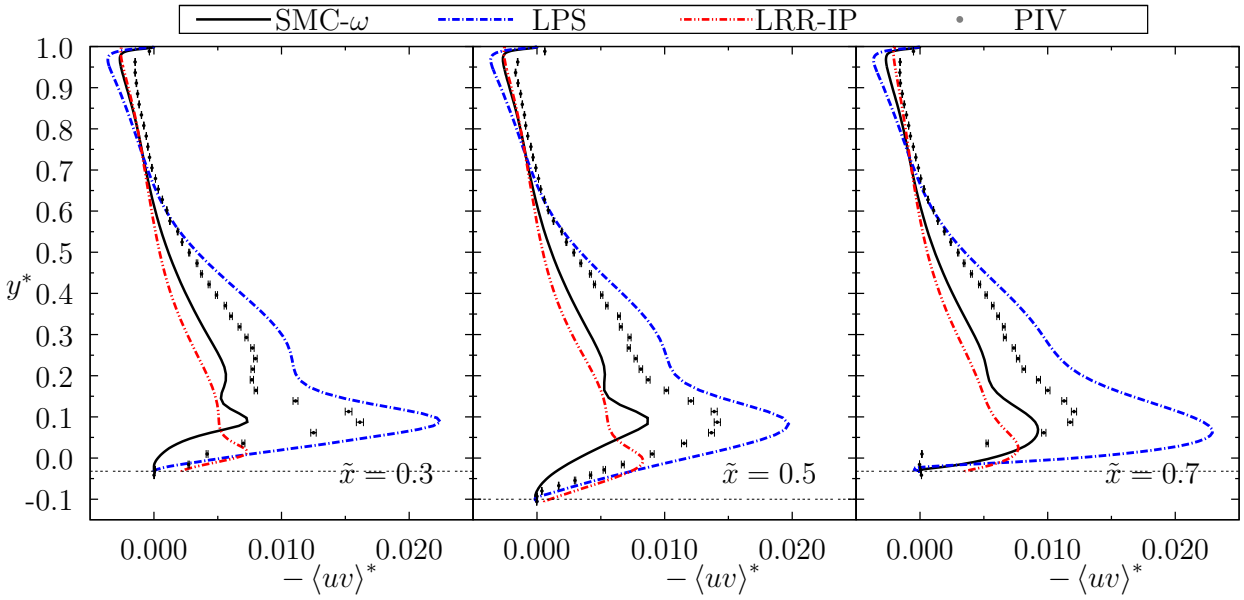

Figure 5.14: SMC models: Dimensionless Reynolds shear stress, $-\langle uv \rangle^*$, distributions at $\mathrm{Re_b} = 10700$ for Wave 9 at $\tilde{x} = 0.3$, 0.5, and 0.7.

Table 5.4: $\mathrm{RMS}_{\mathrm{RN},-\langle uv\rangle^*}$ [%] values comparing numerical to experimental data, for the entire profile and to a near-wall region.

Model	Entire Height			Near-Wall		
	Location ($\tilde{x}$)			Location ($\tilde{x}$)		
	0.3	0.5	0.7	0.3	0.5	0.7
LRR-IP	20.3	22.0	23.6	34.7	30.1	42.0
LPS	12.0	9.5	28.0	22.0	13.8	68.6
SMC-ω	14.5	13.1	17.6	26.5	18.5	40.0

5.5 Summary: Numerical Results

The numerical results are summarized in Table 2.2. The mean velocity and recirculation region are analyzed in Section 5.1, and it established the overall view of the flow predictions over the wavy geometry. The first order statistics ($\langle U\rangle^*$ and $\langle V\rangle^*$) were thoroughly discussed for the flow development and fully periodic regions. They provided great insights on the mean velocity quantities characteristics and the influence of the recirculation region and the shear layer region in these numerical mean quantities. The wall shear stress, τ_w^*, results shown how the separation and reattachment locations were determined for the numerical models, and their comparison to previous experiments and numerical studies. The three Reynolds stresses ($\langle u^2\rangle^*$, $\langle v^2\rangle^*$, and $-\langle uv\rangle^*$) were presented and discussed in Section 5.4; they provided great insights in the turbulence field predictions allowing a further understanding of the weakness of the SMC models to properly reproduce the correct Reynolds stresses levels.

Table 5.5: Experimental studies summary: turbulent flow over a wavy channel.

Method	Flow Quantities Studied
k–ϵ, R-k–ϵ, k–ω, SST, LPS, LRR-IP, and SMC-ω	$\langle U\rangle^*$, $\langle V\rangle^*$, τ_w^*, $\langle u^2\rangle^*$,$\langle v^2\rangle^*$, and $-\langle uv\rangle^*$

Summary and Conclusions

The experimental studies revealed some unique features of the turbulent flow over the wavy bottom wall in a closed channel. For example, the streamwise mean velocity profiles presented an inflection point (i.e., a curve concavity change) because of the presence of the recirculation bubble. The mean velocity and Reynolds stresses exhibited flow inhomogeneity in the x and y directions for all waves. Higher levels of Reynolds stresses were found above the recirculation region. The Reynolds normal stresses distributions are also highly anisotropic, which challenges turbulence models that assume an isotropic condition for the Reynolds normal stresses. The wave shape induced small variations in the outer area of the flow, confirming previous studies findings that the outer turbulence characteristics are independent of turbulence generated at the wall.

The experimental studies were also able to provide useful information about the turbulent flow development along the wavy wall. The statistical quantities revealed a very different flow physics between Wave 1 and other Waves. For example, the recirculation bubble occupied a longer extend over the bottom wall, and it had a higher height at Wave 1. The recirculation decreased in size from wave to wave until reaching the periodic flow condition region (Wave 8), where the recirculation size remained constant. The influence of the differences in the recirculation size could be seen in differences in the mean velocities distributions differences among the waves. For example, there was a stronger reverse flow at Wave 1, a higher streamwise mean velocity magnitude in the lower portion of the channel at Wave 1 (above the recirculation bubble), and a smaller magnitude for the upper part of the channel. The wall-normal mean velocity was larger in magnitude at Wave 1 than in some areas of the channel, which implied a higher momentum transport at Wave 1 compared to Wave 9. Those insights provided a clear and detailed analyses of the flow adjustment along the wavy channel.

The flow physics of the turbulence production was thoroughly investigated in both non-periodic and periodic regions. The results revealed that, due to the unique Reynolds stresses

and velocity gradients distributions, the turbulent kinetic energy production is quite different when compared to the canonical flat wall channel flow. For instance, in a smooth wall channel flow, only the $-\langle uv \rangle \frac{\partial \langle U \rangle}{\partial y}$ term contributes to turbulence production. In the wavy wall channel, on the other hand, the influence of the $-\langle u^2 \rangle \frac{\partial \langle U \rangle}{\partial x}$ and $-\langle uv \rangle \frac{\partial \langle V \rangle}{\partial x}$ terms in the total production, P_k^* are relevant in certain areas. The $-\langle v^2 \rangle \frac{\partial \langle V \rangle}{\partial y}$ and $-\langle u^2 \rangle \frac{\partial \langle U \rangle}{\partial x}$ term switched signs from $\tilde{x} = 0.3$ to 0.7 because of the switch on sign of the velocity gradients in all waves. Important differences are also found in the turbulence production for Wave 1 compared to Wave 9. At Wave 1, the turbulence production was restricted to a smaller portion of the channel and the turbulence production peak value was 33 % higher than Wave 9 at $\tilde{x} = 0.3$. The turbulence production terms contributed differently to the total production at Wave 1 compared to Wave 9. Those are a few examples that demonstrate the complexity of the interplay between the statistical quantities and how they influenced the turbulence production. The turbulence model formulations may be improved by using the information provided here.

The ability of seven turbulence models to predict the recirculation location, streamwise mean velocity, and Reynolds shear stress in turbulent flow over a wavy wall in a horizontal channel was investigated by comparisons with experimental data. The standard k–ϵ and Realizable k–ϵ eddy viscosity models along with the LPS SMC model had the best overall performance. All the eddy viscosity models predicted similar results for the mean velocity and recirculation location. The SMC-ω model was also in good agreement with experimental data for the mean velocity. For the Reynolds stresses, the LPS and SMC-ω models had reasonable predictions in Wave 9 except at $\tilde{x} = 0.7$. The LRR-IP model showed poor predictions, most likely because of its scalable wall function. It was noted that the wall treatment was critically important in the capability of the model to predict the flow separation. The following wall treatments are suitable for this application: the Automatic Wall Treatment in CFX 16.2 and 17.2, and the Enhanced Wall Treatment (EWT) in Fluent 17.2. In addition, there was no notable benefit of the SMC models compared to the eddy viscosity models in

capability of predicting the mean flow and the separation and reattachment locations.

As future work, the following items could be further investigated:

- An improved PIV set-up to measure three-component flow quantities would allow further flow physics studies including the turbulence quantities in the z-direction.
- The numerical and experimental studies could be further expanded to consider a non-isothermal scenario since this type of geometry is mainly associated with heat transfer enhancement applications.
- The study of a more realistic engineering problems such as an industrial plate heat exchanger, where flow separation occurs and structured surfaces were employed in the upper and lower channel walls.
- Investigation of all the terms in the turbulent kinetic energy transport equation to have a more profound understanding of the turbulent transport, which would require an adequate experimental set-up to capture the quantities involved.
- Implement other numerical simulations techniques such as a hybrid RANS-LES, LES, and DNS to explore their capabilities further when dealing with separated turbulent flows.

Overall, the study has fulfilled its objective to provide further physical understanding of isothermal turbulent flow over a wavy wall geometry using mean velocities and higher order statistics obtained using a particle image velocimetry technique, for both periodic and non-periodic regions. It also accomplished the objective to provide a systematic evaluation of two-equation and SMC models performance for future reference for engineers when selecting those models.

References

[1] N. Kruse, S. Kuhn, and P. R. von Rohr, Wavy Wall Effects on Turbulence Production and Large-Scale Modes, *Journal of Turbulence*, vol. 7, pp. N31, 2006.

[2] A. M. Hamed, L. Castillo, and L. P. Chamorro, Turbulent Boundary Layer Response to Large-Scale Wavy Topographies, *Physics of Fluids*, vol. 29, pp. 065113, 2017.

[3] V. De Angelis, P. Lombardi, and S. Banerjee, Direct Numerical Simulation of Turbulent Flow over a Wavy Wall, *Physics of Fluids*, vol. 9, pp. 2429, 1997.

[4] W. K. George, Lectures in Turbulence for the 21st Century, *Chalmers University of Technology*, 2013.

[5] H. Tennekes and J. L. Lumley, *A First Course in Turbulence*, MIT Press, Cambridge, Mass, 1972.

[6] D. S.-K. Ting, Statistical Description of Flow Turbulence, in *Basics of Engineering Turbulence*, pp. 47–68, Elsevier, 2016.

[7] D. Wilcox, *Turbulence Modeling for CFD*, DCW Industries, Incorporated, 1994.

[8] N. D. Sandham, B. E. Launder, and Isaac Newton Institute for Mathematical Sciences, *Closure Strategies for Turbulent and Transitional Flows*, Cambridge University Press, Cambridge, UK, 2002.

[9] S. B. Pope, *Turbulent Flows*, [rev. ed.]. ed., Cambridge, Cambridge, 2005.

[10] A. Dewan, *Tackling Turbulent Flows in Engineering*, Springer Berlin Heidelberg, Berlin, Heidelberg, 2011.

[11] O. Reynolds, On the Dynamical Theory of Incompressible Viscous Fluids and the Determination of the Criterion., *Proceedings of the Royal Society of London*, vol. 56, pp. 40–45, 1894.

[12] B. Launder and D. Spalding, The Numerical Computation of Turbulent Flows, *Computer Methods in Applied Mechanics and Engineering*, vol. 3, pp. 269–289, 1974.

[13] Z. Yang, T.-H. Shih, A. Shabbir, J. Zhu, and W. W. Liou, A New K-Epsilon Eddy Viscosity Model for High Reynolds Number Turbulent Flows: Model Development and Validation - NASA-TM-106721, 1994.

[14] D. Wilcox, Reassessment of the Scale-Determining Equation for Advanced Turbulence Models, *AIAA Journal*, vol. 26, pp. 1299–1310, 1988.

[15] F. R. Menter, Two-Equation Eddy-Viscosity Turbulence Models for Engineering Applications, *AIAA Journal*, vol. 32, pp. 1598–1605, 1994.

[16] ANSYS® Academic Research, Help System, CFX-Solver Theory Manual, ANSYS, Inc., Canonsburg, PA, USA., Release 16.2.

[17] G. Iaccarino, Predictions of a Turbulent Separated Flow Using Commercial CFD Codes, *Journal of Fluids Engineering*, vol. 123, pp. 819, 2001.

[18] B. Launder and B. Sharma, Application of the Energy-Dissipation Model of Turbulence to the Calculation of Flow near a Spinning Disc, *Letters in Heat and Mass Transfer*, vol. 1, pp. 131–137, 1974.

[19] M. Pathak, A. Dewan, and A. K. Dass, Computational Prediction of a Slightly Heated Turbulent Rectangular Jet Discharged into a Narrow Channel Crossflow Using Two Different Turbulence Models, *International Journal of Heat and Mass Transfer*, vol. 49, pp. 3914–3928, 2006.

[20] S. Paul, S. Ormiston, and M. Tachie, Experimental and Numerical Investigation of Turbulent Cross-Flow in a Staggered Tube Bundle, *International Journal of Heat and Fluid Flow*, vol. 29, pp. 387–414, 2008.

[21] B. E. Launder, G. J. Reece, and W. Rodi, Progress in the Development of a Reynolds-Stress Turbulence Closure, *Journal of Fluid Mechanics*, vol. 68, pp. 537–566, 1975.

[22] D. P. Zilker, G. W. Cook, and T. J. Hanratty, Influence of the Amplitude of a Solid Wavy Wall on a Turbulent Flow. Part 1. Non-Separated Flows, *Journal of Fluid Mechanics*, vol. 82, pp. 29–51, 1977.

[23] D. P. Zilker and T. J. Hanratty, Influence of the Amplitude of a Solid Wavy Wall on a Turbulent Flow. Part 2. Separated Flows, *Journal of Fluid Mechanics*, vol. 90, pp. 257–271, 1979.

[24] J. D. Kuzan, T. J. Hanratty, and R. J. Adrian, Turbulent Flows with Incipient Separation over Solid Waves, *Experiments in fluids*, vol. 7, pp. 88–98, 1989.

[25] J. Buckles, T. J. Hanratty, and R. J. Adrian, Turbulent Flow over Large-Amplitude Wavy Surfaces, *Journal of Fluid Mechanics*, vol. 140, pp. 27–44, 1984.

[26] J. D. Hudson, L. Dykhno, and T. J. Hanratty, Turbulence Production in Flow over a Wavy Wall, *Experiments in Fluids*, vol. 20, pp. 257–265, 1996.

[27] N. Kruse, A. Gunther, and P. R. von Rohr, Dynamics of Large-Scale Structures in Turbulent Flow over a Wavy Wall, *Journal of Fluid Mechanics*, vol. 485, pp. 87–96, 2003.

[28] A. Günther and P. R. von Rohr, Large-Scale Structures in a Developed Flow over a Wavy Wall, *Journal of Fluid Mechanics*, vol. 478, 2003.

[29] N. Kruse and P. Rudolf von Rohr, Structure of Turbulent Heat Flux in a Flow over a Heated Wavy Wall, *International Journal of Heat and Mass Transfer*, vol. 49, pp. 3514–3529, 2006.

[30] C. Wagner, S. Kuhn, and P. Rudolf von Rohr, Scalar Transport from a Point Source in Flows over Wavy Walls, *Experiments in Fluids*, vol. 43, pp. 261–271, 2007.

[31] A. M. Hamed, A. Kamdar, L. Castillo, and L. P. Chamorro, Turbulent Boundary Layer over 2D and 3D Large-Scale Wavy Walls, *Physics of Fluids*, vol. 27, pp. 106601, Oct. 2015.

[32] C. Maass and U. Schumann, Numerical Simulation of Turbulent Flow over a Wavy Boundary, *Direct and Large-Eddy Simulation I*, pp. 287–297, 1994.

[33] C. Maass and U. Schumann, Direct Numerical Simulation of Separated Turbulent Flow over a Wavy Boundary, *Flow Simulation with High-Performance Computers II*, pp. 227–241, 1996.

[34] P. Cherukat, Y. Na, T. J. Hanratty, and J. B. McLaughlin, Direct Numerical Simulation of a Fully Developed Turbulent Flow over a Wavy Wall, *Theoretical and computational fluid dynamics*, vol. 11, pp. 109–134, 1998.

[35] H. Yoon, O. El-Samni, A. Huynh, H. Chun, H. Kim, A. Pham, and I. Park, Effect of Wave Amplitude on Turbulent Flow in a Wavy Channel by Direct Numerical Simulation, *Ocean Engineering*, vol. 36, pp. 697–707, 2009.

[36] V. Patel, J. Chon, and J. Yoon, Turbulent-Flow in a Channel with a Wavy Wall, *Journal of Fluid Engineering-Transactions of the ASME*, vol. 113, 1991.

[37] D. S. Henn and R. I. Sykes, Large-Eddy Simulation of Flow over Wavy Surfaces, *Journal of Fluid Mechanics*, vol. 383, pp. 75–112, 1999.

[38] J. Cui, V. C. Patel, and C.-L. Lin, Prediction of Turbulent Flow Over Rough Surfaces Using a Force Field in Large Eddy Simulation, *Journal of Fluids Engineering*, vol. 125, pp. 2, 2003.

[39] A. Z. Dellil, A. Azzi, and B. A. Jubran, Turbulent Flow and Convective Heat Transfer in a Wavy Wall Channel, *Heat and Mass Transfer*, vol. 40, pp. 793–799, 2004.

[40] C. Wagner, S. Kenjereš, and P. R. von Rohr, Dynamic Large Eddy Simulations of Momentum and Wall Heat Transfer in Forced Convection over Wavy Surfaces, *Journal of Turbulence*, vol. 12, pp. N7, 2011.

[41] S. Knotek and M. Jícha, Simulation of Flow over a Wavy Solid Surface: Comparison of Turbulence Models, *EPJ Web of Conferences*, vol. 25, p. 01040, EDP Sciences, 2012.

[42] C. Khaled, N. Driss, and S. C. Nouredine, CFD Simulation of Turbulent Flow and Heat Transfer Over Rough Surfaces, *Energy Procedia*, vol. 74, pp. 909–918, 2015.

[43] V. Martins Segunda, S. Ormiston, and M. Tachie, Numerical Analysis of Turbulent Flow Over a Wavy Wall in a Channel, p. V01AT03A014, 2016.

[44] M. Raffel (ed.), *Particle Image Velocimetry: A Practical Guide*, 2nd ed., Springer, Heidelberg ; New York, 2007.

[45] A. K. Prasad, R. J. Adrian, C. C. Landreth, and P. W. Offutt, Effect of Resolution on the Speed and Accuracy of Particle Image Velocimetry Interrogation, *Experiments in Fluids*, vol. 13, pp. 105–116, 1992.

[46] D. J. Forliti, P. J. Strykowski, and K. Debatin, Bias and Precision Errors of Digital Particle Image Velocimetry, *Experiments in Fluids*, vol. 28, pp. 436–447, 2000.

[47] Julius S. Bendat and A. G. Piersol, *Random Data: Analysis and Measurement Procedures*, 4th ed., Wiley series in probability and statistics, Wiley, Hoboken, NJ, 2010.

[48] ANSYS® Academic Research, Help System, Fluent-Solver Theory Manual,ANSYS, Inc., Canonsburg, PA, USA, Release 17.2.

[49] M. Shah, M. Agelinchaab, and M. Tachie, Influence of PIV Interrogation Area on Turbulent Statistics up to 4th Order Moments in Smooth and Rough Wall Turbulent Flows, *Experimental Thermal and Fluid Science*, vol. 32, pp. 725–747, 2008.

[50] T.-H. Shih, W. W. Liou, A. Shabbir, Z. Yang, and J. Zhu, A New K-ϵ Eddy Viscosity Model for High Reynolds Number Turbulent Flows, *Computers & Fluids*, vol. 24, pp. 227–238, 1995.

[51] B. E. Launder and N. Shima, Second-Moment Closure for the near-Wall Sublayer - Development and Application, *AIAA Journal*, vol. 27, pp. 1319–1325, 1989.

[52] M. Wolfshtein, The Velocity and Temperature Distribution in One-Dimensional Flow with Turbulence Augmentation and Pressure Gradient, *International Journal of Heat and Mass Transfer*, vol. 12, pp. 301–318, 1969.

[53] H. C. Chen and V. C. Patel, Near-Wall Turbulence Models for Complex Flows Including Separation, *AIAA Journal*, vol. 26, pp. 641–648, 1988.

[54] R. D. Moser, J. Kim, and N. N. Mansour, Direct Numerical Simulation of Turbulent Channel Flow up to Re[Sub τ]=590, *Physics of Fluids*, vol. 11, pp. 943, 1999.

[55] R. B. Dean, Reynolds Number Dependence of Skin Friction and Other Bulk Flow Variables in Two-Dimensional Rectangular Duct Flow, *Journal of Fluids Engineering*, vol. 100, pp. 215–223, 1978.

[56] N. T. Basse, Turbulence Intensity and the Friction Factor for Smooth- and Rough-Wall Pipe Flow, *Fluids*, vol. 2, pp. 30, 2017.

[57] Zhang Hui-Qiang and Lu Hao and Wang Bing and Wang Xi-Lin, Experimental Investigation of Flow Drag and Turbulence Intensity of a Channel Flow with Rough Walls, *Chinese Physics Letters*, vol. 28, pp. 084703, 2011.

Appendix A

Experimental Data Convergence Test

A.1 Sample size

The adequacy of the sample size used to compute the turbulent flow mean and higher order statistics was evaluated. A set of 7500 image pairs was acquired, and then sample sizes of N = 2000, 4000, 6000 and 7500 were used to calculate the mean velocity, the Reynolds stresses, and the triple correlations. Those image pairs used an IA size of 32×32 pixels with 50% overlap. A qualitative study of the dimensionless profiles of those quantities at $\tilde{x} = 0.5$ along Wave 9 is presented in Figures A.1, A.2, and A.3.

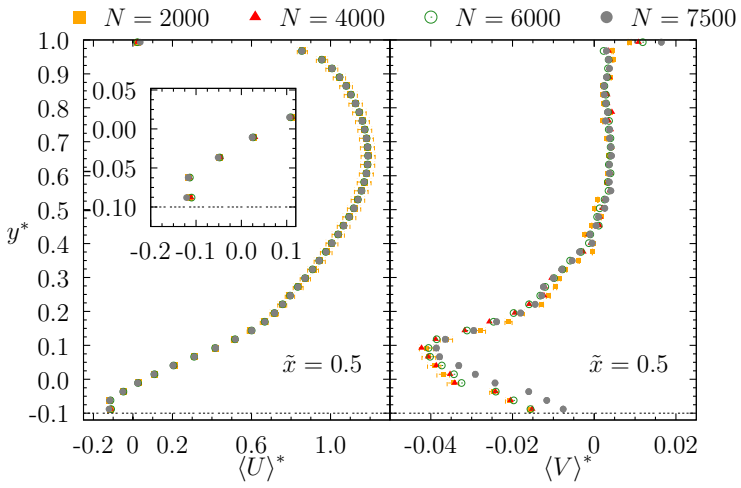

Figure A.1: Results for samples sizes of $N = 2000, 4000, 6000$, and 7500 for the profiles of dimensionless streamwise mean velocity, $\langle U \rangle^*$, and wall normal mean velocity, $\langle V \rangle^*$, at Wave 9 and $\tilde{x} = 0.5$, at $\mathrm{Re_b} = 10700$.

The dimensionless streamwise mean velocity, $\langle U \rangle^*$, profiles collapsed well within experimental uncertainty for all values of N in Figure A.1. The dimensionless wall normal mean velocity for all values of N collapsed well within experimental uncertainty, except for a small

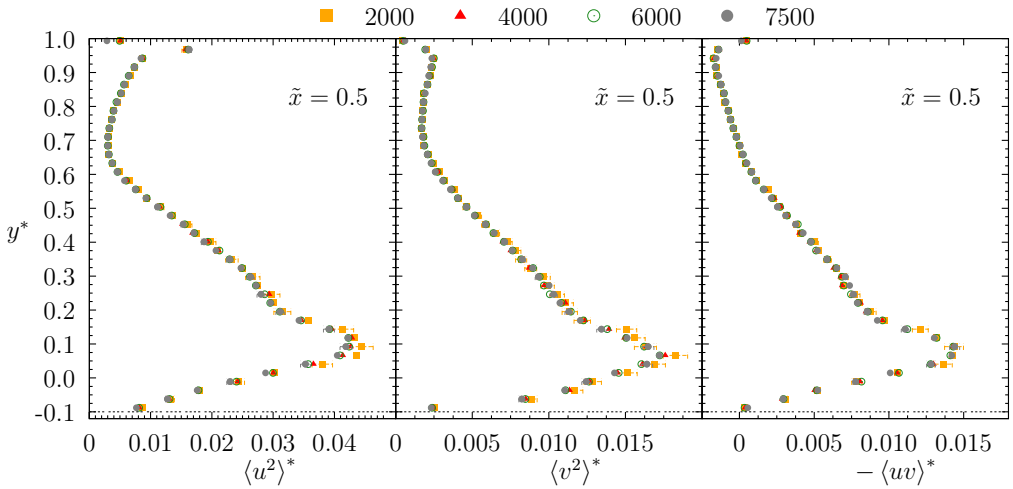

Figure A.2: Results for samples sizes of $N = 2000, 4000, 6000$, and 7500 for profiles of dimensionless Reynolds normal stresses in the streamwise direction, $\langle u^2 \rangle^*$, wall-normal direction, $\langle v^2 \rangle^*$, and the Reynolds shear stress, $-\langle uv \rangle^*$, at Wave 9 and $\tilde{x} = 0.5$, at $\mathrm{Re_b} = 10700$.

region below $y^* < 0.05$ where the results for $N = 7500$ yields lower $\langle V \rangle^*$ compared to the other sample sizes in Figure A.1. It indicates that the mean velocities are independent of the sample size for $N > 2000$.

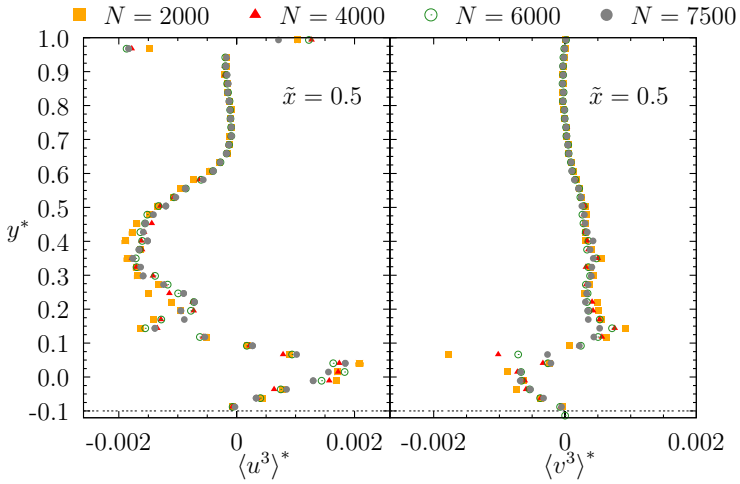

Figure A.3: Results for samples sizes of $N = 2000, 4000, 6000$, and 7500 for the profiles of dimensionless triple correlations in the streamwise, $\langle u^3 \rangle^*$, and wall normal, $\langle v^3 \rangle^*$ directions, at Wave 9 and $\tilde{x} = 0.5$, at $\mathrm{Re_b} = 10700$.

The profiles of dimensionless Reynolds normal stresses in the streamwise direction, $\langle u^2 \rangle^*$, wall-normal direction, $\langle v^2 \rangle^*$, and the Reynolds shear stress, $-\langle uv \rangle^*$, collapsed well within experimental uncertainty for all values of N in Figure A.2. Figure A.3 results for the triple velocity correlations $\langle u^3 \rangle^*$ and $\langle v^3 \rangle^*$ shown good agreement within all sample sizes, except to three scattered $\langle v^3 \rangle^*$ data points at y^*=0.075.

A sample size of $N = 2000$ was selected to analyze the inlet conditions, and the flow development studies at Waves 1, 3, 6 and 8 to reduce data acquisition time. The results in the fully periodic region at Wave 9 used $N = 7500$ to reduce the data uncertainty. Note that a 2000 sample size would be sufficient to evaluate the presented statistics and it is within the range of sample size commonly used in the PIV literature.

A.2 Interrogation Area (IA)

The PIV interrogation area has an influence on turbulent statistics as presented by Shah *et al.* [49] for smooth and rough wall turbulent flows. It is important to establish the influence of the interrogation size in the current results. For that reason, this study investigated five IA sizes from 16 pixels to 64 pixels, where the velocity vectors spacing varied from 0.19 mm to 0.77 mm, with an overlap of 50% for all IA sizes. The sample size of $N = 7500$ was considered for this investigation. A quantitative study of the dimensionless profiles of the turbulence statistics at $\tilde{x} = 0.5$ along Wave 9 is presented in Figures A.4, A.5, and A.6.

The dimensionless streamwise mean velocity, $\langle U \rangle^*$, collapsed for all IA sizes in Figure A.4. The wall normal mean velocity, $\langle V \rangle^*$, had overall good agreement within all IA sizes, except for a region below $y^* < 0.1$ where the results for 32×32 yields lower $\langle V \rangle^*$ compared to the other IA sizes in Figure A.4. The different IA results for the profiles of dimensionless Reynolds normal stresses in the streamwise direction, $\langle u^2 \rangle^*$, wall-normal direction, $\langle v^2 \rangle^*$, and

the Reynolds shear stress, $-\langle uv \rangle^*$, are very similar among them. The 16×16 IA size was the only result that has slightly diffrent from other IA sizes. It is seen that the 32×32 has demonstrated to be adequate because it compared well with other IA sizes profiles within the experimental uncertainty.

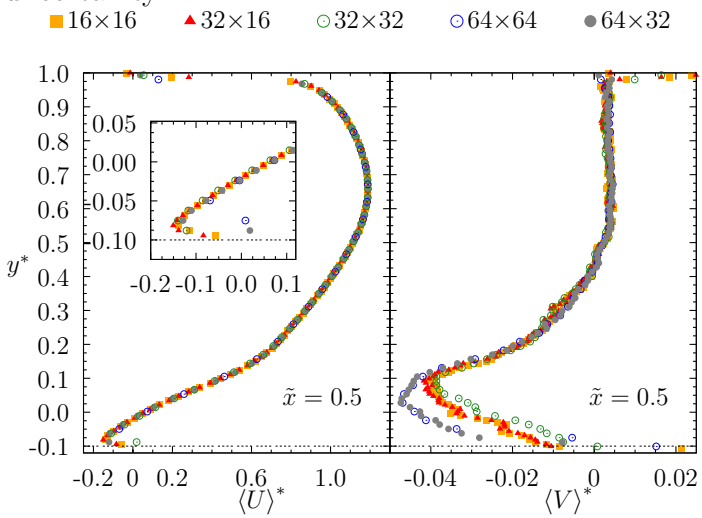

Figure A.4: Results for IA sizes of 16×16, 32×16, 32×32, 64×32, and 64×64 for the profiles of dimensionless streamwise mean velocity, $\langle U \rangle^*$, and wall normal mean velocity, $\langle V \rangle^*$, at Wave 9 and $\tilde{x} = 0.5$, at $\mathrm{Re_b} = 10700$.

The triple correlations $\langle u^3 \rangle^*$ and $\langle v^3 \rangle^*$ are comparable and within the uncertainty for all IA sizes. The 16×16 presented slight more scattering than other IA sizes, most likely because the IA was to small and the experimental set-up was not adequate for such small IA size. It was found that the 32×32 IA size with 50% overlap was adequate for these experimental conditions, since it compared well to other IA sizes results presented. This represents an IA of $l_x = 0.39$ mm and $l_y = 0.39$ mm, representing a spacing between adjacent vectors of about $l = 0.025h$ in both the x and y directions.

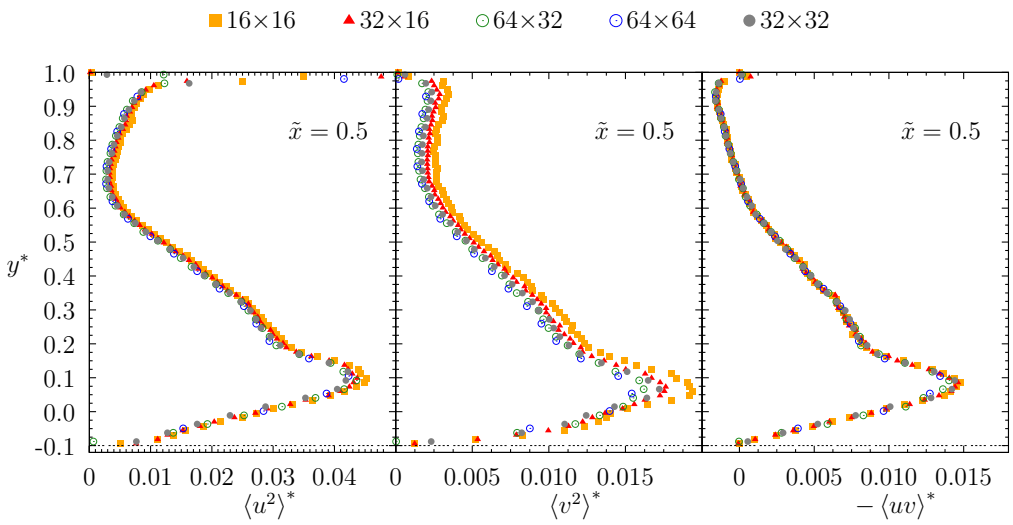

Figure A.5: Results for IA sizes of 16×16, 32×16, 32×32, 64×32, and 64×64 for profiles of dimensionless Reynolds normal stresses in the streamwise direction, $\langle u^2 \rangle^*$, wall-normal direction, $\langle v^2 \rangle^*$, and the Reynolds shear stress, $-\langle uv \rangle^*$, at Wave 9 and $\tilde{x} = 0.5$, at $\mathrm{Re_b} = 10700$.

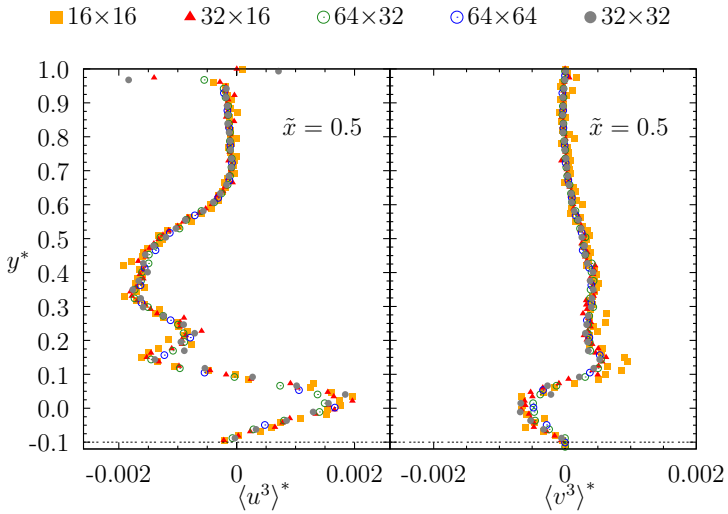

Figure A.6: Results for IA sizes of 16×16, 32×16, 32×32, 64×32, and 64×64 for the profiles of dimensionless triple correlations in the streamwise, $\langle u^3 \rangle^*$, and wall normal, $\langle v^3 \rangle^*$ directions, at Wave 9 and $\tilde{x} = 0.5$, at $\mathrm{Re_b} = 10700$.

Appendix B

Reynolds Averaged Navier Stokes (RANS) Models

The equations for the continuity (mass conservation) and the conservation of momentum are presented in Equation 2.2 and 2.3, respectively. As mentioned in Section 2.1, the last term in Equation 2.3 ($\langle u_i u_j \rangle$) is called the Reynolds stress. Because of the Reynolds stresses, there are ten unknowns compared to the four equations when considering the RANS equations (Eq. 2.3). It is therefore necessary to close the RANS equations to implement them in a RANS CFD simulation. The approach to calculating the Reynolds stress is the main difference between the so-called eddy viscosity models and the Second-Moment Closure (SMC) models. The first use the Boussinesq approximation to close the momentum Equation 2.3. The SMC models solve a transport equation for each of the six components of the symmetric Reynolds stress tensor. The equations and formulations are presented in the next section were mainly obtained from [16,48]. They are presented here in Cartesian coordinates using Einstein summation convention. They are in steady-state form and for isothermal, incompressible flow, and without buoyancy forces. The equations also do not consider any user-defined source terms. The current study applies a range of eddy viscosity and SMC turbulence models as outlined in the Section 3.2.3. A detailed description of the turbulence models are presented first followed by the near-wall treatment in this Appendix.

B.1 Two-Equation Eddy Viscosity Models

Two-equation turbulence models are an example of eddy viscosity models. The two-equation turbulence models used in this work are the following: k-ϵ [12], Realizable k-ϵ [13], k-ω [14], and SST [15]. These models will be referred hereafter as k–ϵ, R-k–ϵ, k–ω, and SST,

respectively. The Reynolds stress term $-\rho \langle u_i u_j \rangle$ can be modelled as follow:

$$-\rho \langle u_i u_j \rangle = \mu_t \left(\frac{\partial \langle U_i \rangle}{\partial x_j} + \frac{\partial \langle U_j \rangle}{\partial x_i} \right) - \frac{2}{3} \delta_{ij} (\rho k) \tag{B.1}$$

where μ_t is the turbulence eddy viscosity, k is the turbulent kinetic energy, δ_{ij} is the Kronecker delta. The mean flow conservation of momentum equation (Eq. 2.3) can now be written in terms of the eddy viscosity μ_t, as follow:

$$\rho \langle U \rangle_j \frac{\partial \langle U \rangle_i}{\partial x_j} = -\frac{\partial \langle P' \rangle}{\partial x_i} + \frac{\partial}{\partial x_j} \left[(\mu + \mu_t) \left(\frac{\partial \langle U_i \rangle}{\partial x_j} \right) \right] \tag{B.2}$$

where the first term on the right-hand side equation($\langle P' \rangle$) is the modified pressure, which is defined as follow:

$$\langle P' \rangle = \langle P \rangle + \frac{2}{3} \rho k \tag{B.3}$$

B.1.1 The k–ϵ model

The model proposed by Launder and Spalding [12] is used for the k–ϵ model in ANSYS Fluent and CFX. This model solves transport equations for the turbulent kinetic energy (k) in Equation (B.4), and the turbulence eddy dissipation (ϵ) in Equation (B.5).

$$\rho \frac{\partial (\langle U_j \rangle k)}{\partial x_j} = \frac{\partial}{\partial x_j} \left[(\mu + \frac{\mu_t}{\sigma_k}) \left(\frac{\partial k}{\partial x_j} \right) \right] + P_k - \rho \epsilon \tag{B.4}$$

$$\rho \frac{\partial (\langle U_j \rangle \epsilon)}{\partial x_j} = \frac{\partial}{\partial x_j} \left[(\mu + \frac{\mu_t}{\sigma_\epsilon}) \left(\frac{\partial \epsilon}{\partial x_j} \right) \right] + \frac{\epsilon}{k} \left(C_{\epsilon 1} P_k - C_{\epsilon 2} \rho \epsilon \right) \tag{B.5}$$

The k-ϵ model constants are σ_k=1.0, σ_ϵ=1.3 ,$C_{\epsilon 1}$=1.44, and $C_{\epsilon 2}$=1.92. By solving those two equations (B.4 and B.5), the eddy viscosity term in the momentum equation (B.2) is determined by the following Equation B.6, where C_μ is equal to 0.09.

$$\mu_t = C_\mu \rho \frac{k^2}{\epsilon} \tag{B.6}$$

B.1.2 The Realizable k–ϵ model

Realizable k–ϵ model (R-k–ϵ) was developed by Shih *et al.* [50]. This model used in ANSYS Fluent (release 17.2) solves two equations: the turbulent kinetic energy (k), which has the same formulation and constants as in the previous Equation B.4, and the turbulent dissipation (ϵ) that now it is defined in Equation B.7.

$$\rho\frac{\partial(\langle U_j\rangle\,\epsilon)}{\partial x_j} = \frac{\partial}{\partial x_j}\left[(\mu+\frac{\mu_t}{\sigma_\epsilon})\left(\frac{\partial\epsilon}{\partial x_j}\right)\right] - \rho C_{\epsilon 2}\frac{\epsilon^2}{k+\sqrt{\nu\epsilon}} \tag{B.7}$$

where the constants are the σ_ϵ=1.2, and $C_{\epsilon 2}$=1.90. By solving those two equations, the eddy viscosity in the momentum equation (Eq. B.2) is determined by Equation B.6. In this model, the C_μ value is defined by Equation B.8 [48].

$$C_\mu = \frac{1}{A_0 + A_s\frac{kU^*}{\epsilon}} \tag{B.8}$$

where, U^* is defined as :

$$U^* = \sqrt{S_{ij}S_{ij} + \tilde{\Omega}_{ij}\tilde{\Omega}_{ij}} \tag{B.9}$$

where, S_{ij} is the mean strain rate tensor defined as:

$$S_{ij} = \frac{1}{2}\left(\frac{\partial\langle U_i\rangle}{\partial x_j} + \frac{\partial\langle U_j\rangle}{\partial x_i}\right) \tag{B.10}$$

and

$$\tilde{\Omega}_{ij} = \Omega_{ij} - 2\epsilon_{ijk}\omega_k \tag{B.11}$$

with

$$\Omega_{ij} = \langle\Omega\rangle_{ij} - 2\epsilon_{ijk}\omega_k \tag{B.12}$$

where $\langle\Omega\rangle_{ij}$ is the mean rate-of-rotation tensor defined as:

$$\langle\Omega_{ij}\rangle = \frac{1}{2}\left(\frac{\partial\langle U_i\rangle}{\partial x_j} - \frac{\partial\langle U_j\rangle}{\partial x_i}\right) \tag{B.13}$$

The model constants are the A_0 =4.04 and $A_s = \sqrt{6}\,cos\phi$, where

$$\phi = \frac{1}{3}cos^{-1}\left(\sqrt{6}W\right), W = \frac{S_{ij}S_{jk}S_{ki}}{S_{ij}S_{ij}^{3/2}} \tag{B.14}$$

Note that the eddy viscosity is still a function of k and ϵ, but in this case C_μ takes into consideration the mean strain and the rotation rates (angular velocity if the system has a rotation).

B.1.3 The k–ω model

The k–ω model solves a slightly different formulation for the turbulent kinetic energy, k, and a transport equation for turbulent frequency, ω. The set of equations are presented in Equations B.15 and B.16, respectively for k and ω.

$$\rho\frac{\partial(\langle U_j\rangle\, k)}{\partial x_j} = \frac{\partial}{\partial x_j}\left[(\mu + \frac{\mu_t}{\sigma_k})\left(\frac{\partial k}{\partial x_j}\right)\right] + P_k - \rho\beta' k\omega \tag{B.15}$$

$$\rho\frac{\partial(\langle U_j\rangle\, \omega)}{\partial x_j} = \frac{\partial}{\partial x_j}\left[(\mu + \frac{\mu_t}{\sigma_\omega})\left(\frac{\partial \omega}{\partial x_j}\right)\right] + \alpha\frac{\omega}{k}P_k - \rho\beta\omega^2 \tag{B.16}$$

where P_k is the production term defined as:

$$P_k = \mu_t\left(\frac{\partial\langle U_i\rangle}{\partial x_j} + \frac{\partial\langle U_j\rangle}{\partial x_i}\right)\frac{\partial\langle U_i\rangle}{\partial x_j} \tag{B.17}$$

and the eddy viscosity is computed as:

$$\mu_t = \rho\frac{k}{\omega} \tag{B.18}$$

The k-ω model constants used are: σ_k= 2, β'=0.09, σ_ω= 2, α=5/9, and β=0.075.

B.1.4 The SST model

The SST model is significantly different than the previous models, k–ϵ, R-k–ϵ, and k–ω. It uses a blending function that allows the model to use the k-ϵ model in the outer part of the boundary layer (in the free stream) and the k-ω model in the near the wall region. The model was developed by Menter [15] and its formulation in Equation B.19 and B.20 are based on [16].

$$\rho\frac{\partial(\langle U_j\rangle\, k)}{\partial x_j} = \frac{\partial}{\partial x_j}\left[(\mu + \frac{\mu_t}{\sigma_{k3}})\left(\frac{\partial k}{\partial x_j}\right)\right] + P_k - \rho\beta' k\omega \tag{B.19}$$

$$\rho\frac{\partial(\langle U_j\rangle\,\omega)}{\partial x_j} = \frac{\partial}{\partial x_j}\left[(\mu+\frac{\mu_t}{\sigma_{\omega 3}})\left(\frac{\partial\omega}{\partial x_j}\right)\right] + (1-F_1)2\rho\frac{1}{\sigma_{\omega 2}\omega}\frac{\partial k}{\partial x_j}\frac{\partial\omega}{\partial x_j} + \alpha_3\frac{\omega}{k}P_k - \rho\beta_3\omega^2 \quad \text{(B.20)}$$

P_k is the production term defined in Equation B.17, F_1 is the blending function defined in Equation B.22, and the constants σ_{k3}, $\sigma_{\omega 3}$, α_3, and β_3 are calculated from Equation B.21.

$$\phi_3 = F_1\phi_1 + (1-F_1)\phi_2 \quad \text{(B.21)}$$

where the constants of set 1 (ϕ_1) are the k-ω model constants σ_{k1}= 2.0, β_1'=0.09, $\sigma_{\omega 1}$= 2.0, α_1=5/9, and β_1=0.075. The constants of set 2 (ϕ_2) are the k-ϵ model constants σ_{k2}= 1.0, β_2'=0.09, $\sigma_{\epsilon 2}$= 1.3, α_1=1.44, and β_1=0.0828. The blending function F_1 is:

$$F_1 = \tanh(arg_1^4) \quad \text{(B.22)}$$

where arg_1 is defined in Equation B.23 with y defined as the distance to the closest wall.

$$arg_1 = \min\left(\max\left(\frac{\sqrt{k}}{\beta_1'\omega y}, \frac{500\nu}{y^2\omega}\right), \frac{4\rho k}{CD_{kw}\sigma_{\omega 2}y^2}\right) \quad \text{(B.23)}$$

$$CD_{k\omega} = \max\left(2\rho\frac{1}{\sigma_{\omega 2}\omega}\frac{\partial k}{\partial x_j}\frac{\partial\omega}{\partial x_j}, 1\times 10^{-10}\right) \quad \text{(B.24)}$$

The SST model redefines the eddy-viscosity by Equation B.25 using a second blending function F_2, which has the function to better predict the eddy viscosity value in adverse pressure gradient regions and to use Equation B.18 for other parts of the flow [15].

$$\mu_t = \frac{a_1 k\rho}{\max(a_1\omega, SF_2)} \quad \text{(B.25)}$$

The blending function F_2 and arg_2 are defined in Equation B.26 and B.27, respectively.

$$F_2 = \tanh(arg_2^2) \quad \text{(B.26)}$$

$$arg_2 = \max\left(\frac{2\sqrt{k}}{\beta_1'\omega y}, \frac{500\nu}{y^2\omega}\right) \quad \text{(B.27)}$$

B.2 Second Moment Closure (SMC) models

Second Moment Closure (SMC) models solves the original RANS momentum equation (Equation 2.3). The SMC models solve a differential transport equation for each of the six Reynolds stress components, $\langle u_i u_j \rangle$, based on Equation 2.4. The SMC models assume two forms depending on the additional transport equation that is solved. The Reynolds stress equations and the additional transport equation for each of the SMC models used in this study are presented in the next sections.

B.2.1 The LRR-IP model

The LRR-IP model formulations developed by Launder *et al.* [21] are presented here. The Reynolds stress Equation B.28 serve as the initial equation to derive the modelled Reynolds stress equations used by the LRR-IP model. The treatment of each term in the Equation B.28 that is particular to the LRR-IP model is discussed below.

$$\underbrace{\rho \langle U \rangle_k \frac{\partial \langle u_i u_j \rangle}{\partial x_k}}_{C_{ij}} = \overbrace{\left\langle p \left[\frac{\partial u_i}{\partial x_j} + \frac{\partial u_j}{\partial x_i} \right] \right\rangle}^{\phi_{ij}} \underbrace{-\rho \left[\langle u_i u_k \rangle \frac{\partial u_j}{\partial x_k} + \langle u_j u_k \rangle \frac{\partial u_i}{\partial x_k} \right]}_{P_{ij}}$$
$$\underbrace{-\frac{\partial}{\partial x_k} \{ \langle p u_j \rangle \delta_{ik} + \langle p u_i \rangle \delta_{jk} \}}_{D^p_{ij}} \underbrace{-\frac{\partial}{\partial x_k} \{ \rho \langle u_i u_j u_k \rangle \}}_{D^t_{ij}} \underbrace{-\frac{\partial}{\partial x_k} \{ \mu \frac{\partial \langle u_i u_j \rangle}{\partial x_k} \}}_{D^\mu_{ij}} \tag{B.28}$$
$$\underbrace{-2\mu \left[\left\langle \frac{\partial u_i}{\partial x_k} \frac{\partial u_j}{\partial x_k} \right\rangle \right]}_{\epsilon_{ij}}$$

The individual terms identified in Equation B.28 are summarized divided into terms that do not require any modelling (I) and terms that need to be modelled (II), as follows:

I: Terms that do not require modelling

- C_{ij} represents the rate of change of Reynolds stresses due to convection by the mean flow, referred here as the convection term.

- P_{ij} represents the production of stresses by extracting energy from the mean flow, referred as the production term for the Reynolds stresses.

- D^{μ}_{ij} represents the diffusion of Reynolds stresses within the flow field by viscosity, referred as the molecular diffusion term.

II: Terms that require modelling

- ϕ_{ij} represents a pressure velocity gradient tensor responsible for the redistribution of energy among the Reynolds stresses, referred here as the pressure-strain rate term. An empirical function developed by Launder *et al.* [21] is used instead. The pressure strain is modelled via the Isotropization of Production (IP), as follow:

$$\phi_{ij} = \overbrace{-C_1\rho\frac{\epsilon}{k}(\langle u_i u_j\rangle - \frac{2}{3}\delta_{ij}k)}^{\phi_{ij,1}}\overbrace{-C_2(P_{ij} - \frac{2}{3}\delta_{ij}P)}^{\phi_{ij,2}} \tag{B.29}$$

  where C_1=1.8, C_2=0.6, and $P = 0.5\ P_{ii}$.

- D^{p}_{ij} represents the pressure diffusion of Reynolds stresses, referred as the pressure diffusion term, this term has not been modelled or calculated. The term is neglected by the model as usual practice by other authors in SMC modelling [21].

- D^{t}_{ij} represents the turbulent diffusion of Reynolds stresses by velocity fluctuations, referred as the turbulent diffusion term. It is modelled by the generalized gradient diffusion model:

$$D^{t}_{ij} = C_s\rho\frac{\partial}{\partial x_k}\left(\frac{k^2}{\epsilon}\frac{\partial\langle u_i u_j\rangle}{\partial x_k}\right) \tag{B.30}$$

- ϵ_{ij} represents the dissipation of turbulent kinetic energy due to viscous stresses, referred as the dissipation term. The formulation used in the LRR-IP model assumes local isotropy within the small scale structures and high Reynolds numbers, which yields:

$$\epsilon_{ij} = -\frac{2}{3}\rho\epsilon\delta_{ij} \tag{B.31}$$

ANSYS CFX solves Equation B.32 for the Reynolds stresses, taking in account the earlier models presented. Details of the model can be seen in [8, 16, 21]. Those terms were approximated by empirical functions of the mean velocities, Reynolds stresses, and their derivatives.

$$\underbrace{\rho \left\langle U \right\rangle_k \frac{\partial \left\langle u_i u_j \right\rangle}{\partial x_k}}_{C_{ij}} = \overbrace{-C_1\rho\frac{\epsilon}{k}(\langle u_i u_j\rangle - \frac{2}{3}\delta_{ij}k) - C_2(P_{ij} - \frac{2}{3}\delta_{ij}P)}^{\phi_{ij}}$$
$$\underbrace{-\rho\left[\langle u_i u_k\rangle \frac{\partial u_j}{\partial x_k} + \langle u_j u_k\rangle \frac{\partial u_i}{\partial x_k}\right]}_{P_{ij}} \underbrace{+\frac{2}{3}C_s\rho\frac{\partial}{\partial x_k}\left[\frac{k^2}{\epsilon}\frac{\partial\overline{u_i u_j}}{\partial x_k}\right]}_{D^t_{ij}} \underbrace{+\frac{\partial}{\partial x_k}\left[\mu\frac{\partial\overline{u_i u_j}}{\partial x_k}\right]}_{D^\mu_{ij}} \overbrace{-\frac{2}{3}\rho\epsilon\delta_{ij}}^{\epsilon_{ij}} \tag{B.32}$$

It is seen that the model requires an equation for the dissipation, ϵ, to close the Reynolds stress equation. The ϵ-equation in the LRR-IP model in ANSYS CFX (release 16.2) [16] is as follows:

$$\rho\frac{\partial(\langle U_k\rangle\,\epsilon)}{\partial x_k} = \frac{\partial}{\partial x_k}\left[(\mu + \frac{\mu_t}{\sigma_{\epsilon RS}})\left(\frac{\partial\epsilon}{\partial x_k}\right)\right] + \frac{\epsilon}{k}\left(C_{\epsilon 1}P_k - C_{\epsilon 2}\rho\epsilon\right) \tag{B.33}$$

The values for the coefficients used in this model are: $C_{\mu RS} = 0.1152$, $\sigma_{\epsilon RS} = 1.10$, $C_S = 0.22$, $C_{\epsilon 1}$=1.45, $C_{\epsilon 2}$=1.9. The eddy viscosity, μ_t, is computed using Equation B.6, where C_μ is now replaced by $C_{\mu RS}$.

B.2.2 The LPS model

The LPS model, in ANSYS Fluent (release 17.2), models the D^t_{ij}, D^p_{ij}, ϕ_{ij}, and ϵ_{ij} terms in Equation B.28. The Reynolds stresses diffusion, D^t_{ij}, and the pressure diffusion, D^p_{ij}, terms

are combined as a total turbulent diffusion term, D_{ij}^{T}, which is modelled by Equation B.34.

$$D_{ij}^{T} = \frac{\partial}{\partial x_k}\left(\frac{\mu_t}{\sigma_k}\frac{\partial \langle u_i u_j \rangle}{\partial x_k}\right) \tag{B.34}$$

where μ_t is computed in the same manner as in Equation B.6, and $\sigma_k = 0.82$.

The pressure strain term, ϕ_{ij}, is modelled significantly differently compared to the LRR-IP model. Equation B.35 shows the approach used to model ϕ_{ij}, as presented in the ANSYS Fluent Theory Guide (release 17.2) [48]. Note that, the main difference is the presence of a so-called wall reflection term, $\phi_{ij,w}$, which redistributes the normal stresses near the wall [48]. $\phi_{ij,w}$ is included by default in the LPS model.

$$\begin{aligned}\phi_{ij} = &\overbrace{-C_1\rho\frac{\epsilon}{k}(\langle u_i u_j\rangle - \frac{2}{3}\delta_{ij}k)}^{\phi_{ij,1}}\overbrace{-C_2\left\{(P_{ij} - \frac{5}{C_{ij}}) - \frac{2}{3}\delta_{ij}(P - \frac{5}{C})\right\}}^{\phi_{ij,2}} \\ &\overbrace{+C_1'\frac{k}{\epsilon}\left\{\langle u_k u_m\rangle n_k n_m \delta_{ij} - \frac{3}{2}\langle u_i u_k\rangle n_j n_k - \frac{3}{2}\langle u_j u_k\rangle n_i n_k\right\}\frac{C_l k^{3/2}}{\epsilon d}}^{\phi_{ij,w}} \\ &\overbrace{+C_2'\left\{\phi_{km,2} n_k n_m \delta_{ij} - \frac{3}{2}\phi_{ik,2} n_j n_k \frac{3}{2}\phi_{jk,2} n_i n_k\right\}\frac{C_l k^{3/2}}{\epsilon d}}^{\phi_{ij,w}}\end{aligned} \tag{B.35}$$

In this model $C_1 = 1.8$, $C_2 = 0.60$, $P{=}\frac{1}{2}P_{kk}$, $C{=}\frac{1}{2}C_{kk}$, $C_1' = 0.5$, $C_2' = 0.3$, n_k is the x_k component of the unit normal to the wall, d is the normal distance to the wall, $C_l = C_\mu^{3/4}/\kappa$, where $C_\mu = 0.09$ and $\kappa = 0.04187$ is the von Kármán Constant.

An additional modification in the LPS model is presented for the near wall modelling when using ANSYS Fluent (release 17.2). The LPS model is modified when it is combined with the Enhanced Wall Treatment (EWT) presented in section B.3.3, which is the case for the present study. The coefficients C_1, C_2, C_1', and C_2' are modified as described in [48] based on studies from Launder and Shima [51].

$$C_1 = 1 + 2.58AA_2^{0.25}\{1 - \exp[-(0.0067Re_t)^2]\} \tag{B.36}$$

$$C_2 = 0.75\sqrt{A} \tag{B.37}$$

$$C_1^{'} = -\frac{2}{3}C_1 + 1.67 \tag{B.38}$$

$$C_2^{'} = \max\left[\frac{2/3C_2 - 1/6}{C_2}, 0\right] \tag{B.39}$$

The turbulent Reynolds number Re_t is defined in Equation B.40. The flatness parameter A is defined in Equation B.41 and the tensor invariants A_2 and A_3 in Equation B.42 and B.42, respectively. The Reynolds stress anisotropy tensor, a_{ij}, is also needed and defined in Equation B.44.

$$Re_t = \frac{\rho k^2}{\mu\epsilon} \tag{B.40}$$

$$A = \left[1 - \frac{9}{8}(A_2 - A_3)\right] \tag{B.41}$$

$$A_2 = a_{ik}a_{ki} \tag{B.42}$$

$$A_3 = a_{ik}a_{kj}a_{ji} \tag{B.43}$$

$$a_{ij} = -\left(\frac{-\rho\left\langle u_i u_j\right\rangle + \frac{2}{3}\rho k\delta_{ij}}{\rho k}\right) \tag{B.44}$$

The last term to be modelled in the Reynolds stress equation is the dissipation, ϵ_{ij}. That term modelled using the previous equation presented for the LRR-IP model, Equations B.31 and B.33. The values for the coefficients used in this model are: $\sigma_{\epsilon RS} = 1.0$, $C_{\epsilon 1}$=1.44, $C_{\epsilon 2}$=1.92. The eddy viscosity, μ_t, is computed using Equation B.6.

B.2.3 The SMC-ω model

The ω-based Second Moment Closure (SMC-ω) model solves the Reynolds stress equation along with an ω equation. Equation B.45 is the modelled Reynolds stress equation for the SMC-ω.

$$\underbrace{\rho \langle U \rangle_k \frac{\partial \langle u_i u_j \rangle}{\partial x_k}}_{C_{ij}} =$$

$$\underbrace{-\beta' C_1 \rho\omega(\langle u_i u_j \rangle - \frac{2}{3}k\delta_{ij}) - \hat{a}(P_{ij} - \frac{1}{3}P_{kk}\delta_{ij}) - \hat{\beta}(D_{ij} - \frac{1}{3}P_{kk}\delta_{ij}) - \hat{\gamma}\rho k(S_{ij} - \frac{1}{3}S_{kk}\delta_{ij})}_{\phi_{ij}}$$

$$\underbrace{-\rho\left[\langle u_i u_k \rangle \frac{\partial u_j}{\partial x_k} + \langle u_j u_k \rangle \frac{\partial u_i}{\partial x_k}\right]}_{P_{ij}} \underbrace{+\rho\frac{\partial}{\partial x_k}\left[\frac{\mu_t}{\sigma_k}\frac{\partial \overline{u_i u_j}}{\partial x_k}\right]}_{D^t_{ij}} \underbrace{+\frac{\partial}{\partial x_k}\left[\mu\frac{\partial \overline{u_i u_j}}{\partial x_k}\right]}_{D^\mu_{ij}} \underbrace{-\frac{2}{3}\beta'\rho\omega k\delta_{ij}}_{\epsilon_{ij}} \tag{B.45}$$

The production term P_{ij} in the pressure strain term has the same formulation as the production term itself. The D_{ij} term in the pressure strain term differs slightly from the P_{ij} formulation as shown in Equation B.46.

$$D_{ij} = \langle u_i u_k \rangle \frac{\partial u_k}{\partial x_j} + \langle u_j u_k \rangle \frac{\partial u_k}{\partial x_i} \tag{B.46}$$

The model constants are defined as follow: β'=0.09, $\hat{a} = (8 + C_2)/11$, $\hat{\beta} = (8C_2 - 2)/11$, $\hat{\gamma} = (60C_2 - 4)/55$, $C_1 = 1.8$, and $C_2 = 0.52$. The turbulent viscosity, μ_t, is defined as in the k–ω model (Equation B.18). It is also necessary to define an ω equation that can be solved along with the Reynolds stress equation, because the term ω is part of Equation B.45. This ω-equation is presented in Equation B.47.

$$\rho\frac{\partial(\langle U_k \rangle \omega)}{\partial x_k} = \frac{\partial}{\partial x_k}\left[(\mu + \frac{\mu_t}{\sigma})\left(\frac{\partial \omega}{\partial x_j}\right)\right] + \alpha\rho\frac{\omega}{k}P_k - \rho\beta\omega^2 \tag{B.47}$$

The coefficients for Equation B.47 are $\sigma = 2$, $\beta = 0.075$, and $\alpha = 5/9$.

B.3 Near Wall Region Modelling

The details of the near wall region modelling used for the turbulence models that are listed in Table 3.1 are now presented. The near wall region models used in this current study by ANSYS CFX are the Scalable Wall Functions (SWF) and the Automatic Wall Treatment (AWT). The Enhanced Wall Treatment (EWT) is used in ANSYS Fluent (release 17.2). The appropriate near the wall treatment is essential for accurate prediction of the turbulent flow field, as the near-wall regions generate most of the vorticity and turbulence. There are two main approaches to model the flow field near to the wall: first, use of semi-empirical equation to reproduce the flow field near to the wall and, second, use modified turbulence model to solve the flow field in the near the wall region.

B.3.1 Scalable Wall Functions (SWF)

The ANSYS CFX (release 16.2) uses a Scalable Wall Functions (SWF) to model the near wall region for specific models. It is a wall function approach based on Launder and Spalding [12, 48]. The method starts with a formulation that relates the friction velocity, u_τ to the wall shear stress τ_w in Equation B.48.

$$u_\tau = \left(\frac{\tau_w}{\rho}\right)^{1/2} \tag{B.48}$$

A dimensional distance from the wall, y^+, is also defined as shown in Equation B.49.

$$y^+ = \frac{\rho\ \Delta y\ u_\tau}{\mu} \tag{B.49}$$

In this technique, the near wall tangential velocity is related to the wall shear stress using a logarithmic relation, the well-known as the log-law and is defined as:

$$u^+ = \frac{U}{u_\tau} = \frac{1}{\kappa} ln(y^+) + B \tag{B.50}$$

The term u^+ is the near wall velocity, $\kappa = 0.41$ (von Karman constant), and $B = 5.2$ (log-layer constant).

The scalable wall function, however, has an alternative formulation for the velocity scale (u_τ). This velocity scale (u^*) replaces u_τ, and it is defined as follows:

$$u^* = {C_\mu}^{1/4} k^{1/2} \tag{B.51}$$

By using this new definition of the velocity scale (u^*), it is possible to obtain the following explicit equation for u_τ:

$$u_\tau = \frac{U}{\frac{1}{\kappa} ln(y^*) + B} \tag{B.52}$$

where y^* is defined as follow:

$$y^* = \frac{\rho \ \Delta y \ u^*}{\mu} \tag{B.53}$$

The wall shear stress value can be determined by:

$$\tau_\omega = \rho u^* u_\tau \tag{B.54}$$

The SWF methodology implemented in ANSYS CFX limits the y^* greater than o equal 11.06; this value represents the intersection between the logarithmic and linear near wall profiles. In this method, all mesh points are outside the viscous sublayer. The dissipation rate (ϵ) in the logarithmic region is also defined by the following equation:

$$\epsilon = \frac{\rho u^*}{\tilde{y}^* \mu} \frac{C_\mu^{3/4}}{\kappa} k^{3/2} \tag{B.55}$$

where $\tilde{y}^*$ is defined as $\max(y^*, 11.06)$.

The SWF technique is implemented in the Second Moment Closure Models based on the dissipation rate (ϵ) equation in ANSYS CFX. It is also applied in the Standard k-ϵ model. The current study makes use of the SWF for the $LRR - IP$ model because it is the only near wall treatment option available for that model.

B.3.2 Automatic Wall Treatment (AWT)

The Automatic Wall Treatment (AWT) is available in ANSYS CFX (release 16.2). This method is based on the use of low-Reynolds near wall formulation instead of wall functions, if

the mesh is fine enough. A mesh refinement with y^+ (Eq. B.49) around 1 is recommended [48]. This method is used for all omega-based turbulence models in ANSYS CFX (release 16.2). The method formulation details are provided by the equations as follows. The flux for the k equation is kept to be zero (Equation B.56) and the flux in the momentum equation depends on the velocity profile (Equation B.57).

$$F_k = 0 \tag{B.56}$$

$$F_U = -\rho u_\tau u^* \tag{B.57}$$

u_τ and u^* are obtained from the following expressions:

$$u^* = \sqrt[4]{\left(\sqrt{\frac{\mu}{\rho}\frac{\Delta U}{\Delta y}}\right)^4 + \left(\sqrt{a_1 k}\right)^4} \tag{B.58}$$

and

$$u_\tau = \sqrt[4]{(u_\tau{}^{vis})^4 + (u_\tau{}^{log})^4} \tag{B.59}$$

with

$$u_\tau{}^{vis} = \sqrt{\frac{\mu}{\rho}\left|\frac{\Delta U}{\Delta y}\right|} \tag{B.60}$$

and

$$u_\tau{}^{log} = \frac{U}{\frac{1}{\kappa} log(y^+) + C} \tag{B.61}$$

An algebraic formulation is known for the turbulent frequency, ω, and it is used instead of an added flux for the ω-equation. One ω expression is determined for the logarithmic region, ω_l, and one for the sublayer region, ω_s.

$$\omega_l = \frac{u^*}{a_1 \kappa y} = \frac{1}{a_1 \kappa \nu}\frac{u^{*2}}{y^+} \tag{B.62}$$

$$\omega_s = \frac{6\nu}{\beta\left(\Delta y^2\right)} \tag{B.63}$$

where Δy represents the distance between the first and the second mesh points. Both formulations are blended using Equation B.64.

$$\omega_\omega = \omega_s \sqrt{1 + \left(\frac{w_l}{w_s}\right)^2} \tag{B.64}$$

The main advantage of the formulation is that the location of the first mesh point near the wall can be positioned in the viscous sublayer, and it can have better predictive performance.

B.3.3 Enhanced Wall Treatment (EWT)

The Enhanced Wall Treatment (EWT) used in ANSYS Fluent uses a two-layer model or an enhanced wall function [48]. The EWT method allows for fine meshes. Where y^+ is smaller than 1, the model uses a two-layer approach for the near the wall region. If the mesh is not fine enough, the treatment will apply enhanced wall functions to model the near wall region. In the current studies, fine meshes were used to allow the model to perform calculations in the near wall region using a two-layer approach. The two-layer approach divides the entire solution domain into two regions: a viscous sublayer region where the turbulent Reynolds number, Re_y, is less than 200, and a fully turbulent region for Re_y greater than 200. Equation B.65 defines Re_y based on a wall distance, y, interpreted as the nearest wall distance given by Equation B.66.

$$Re_y = \frac{\rho y \sqrt{k}}{\mu} \tag{B.65}$$

$$y = \min_{\vec{r_w} \in \Gamma_w} ||\vec{r} - \vec{r_w}|| \tag{B.66}$$

where $\vec{r}$ is the position vector at the field point, and $\vec{r_w}$ is the position vector of the wall boundary which satisfies the following criteria: $\vec{r_w} \in \Gamma_w$. Γ_w is the union of all the wall boundaries involved.

In the fully turbulent region, $Re_y > 200$, the equations for the two-equation or the SMC models are employed. For the viscous sublayer region where $Re_y < 200$, the one-equation

model from Wolfstein [52] is employed. This one-equation model retains the momentum Equation B.2 and the k equations for two-equation, Equations B.4. In the SMC models k is computed by the mean of the turbulent normal stresses. However, the turbulent viscosity, μ_t, is computed from Equation B.67 using a length scale l_μ defined in Equation B.68.

$$\mu_{t,2layer} = \rho C_\mu l_\mu \sqrt{k} \tag{B.67}$$

$$l_\mu = y C_l{}^* (1 - e^{-Re_y/A_\mu}) \tag{B.68}$$

This two-layer definition for the eddy viscosity is smoothly blended with the high-Reynolds number definition from the outer region, as follow:

$$\mu_{t,enh} = \lambda_\epsilon \mu_t + (1 - \lambda_\epsilon)\mu_{t,2layer} \tag{B.69}$$

The blending function, λ_ϵ, is defined in such a way that it is equal to unity away from walls and is zero in the vicinity of the walls. The blending function is defined in Equation B.70.

$$\lambda_\epsilon = \frac{1}{2}\left[1 + \tanh\left(\frac{Re_y - Re_y^*}{A}\right)\right] \tag{B.70}$$

The constant A computes the width of the blending function as follow:

$$A = \frac{|\Delta Re_y|}{\tanh^{-1}(0.98)} \tag{B.71}$$

The ΔRe_y values are between 5% and 20% of Re_y^*. The blending function λ_ϵ prevents the solution from diverging if the value of μ_t obtained in the outer layer is different from μ_t at the edge of the viscous sublayer region with the fully turbulent region. A value for ϵ is computed in the viscosity affected region in Equation B.72.

$$\epsilon = \frac{k^{3/2}}{l_\epsilon} \tag{B.72}$$

The length scales are computed in Equation B.73 using Chen and Patel definition [53].

$$l_\epsilon = y C_l^* \left(1 - \epsilon^{\frac{-Re_y}{A_\epsilon}}\right) \tag{B.73}$$

The constant values are: $C_l^* = \kappa C_\mu^{-3/4}$, A_μ=70, and $A_\epsilon = 2C_l^*$

Appendix C

Approaching Flow Characteristics

The inlet flow conditions for the experimental and numerical studies were analyzed to confirm that fully developed turbulent flow conditions existed at an upstream location before the wavy section. DNS simulations result from Moser *et al.* [54] and relevant literature were used for validation purposes.

C.1 Experimental Investigation

Test Conditions

The turbulent boundary layer over the flat wall was accelerated in the inlet section before the wavy section by tripping the flow with a sandpaper sheet measuring 186 mm in width and 35 mm in length (in the flow direction) placed at the leading top and bottom edges of the entrance of the test channel (as previously mentioned in section 3.1.1). PIV measurements at an upstream plane (P0) in Figure 3.2 located 100 mm before the wavy section were analyzed to verify a fully developed turbulent flow before the wavy section. The experimental flow conditions studied were for the Reynolds number ($\mathrm{Re_b}$) of 5040, 8387, 10671, and 13039 with respective bulk velocity values of U_b = 0.340, 0.565, 0.719, and 0.788 m/s, and h = 15 mm. The fluid properties were taken as ρ = 998 kg/m^3, and μ = 0.00101 kg/m·s. The inlet conditions were explored for a single test condition with $\mathrm{Re_b}$=10671. Note that the Reynolds number ($\mathrm{Re_b}$) commonly used for wavy geometries estimates of the bulk velocity from the top of the wavy bottom wall to the top flat wall for the channel. Equation C.1 introduces a new Reynolds number ($\mathrm{Re_{in}}$) definition commonly used for flat-walled channels.

$$\mathrm{Re_{in}} = \rho U_{\mathrm{in}} h / \mu \tag{C.1}$$

The U_{in} value is obtained from the local velocity profile, $U(y)$, in Equation C.2, where

$$U_{\text{in}} = (2h)^{-1} \int_{y_{\text{wall}}=0}^{2h} U(y)dy \tag{C.2}$$

The four Reynolds numbers studied (previously given in terms of Re_{b}) are equivalent to Re_{in} of 4606, 7665, 9753, and 11917 with average inlet velocity values of U_{in} = 0.305, 0.507, 0.645, and 0.788 m/s. Because the mass flow rate is conserved, the differences in Reynolds number are due to the same length scale (h) for both Reynolds number definitions, but with two different averaged velocity scales (U_b and U_{in}). There is one that is commonly used for wavy wall channels (U_b), and one that is commonly used for flat wall channels (U_{in}). The second velocity scale, U_{in}, is only used in this section as a reference to verify the flow conditions with other flat wall channel flow characteristics.

The test conditions information in Table C.1 for Re_{in} of 9753 contains: the channel height (h), the maximum velocity U_c, y-coordinate location of the maximum velocity y_{max}, inlet averaged velocity U_{in}, ratio between U_c and U_{in}, and friction velocity u_τ. Four Reynolds number definitions are shown: Re_{b} (Eq. 2.10), Re_{in} (Eq. C.1), $\text{Re}_{\text{b}_\tau}$ ($u_\tau y^+/\nu$), and Re_θ (Eq. C.5).

Even if the channel height is different, a fully developed turbulent flow is expected to occur, and they can be qualitatively compared to another PIV experiment [49] performed in a similar water channel but with different channel height (h) and Reynolds number as shown in Table C.1. The comparison aims to understand the test conditions when using similar experimental techniques. The y_{max}/h value expected for a turbulent channel flow is one (maximum mean streamwise velocity at the center of the channel); this is the case for the DNS data [54] in Table C.1. The experimental values are slightly different than one for both the current and Shah *et al.* [49] experimental data. Besides the data from [49], other available literature and empirical correlations were used to provide insights into the flow conditions. Dean's [55] defined a correlation between the centerline velocity (assumed to be the maximum velocity for asymmetric profile) and the averaged inlet velocity, $U_c/U_{in} = 1.28Re_{\text{in}}^{-0.0116}$, which yields a value of 1.15 for $Re_{\text{in}} = 9753$. This ratio compares very well with the current

experimental data ratio of 1.14. The same correlation applied to Shah *et al.* [49] data yields a ratio of 1.14, which is comparable to their experiment ratio of 1.10. Those values are also in agreement with the fully turbulent flow DNS simulation in a smooth wall channel from Moser *et al.* [54], where the ratio $U_c/U_{in} = 1.14$ for $\mathrm{Re_{in}}$=10953.

A few relevant parameters of the approaching boundary layer are also presented in Table C.1; their detailed formulations can be found in the literature [9]. They are important to reveal the actual BL characteristics for this particular experiment. The boundary thickness (δ) was calculated based on the location where the $\langle U \rangle$ velocity reached 99% of the maximum free-stream velocity, which is also defined as the centreline velocity (U_c) for the closed channel. The displacement thickness (δ^*) and the momentum thickness (θ) are estimated by Equation C.3 and C.4, respectively.

$$\delta^* = \int_{y_{\mathrm{wall}}=0}^{y_{max}} \left(1 - \frac{\langle U \rangle}{U_c}\right) dy \tag{C.3}$$

$$\theta = \int_{y_{\mathrm{wall}}=0}^{y_{max}} \frac{\langle U \rangle}{U_c} \left(1 - \frac{\langle U \rangle}{U_c}\right) dy \tag{C.4}$$

A Reynolds number based on momentum thickness is defined as follow:

$$\mathrm{Re_{b\theta}} = \rho U_c \theta / \mu \tag{C.5}$$

The shape factor H defines the ratio of the displacement δ^* and momentum θ thickness.

It is notable that the upper and lower BL parameters are not identical due to the lack of perfect symmetry of the mean velocity profiles concerning $y = h$, which is seen later in Figure C.3. The δ value is not exactly 15 mm, as mentioned earlier due to the lack of symmetry, which yields a δ/h value of less than one for both lower and upper portion of the channel. It is not surprising since it was observed in other experiments that perfect symmetry is not always be possible in an experimental set-up. The displacement thickness (δ^*) and the momentum thickness (θ) values are comparable to DNS [54] at similar Reynolds number as shown in Table C.1. The shape factor H values are higher than the DNS data [54],

since the displacement thickness is slighted higher for the present study. In overall, the BL developed in the experiment presented satisfactory BL parameters when comparing to DNS and the other PIV experiment.

Table C.1: Summary of test conditions and boundary layer parameters for the experiments

	Present Study PIV		Moser *et al.* [54] DNS		Shah *et al.* [49] PIV	
Test Conditions						
h (mm)	15		1		23	
U_c (m/s)	0.74		21.26		0.85	
y_{max}/h	1.1		1		0.93	
U_{in} (m/s)	0.65		18.65		0.78	
U_c/U_{in}	1.14		1.14		1.10	
u_τ (m/s)	0.036		1		0.040	
$\mathrm{Re_b}$	10671		12267		17860	
$\mathrm{Re_{in}}$	9753		10953		16324	
$\mathrm{Re_{b\tau}}$	515		587		612	
Boundary Layer Parameters						
	lower	upper	lower	upper	lower	upper
δ/h	0.968	0.774	1.0	1.0	0.696	0.696
δ^*/h	0.145	0.108	0.123	0.123	0.090	0.073
θ/h	0.088	0.075	0.088	0.088	0.060	0.495
H	1.640	1.440	1.397	1.397	1.510	1.470
Re_θ	982	833	1096	1096	1160	970

Flow Characteristics

Details of the turbulent flow are further explored in Figures C.1 and C.2. DNS data from Moser *et al.* [54] at $\mathrm{Re_{in}} = 10950$ are used for verification. Profiles of dimensionless mean velocity in outer coordinates and inner coordinates, y^* and y^+, are presented for the approaching flow in Figure C.1. The bottom half profile agreed reasonably well with the DNS data in Figure C.1 (a), the upper half had deviations from the DNS data [54]. The mean velocity in the inner coordinates is shown in Figure C.1 (b); the experimental data agreed well in the log-law region with both the log-law itself and the DNS data. The log-law constants were $\kappa = 0.41$ and $B = 5$. That particular graph requires estimating the friction velocity, u_τ, for the experiments. The Clauser plot technique was used and yields a value of 0.036 m/s for the friction velocity.

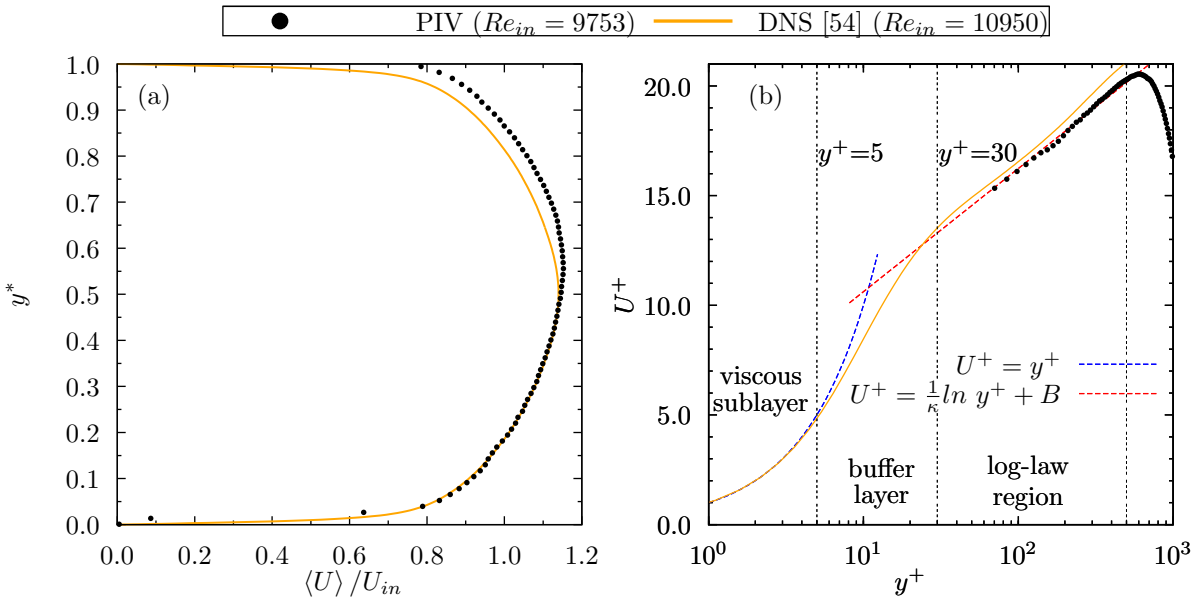

Figure C.1: Approaching turbulent flow over the upstream smooth wall channel for the PIV experimental data: (a) dimensionless mean velocity, $\langle U \rangle / U_{in}$; (b) dimensionless mean velocity, U^+, in log-scale, y^+.

The current experimental set-up was not able to capture the viscous sublayer in Fig-

ure C.1 (b) and yielded a $RMS_{RN,U}$ value of 15.45% to DNS [54]; the relatively high deviations due to the near-wall region, and to the not perfectly symmetric profiles. Turbulence quantities profiles are presented in Figure C.2. The velocity fluctuations in the streamwise direction, u^+, did not capture well the near wall peak.

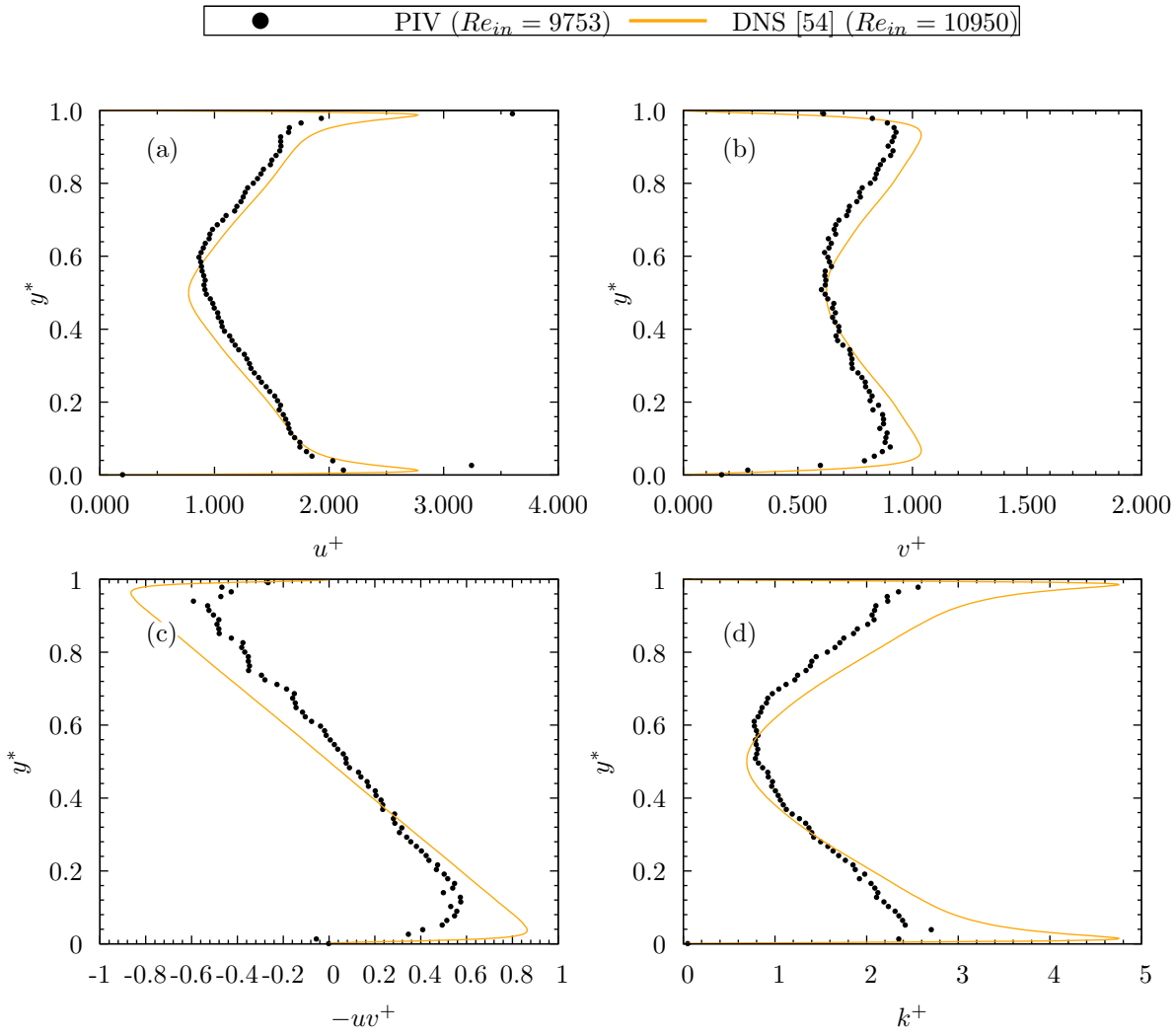

Figure C.2: Approaching turbulent flow over the upstream smooth wall channel for the PIV experimental data: (a) dimensionless velocity fluctuations in the streamwise direction, u^+; (b) and in the wall-normal direction, v^+; (c) dimensionless Reynolds shear stress, uv^+; (d) dimensionless turbulent kinetic energy, k^+.

In later discussion, it is demonstrated that the average turbulence intensity based on the velocity fluctuations along the channel was quantitatively comparable to the value in the literature. The dimensionless velocity fluctuations in the streamwise direction, u^+, and in the wall-normal direction, v^+, are in reasonable agreement with the DNS data [54].

The dimensionless Reynolds shear stress, uv^+, has a peak of about 0.6 which is considerably lower than the peak of 0.87 for the DNS data [54] in Figure C.2 (c). The under prediction might be related to the inability of the experimental method to capture the fluctuating wall-normal velocity component v, which is evident by the under-predicted v^+ profiles in Figure C.2 (b). The overall uv^+ trend is comparable to the literature. Due to the asymmetric profile, the zero uv^+ value that was expected to be located at $y^* = 0.5$ is shifted to about $y^* = 0.6$.

The k is the turbulent kinetic energy estimated as $k = 0.5\{\langle u^2\rangle + 2.45\langle v^2\rangle\}$. The $\langle w^2\rangle$ was estimated to be 1.45 times bigger than $\langle v^2\rangle$ based on the integration averaged profiles along the channel height for a typical turbulent channel flow [54].

A turbulence intensity, T_u, can be obtained using Equation C.6 [56, 57].

$$T_u(y) = \frac{\sqrt{\frac{1}{3}(u_i^2)}}{\sqrt{\langle U_i\rangle^2}} \times 100\% \tag{C.6}$$

The current experiment does not measure the third component of the velocity, W. Therefore, its value and the fluctuation w cannot be obtained. Fortunately, the magnitude of those components are well-known for a flat wall closed channel. The literature [9] indicates that the mean wall normal and span-wise velocities are negligible for a fully developed channel flow. DNS data [54] for the averaged velocity fluctuation w along the channel height were compared to the averaged velocity fluctuation, v. The DNS data comparison reveals that the average velocity fluctuation w along the channel is equal to $1.2v$. Based on that, the current experimental averaged velocity fluctuation w was estimated to be equal to $1.2v$. The

average turbulence intensity, T_u, Equation C.6 can be rewritten for the current experiment as follow:

$$T_u(y) = \frac{\sqrt{\frac{1}{3}(u^2 + v^2 + (1.2v)^2)}}{\sqrt{\langle U \rangle^2}} \times 100\% \tag{C.7}$$

Note that the averaged values for u, v, and $\langle U \rangle$, are calculated by integrating their profile along the entire channel height, because the velocity statistics depend on y. An average turbulent intensity ($\langle T_u \rangle$) value can be estimated for the experiments based on Equation C.7 to be 5.7 %. This value is in complete agreement with the DNS data [54] which also yields a value equal to 5.7 %. Even though the experimental turbulent fluctuations profiles are under predicted in the near-wall regions, the turbulent intensity levels are in good agreement with typical turbulent channel flows [54]. That can be explained by the higher streamwise velocity fluctuations u in the channel centre when compared to [54], as mentioned earlier.

The streamwise turbulence intensity I is a typical definition used to define boundary conditions in RANS numerical simulations. I is defined in Equation C.8 and is calculated from the experimental data to give a reference value compared to the current numerical simulations.

$$I = \frac{u}{\langle U \rangle} \times 100\% \tag{C.8}$$

The averaged I value along the channel height is estimated to be 7.62 % for the experiments, which compares well with the values found for the DNS data [54] of 7.34 %.

A eddy viscosity ratio μ_τ/μ is calculated from the experimental data and yields a value of 25.71, whereas the DNS data [54] give a value of 12.6. The eddy viscosity was calculated here using Equation C.9.

$$\nu_t = \frac{-\langle uv \rangle}{\frac{\partial U}{\partial y}} \tag{C.9}$$

C.2 Numerical Modeling of the Inlet Region

C.2.1 Flow characteristics

The streamwise velocity profile is presented in outer coordinates and inner coordinates in Figure C.3. DNS simulations for similar Reynolds number [54] are compared to the current RANS models. The dimensionless mean velocity, $\langle U \rangle / U_{in}$, agrees very well with the DNS data in both outer and inner coordinate systems.

The $RMS_{RN,U}$ values quantify the differences between the results of each turbulence model simulation and the Moser *et al.* [54] DNS results. The $RMS_{RN,U}$ values for the k–ϵ, R-k–ϵ, k–ω, and SST models were 1.73 %, 1.54 %, 1.39 %, and 1.61 %, respectively. The two-equation turbulence models with their respective U_c/U_{in} ratio values are: Standard k–ϵ (1.11), R-k–ϵ (1.11), k–ω (1.13), and SST (1.12).

The RANS models profiles are in good agreement with the viscous sublayer and the log-law regions as seen in Figures C.3 (b) and (c). Figures C.3 (c) differs from Figures C.3 (b) because it uses a logarithmic scale on both axes and shows how the linear behavior at the near wall region is adequately predicted by all models.

The dimensionless turbulent kinetic energy is in reasonably good agreement with DNS data within the majority of the channel height. The peak near the wall is, however, under-predicted. In that region, the k-ϵ, Realizable k-ϵ models performed better than the ω based two-equations models.

The SMC models also predicted the inlet flow characteristics very well, except the $LRR-IP$ model, which did not predict the quantities presented well, as seen in Figure C.4. The $RMS_{RN,U}$ values for the LRR-IP, LPS, and SMC-ω models were 13.65 %, 2.09 %, and 1.48 %, respectively. The SMC turbulence models with their respective U_c/U_{in} ratio values are: LRR-IP (1.12), LPS (1.11), and SMC-ω (1.12). The RANS SMC models profiles are in good agreement with the viscous sublayer and the log-law regions, as seen in Figures C.4

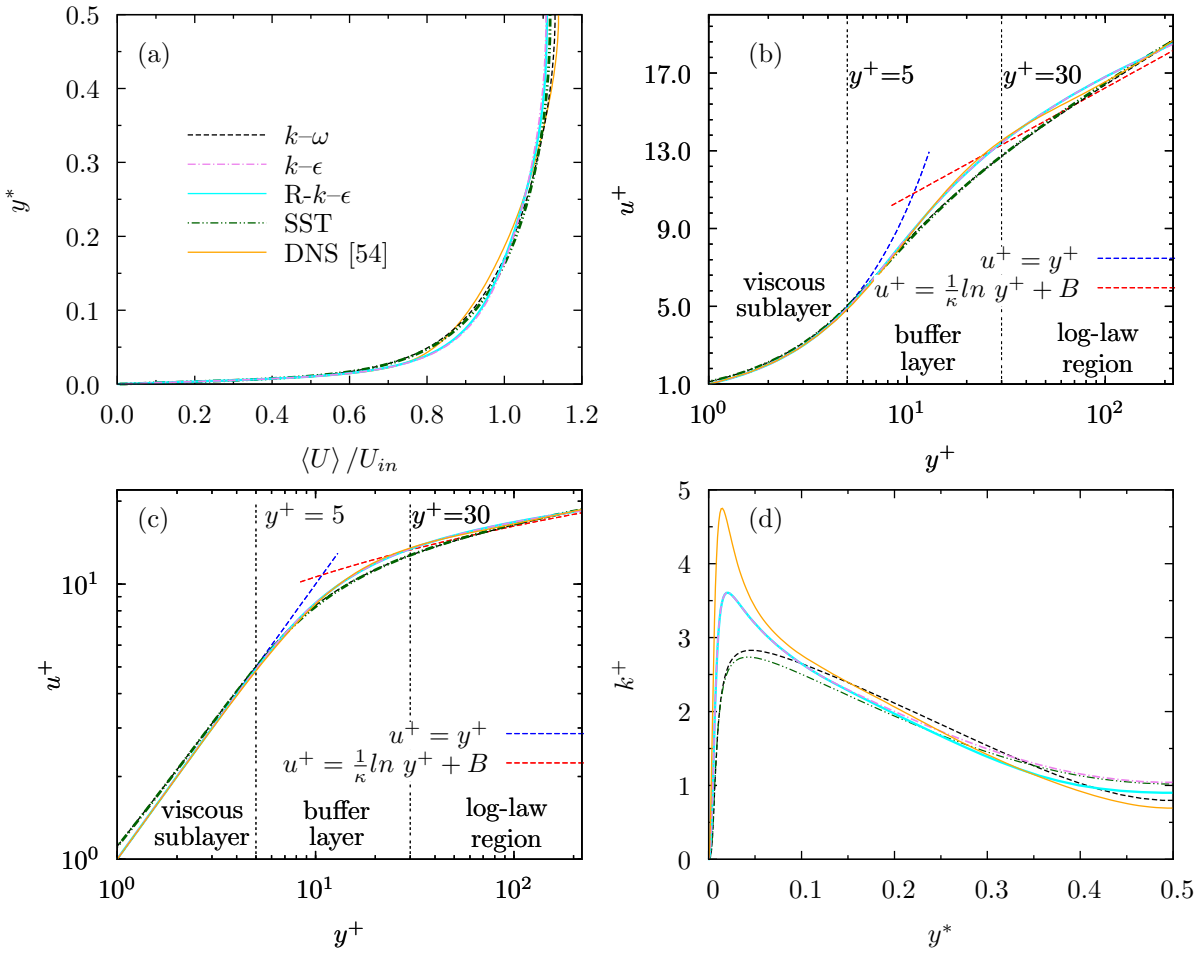

Figure C.3: Approaching turbulent flow over the upstream smooth wall channel for the two equations eddy viscosity models: (a) dimensionless mean velocity, $\langle U \rangle / U_{in}$; (b) dimensionless viscous mean velocity, u^+, with wall units axis in log-scale, y^+; (c) dimensionless viscous mean velocity, u^+, and wall units, both axes in log-scales; (d) dimensionless turbulent kinetic energy, k^+.

(b) and (c). The linear profile in the near wall region is adequately predicted by all models, except for the $LRR - IP$ model. The dimensionless turbulent kinetic energy predictions for the LPS, and SMC-ω models are good agreement with DNS data within the majority of the

channel height. In the near wall region the LPS model had the closest prediction of the peak of the k^+ profile.

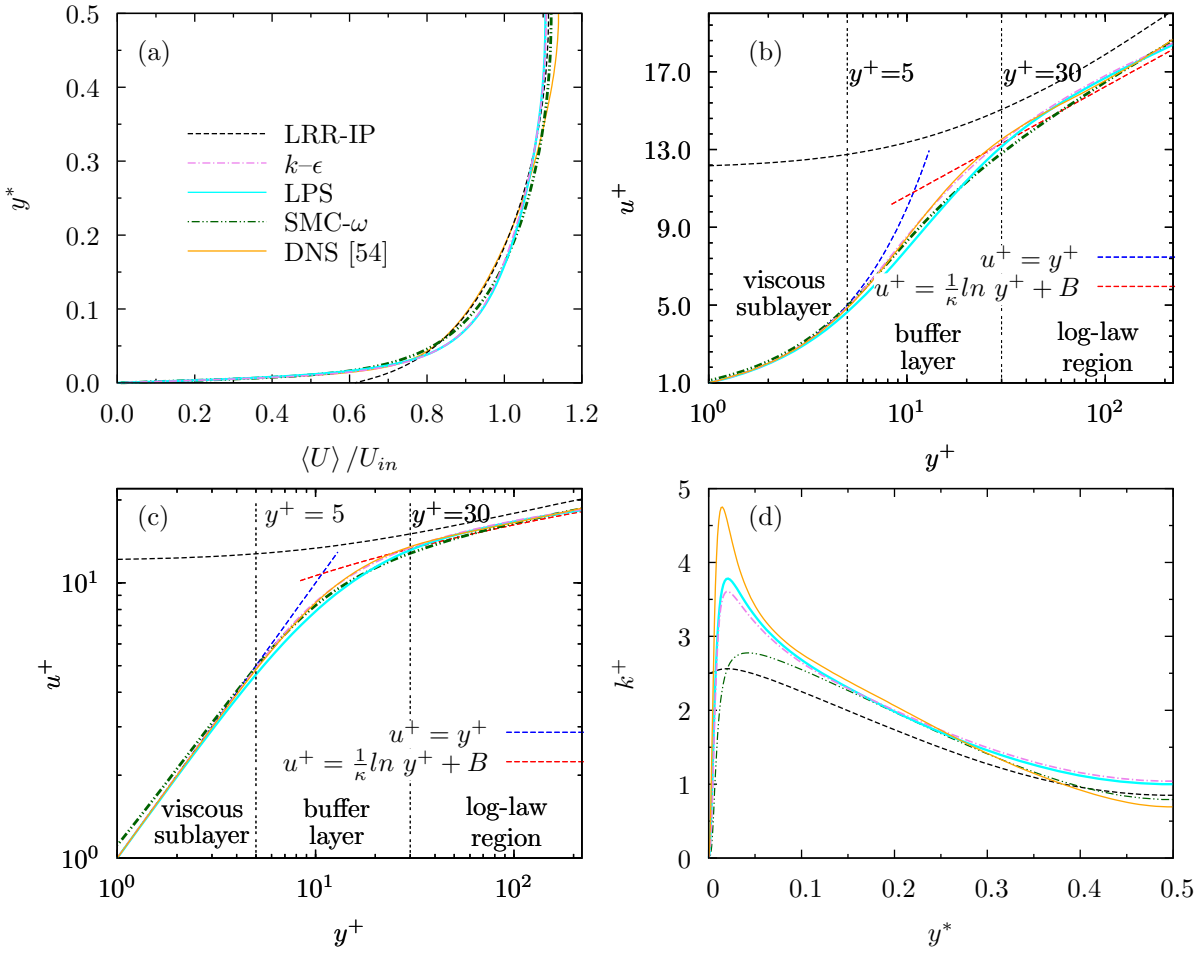

Figure C.4: Approaching turbulent flow over the upstream smooth wall channel for the SMC models: (a) dimensionless mean velocity, $\langle U \rangle / U_{in}$; (b) dimensionless viscous mean velocity, u^+, with wall units axis in log-scale, y^+; (c) dimensionless viscous mean velocity, u^+, and wall units, both axes in log-scales; (d) dimensionless turbulent kinetic energy, k^+.

The turbulence intensity, I, and the eddy viscosity ratio, μ_τ/μ, were prescribed for the

inlet boundary. Those values, however, change as the flow develops, and only their values in the fully developed region can be compared to experimental or DNS data.

The average turbulence intensity, I, is calculated using Equation C.10 had values of 6.2, 6.06, 5.9, 5.95, 6.11, 6.13 , and 6.65 % for the k–ϵ, R-k–ϵ, k–ω, SST, LPS, LRR-IP, and SMC-ω models, respectively.

$$I = \sqrt{\frac{2}{3}\frac{\langle k \rangle}{\langle U \rangle^2}} \times 100\% \tag{C.10}$$

In Equation C.10, $\langle k \rangle$ and $\langle U \rangle$ are the area-averaged turbulent kinetic energy and streamwise velocity, respectively. The average turbulence intensity, I, for the experiment and DNS data [54] were 7.62% and 7.34%, respectively. The average intensity for the fully developed profile in the results from the turbulence models was in the range from 5.95% to 6.65%, which is good agreement with the experiment and DNS results [54].

The area-averaged eddy viscosity ratio, μ_τ/μ, for the k–ϵ, R-k–ϵ, k–ω, SST, LPS, LRR-IP, and SMC-ω models were 51.55, 56.46, 44.90, 49.66, 50.66, 39.40, and 45.27, respectively. The average viscosity ratio for the fully developed region was calculated to be 25.71 and 12.6 for the experiments and DNS data [54], respectively. The average viscosity ratio for the turbulence models was in the range 39.40 to 56.46. The eddy viscosity ratio is about twice as large as the experiments and about four times the value from the DNS data [54].

Finally, to verify the influence of changing the inlet conditions on the results in the fully developed region, six additional runs using the k–ω model were conducted using different combinations of inlet intensity and viscosity ratio. In these tests, the inlet intensity was varied from 3% to 7% and the viscosity ratio was varied from 5 to 20. The results showed that the average intensity and viscosity ratio in the fully developed region were the same for all six cases and equal to the values obtained using the initial conditions (5% intensity and viscosity ratio of 10). A comparison of profiles of mean streamwise velocity and turbulent kinetic energy also showed no noticeable differences among the profiles corresponding to the different combinations of intensity and viscosity ratio. There was no effect of the inlet

boundary condition changes on the results in the full developed region, so it was concluded that the conditions used were appropriate.

Appendix D

Additional Experimental Results

D.1 Recirculation Region Characterization

Figure D.1 shows the mean streamlines for $\mathrm{Re_b} = 10700$ for Wave 1, Wave 3, Wave 6, and Wave 9. It is visually evident the similarity between the flow at Waves 3, 6, and 9. Note that Wave 8 results are summarized in the Table 4.1, but the plots are not presented for brevity and due to their close similarity to Wave 9. The streamline plot at Wave 1 reveals a much higher $\tilde{x}_c$ value of about 0.55 compared to 0.47 at Wave 3, 6, and 9, demonstrating that the $\tilde{x}_c$ value remained unchanged after Wave 3. The separation and reattachment locations, $\tilde{x}_s$ and $\tilde{x}_r$, are very similar at Waves 3, 6, and 9; the differences are close to or within the uncertainty of determining the locations. At Wave 1, however, the separation and reattachment locations are quite different, revealing a larger recirculation region at Wave 1.

The 50% forward fraction contours for $\mathrm{Re_b} = 10700$ are presented in Figure D.2 for Wave 1, Wave 3, Wave 6, and Wave 9. Similar to what was seen in Figure D.1, Wave 1 is the only wave with significant differences in recirculation locations. The separation and reattachment locations values in Table 4.1 for the forward fraction technique shown an almost identical recirculation size for all waves except Wave 1. The contours at Waves 6 and 9 were extrapolated at the reattachment locations, as demonstrated by the dashed lines. This extrapolation was necessary due the uncertainty in values of velocity very near to the wall. The same was done at the separation location at Wave 3. Buckles *et al.* [25] presented results called the flow intermittency, defined as the fraction of time that the velocity u is positive, which is similar to what the forward fraction represents here. Their results showed equally positive and negative u values at the separation location, which agrees with findings here as well. Note that it was also found that the forward fraction results at the maximum reverse

flow region, are in the reverse direction more than 80% of the time for this study. This trend is also in agreement with Buckles *et al.* [25]. It should also be noted that the separation and reattachment are considered fixed locations for the averaged quantities. The forward flow fraction, however, reveals that even after the reattachment or before the separation (for example, at $\tilde{x} = 0.1$ and 0.75), reverse flow still occurs more than 30% of the time, indicating a change on the separation and reattachment over time. Buckles *et al.* [25] described the flow as unsteady at those two locations due the reverse flow occurrences.

Figure D.3 shows the dimensionless mean streamwise velocity contours at $\mathrm{Re_b} = 10700$for

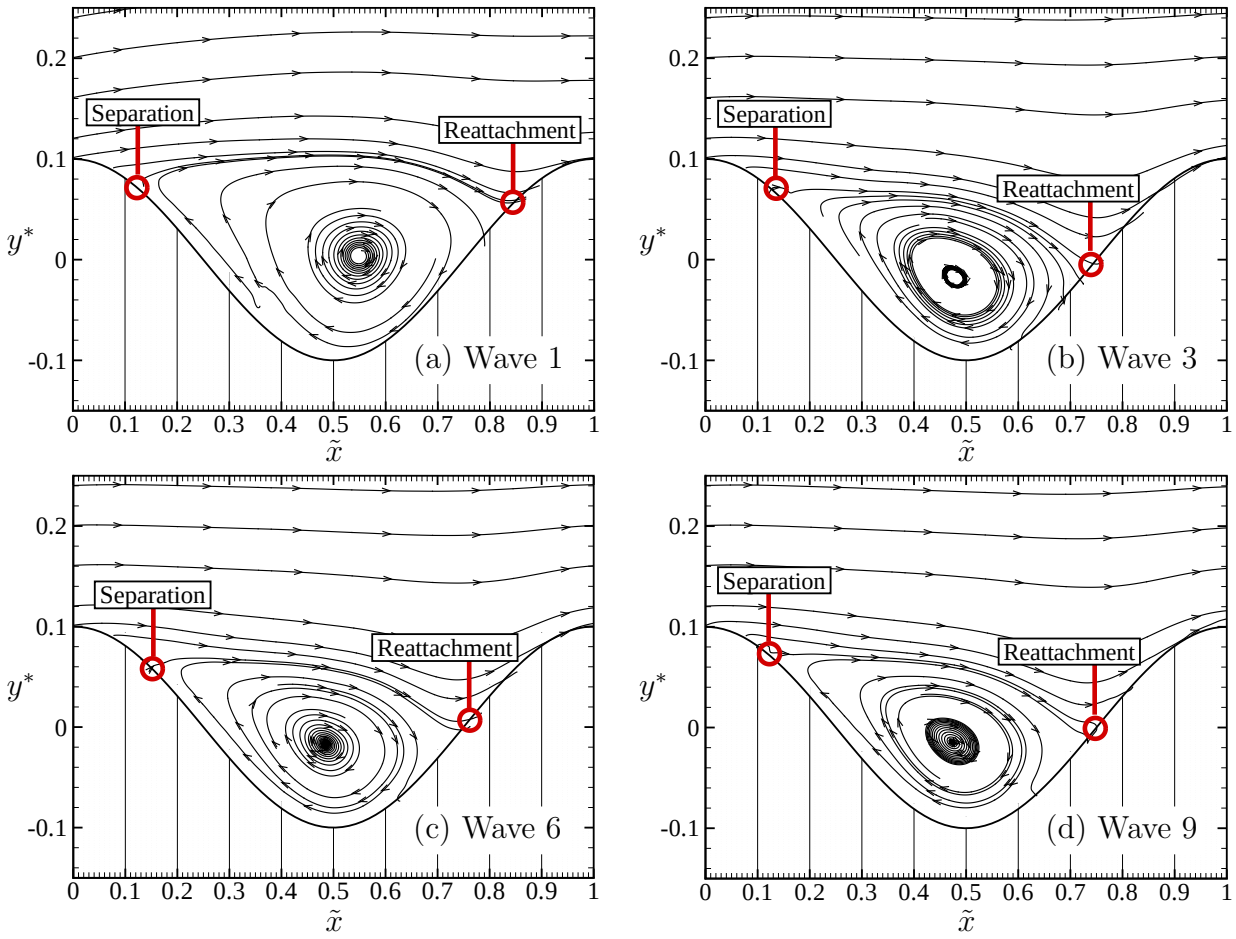

Figure D.1: Contour plots of mean streamlines at (a) Wave 1, (b) Wave 3, (c) Wave 6 and (d) Wave 9, at $\mathrm{Re_b} \approx 10700$.

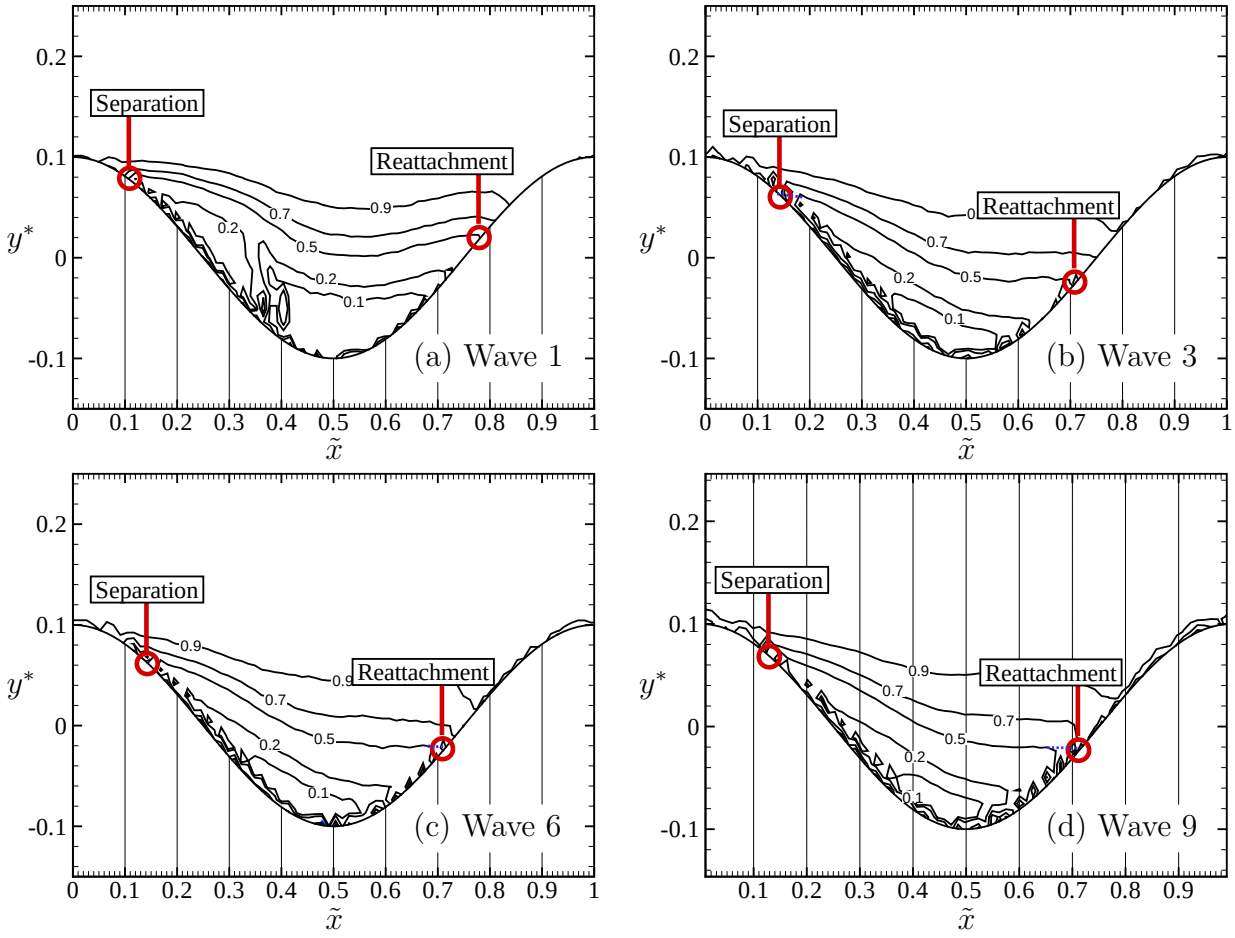

Figure D.2: Contour plots of forward flow fraction at (a) Wave 1, (b) Wave 3, (c) Wave 6 and (d) Wave 9, at $\mathrm{Re_b} \approx 10700$.

Wave 1, Wave 3, Wave 6, and Wave 9. The contours reveals the same features described in the other techniques presented. The recirculation locations are summarized in Table 4.1. The dimensionless mean streamwise velocity contours at Waves 6 and 9 were extrapolated at the reattachment and separation locations as demonstrated by the dashed lines; again, this was necessary due the uncertainty near the wall. The same was done for the separation location at Wave 3. The similarity between the mean streamwise velocity and forward fraction results is no surprise, because Buckles *et al.* [25] observed that both methods yielded very similar separation and reattachment locations.

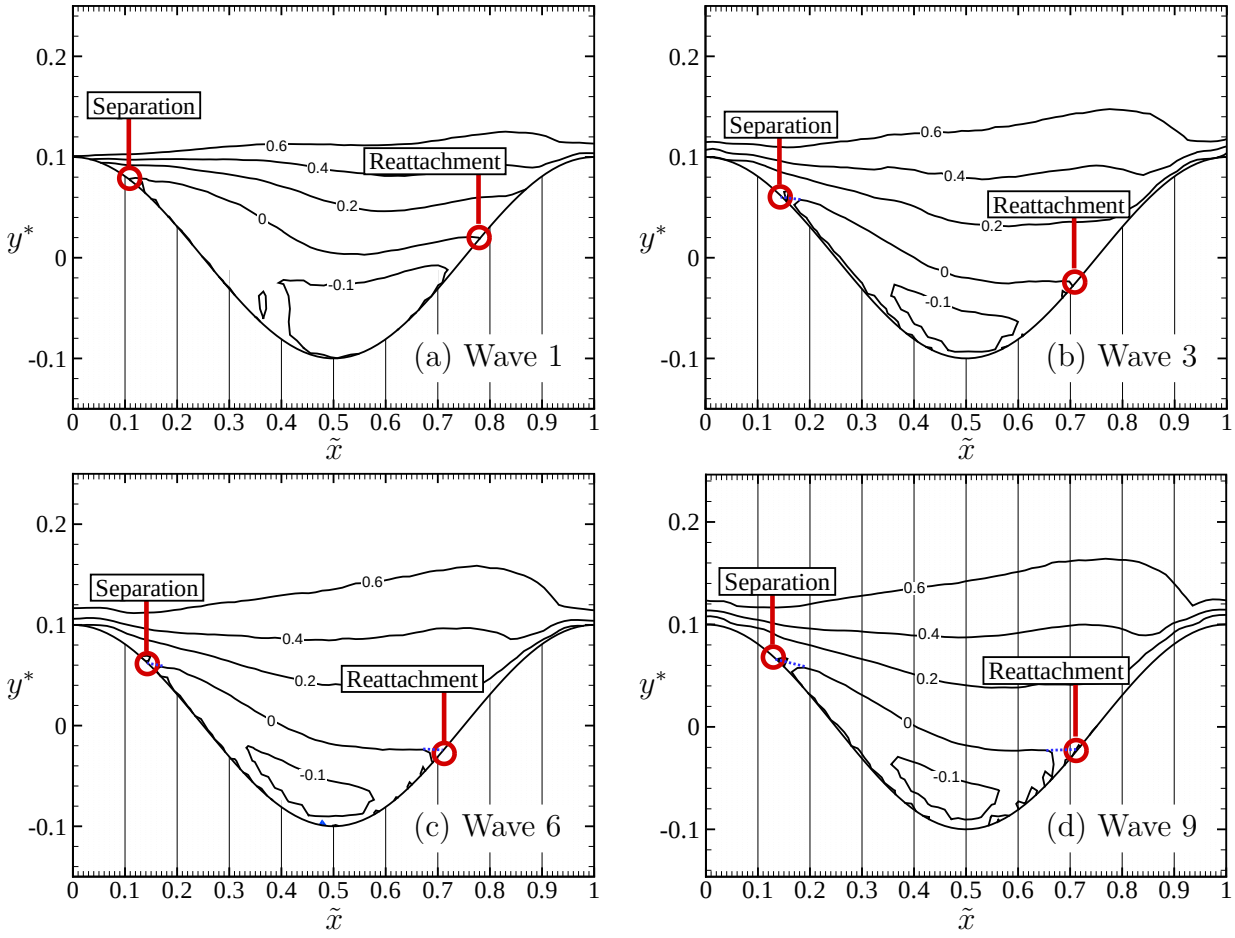

Figure D.3: Contour plots of dimensionless mean streamwise velocity, $\langle U \rangle^*$, at (a) Wave 1, (b) Wave 3, (c) Wave 6 and (d) Wave 9, at $\mathrm{Re_b} \approx 10700$.

D.2 Mean Velocity Gradients

The streamwise and wall-normal mean velocity gradients in both the x and y directions at Wave 9 are shown in Figure D.4. The velocity gradients have significant importance in the flow dynamics, as they contribute to the production of turbulent kinetic energy and in the Reynolds stresses transport equations. Figure D.4 shows that all velocity gradients presented have considerable magnitudes, which is in contrast to canonical turbulent shear flows. The velocity gradient $\partial\langle U \rangle/\partial y$ is dominant in most of Wave 9 whereas other velocity gradients,

$\partial\langle U\rangle/\partial x$, $\partial\langle V\rangle/\partial y$, and $\partial\langle V\rangle/\partial x$ are not negligible in certain regions of the flow. Because of these variations the flow structure and dynamics analyses are more complex than canonical turbulent shear flows.

Hudson *et al.* [26] demonstrated that velocity gradient-related terms in production can be significant in the flow dynamics mainly near to the wavy surface where large gradients of $\langle U\rangle$ and $\langle V\rangle$ exist. Buckles *et al.* [25] identified a region of high vorticity associated with free shear layer containing high velocity gradients. That region, as seen in Figure D.4 (b), encompasses $\partial\langle U\rangle/\partial y$ values in the order of 10 from $\tilde{x} = 0.9$ to 1.0 and between $\tilde{x}$ 0 to 0.15, at about $y^* = 0.12$.

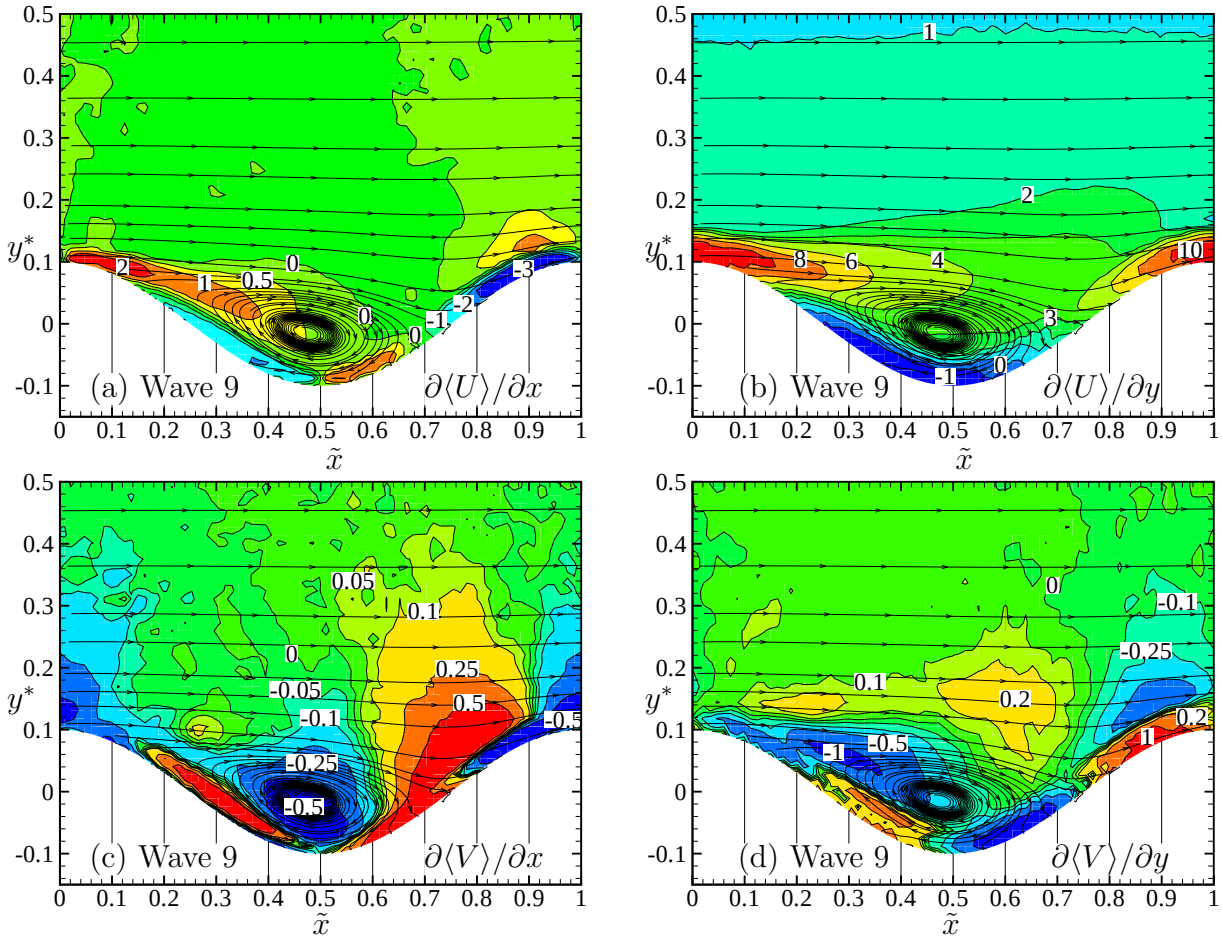

Figure D.4: Contour plots of streamwise and wall normal mean velocity gradients at Wave 9 in the x-direction: (a) $\partial\langle U\rangle/\partial x^\star$ and (c) $\partial\langle V\rangle/\partial x^\star$, and in the y-direction (b) $\partial\langle U\rangle/\partial y^\star$ and (d) $\partial\langle V\rangle/\partial y^\star$.